UNIVERSITY OF CALIFORNIA,
IRVINE

Experimental Investigations of Airplane Stability and Control Characteristics in Stall

DISSERTATION

submitted in partial satisfaction of the requirements
for the degree of

DOCTOR OF PHILOSOPHY

in Mechanical and Aerospace Engineering

by

Moatasem Fouda

Dissertation Committee:
Professor Haithem Taha, Chair
Professor John Michael McCarthy
Professor Mark E. Walter
Professor Matthew Mchenry
Professor Robert H. Liebeck

2022

DEDICATION

Dedicated with love and gratitude to Raghda

TABLE OF CONTENTS

LIST OF FIGURES

LIST OF TABLES

ACKNOWLEDGMENTS

I'm extremely grateful to Prof. Haithem Taha for giving me the opportunity to join his research group and pursue a Ph.D. at the University of California, Irvine. Also, I would like to thank him for his support during this journey and the invaluable insight into my experimental results.

I would like to express my deepest appreciation to Prof. Mark Walter and Prof. David Copp for granting me the assignment of the teaching assistant to their course "MAE-189: Senior Projects". It did not only support my Ph.D. financially, but also; it also made it possible for me to teach and mentor undergraduate students while pursuing my Ph.D. Every capstone project I have sponsored enriched my engineering knowledge and enhanced my communication skills. Working closely with Prof. Walter and Prof. Copp allowed me to learn from their kindness, professionalism, and dedication. It was one of the best experiences in my Ph.D.

I am also grateful to Prof. John Michael McCarthy for the robotics and linkage classes I took in my 1st year. It helped me design many mechanical systems for most of my experiments and paved my new career pathway toward surgical robotics. Prof. McCarthy indeed opened the gateway to the linkage and kinematic synthesis world not only for me but also for many UCI graduates.

Many thanks to the members of my dissertation committee, Prof. McCarthy, Prof. Walter, Prof. McHenry, and Prof. Liebeck, for serving on my Ph.D. committee.

I'd like to recognize the partnership and friendship of my lab mates Nabil Khalifa, Dipan Deb, Mahmoud Abdelgalil, Cody Gonzales, Mohamed Zakaria, Laura Pla Olea, Colin Sledge, Asmaa Eldesoukey, Fernando Pablo Quevedo, Jordi Ventura, and Amir Saman Rezaei.

I would like to extend my deepest gratitude to my wife, Raghda. It would not have been possible without her love and support. I'm extremely grateful to my girls, Fadwa and Nadine, for having them in my life, learning from them, and growing up with them. I deeply appreciate the love, support, and prayers of my father, brothers; Taha, Mohammed, and Mohab, and sisters; Shaimaa and Hasnaa. I'm fortunate to have a wise brother friend like Mohamed Shorbagy in many phases of my life, including this one. And to our cat daughter, Cauchy, I will never forget your company while working at night.

I would like to thank my friends on the other side of the earth: Mahmoud Zonfol, Mohammed Deif, Hossam Elhamy, and Ahmad Abusetta, and friends from my former work at Enppi; Shady Fathi, Moataz Kehela, Ashraf Montaser, Ahmad Abbas and Mohamed Sherbeny for their beautiful supporting messages and calls. Many thanks to Islam Rabie from the civil engineering department for providing me with many resources that helped me in building those experimental setups and for a cheerful company and sincere friendship. Special thanks to Gregory "Pk" Padilla for the morning walks and beautiful insights.

VITA

Moatasem Fouda

EDUCATION

Doctor of Philosophy in Mechanical and Aerospace Engineering **2022**
University of California, Irvine *Irvine, California*

Master of Science in Aerospace Engineering **2013**
Cairo University *Cairo, Egypt*

Bachelor of Science in Aerospace Engineering **2005**
Cairo University *Cairo, Egypt*

RESEARCH EXPERIENCE

Graduate Student Researcher **2018–2022**
University of California, Irvine *Irvine, California*

Graduate Student Researcher - Part Time **2009-2013**
Cairo University *Cairo, Egypt*

TEACHING EXPERIENCE

Teaching Assistant **2019–2022**
University of California, Irvine *Irvine, California*

WORK EXPERIENCE

Project Manager **2013–2018**
Engineering for the Petroleum and Process Industries (Enppi) *Cairo, Egypt*

Project Engineer **2010–2013**
Engineering for the Petroleum and Process Industries (Enppi) *Cairo, Egypt*

Piping Stress Analysis Engineer **2008–2010**
Engineering for the Petroleum and Process Industries (Enppi) *Cairo, Egypt*

ABSTRACT OF THE DISSERTATION

Experimental Investigations of Airplane Stability and Control Characteristics in Stall

By

Moatasem Fouda

Doctor of Philosophy in Mechanical and Aerospace Engineering

University of California, Irvine, 2022

Professor Haithem Taha, Chair

Half of the unintentional stall accidents in light general aviation airplanes likely cause fatalities. At stall, airplanes typically experience a vast rolling moment due to asymmetric lift distribution caused by uneven stall between the two wing laves. This dangerous rolling moment (known as wing drop) and a yaw moment caused by the same uneven stall cause lateral-directional instability at stall. The developed spin becomes more difficult to avoid as the roll control authority and handling qualities are significantly degraded at stall. In the first part of this dissertation, we focus on studying the airplane stability and control authority characteristics near stall. We designed a wind tunnel experiment to investigate both the wing drop and roll control authority in the pre-stall, stall, and post-stall regimes of a wide range of angles of attack (from -9 to +62 degrees). We designed and built five airplane models of different wing planform configurations: rectangular, tapered, hybrid (rectangular-tapered), cropped delta, and cropped elliptic to study the effect of the planform on the wing drop direction and magnitude. Simple flow visualization using tufts was used to study the effect of the wing planform on the stall progression. We developed a novel multi-axis load cell capable of withstanding the violent dynamic loads associated with stall. We measured lift, drag, rolling, and pitching moments vs. aileron and elevator deflections to assess the effectiveness of the control surfaces in the whole range of the angle of attack.

In the second part of this dissertation, we focus on the dynamic stall of two-dimensional wings. A wind tunnel experiment is designed for a continuously pitching wing over full rotation. Lift enhancement and stall delay are observed due to pitching rotation. The effect of angular velocity, Reynolds number, and airfoil type on this lift enhancement is investigated.

Nomenclature

α	Angle of attack
α_{Stall}	The critical stall angle
δ	Boundary correction factor
δ_a	Aileron deflection
δ_e	Elevator deflection
ϵ_{tot}	Total solid and wake blockage correction factor
λ	Taper ratio
ω	Wing model pitching velocity or stepper motor rotational speed
$\sigma_{\overline{n}}$	Standard error
AOA	Angle of attack
AR	Aspect ratio
b	Wingspan
c	Chord
$C_{\mathcal{L}_{\delta_{\dashv}}}$	Aileron effectiveness parameter

$C_{\mathcal{L}}$ Rolling moment coefficient

$C_{\mathcal{M}_{\delta_\gamma}}$ Elevator effectiveness parameter

$C_{\mathcal{M}}$ Pitching moment coefficient

$C_{\mathcal{N}}$ Yaw moment coefficient

C_D Drag force coefficient

C_{L_α} Lift-curve slope

$C_{L_{max}}$ Maximum Lift Coefficient

C_L Lift force coefficient

I_{xx} Airplane longitudinal moment of inertia

I_{yy} Airplane lateral moment of inertia

k Rotating wing reduced frequency $k = \frac{\omega \times b}{V_\infty}$

Re Reynolds number

S Wing surface area

V_∞ Air speed

Chapter 1

Introduction and Discussion

This chapter not only surveys the literature but also compares the results of this research and the relevant literature in the area of wing drop and spin.

1.1 Background and Motivation

Pilots are usually trained in the primary training phase to recognize stall at an early stage, avoid it, and recover from it if not avoidable [1, 2, 3]. Unfortunately, 50% of the unintentional stall accidents in light airplanes likely cause fatalities, while only 17% of those non-stall accidents cause fatalities (Fig.1.1). The numbers are much better in commercial flights, where the fatalities due to stall drop to 30%, and the non-stall fatalities drop to 13% (Fig.1.2)[2]. Commercial airplanes are equipped with angle of attack sensors, stall sensors, and an automatic incipient spin recovery system, which is more responsive than human pilots. These systems could apply corrective controls before the aircraft enter a developed spin. If the parameters of this automatic control system are well-tuned, it will even be able to prevent incipient spin [4]. With all these AOA and stall sensors, it is a well-established

principle in the civil aviation field to avoid the stall. The significant drop in the number of stall accidents from 2005 until 2010 seems to be attributed to many efforts by the regulating authorities, by adding more preventive systems and limiting the flight envelope. Limiting the flight envelope will have some impacts, such as higher fuel consumption and increased ground noise level due to the reduced climb rate.

After World War II, a large surplus of military aircraft found its way to the personally owned aircraft market. This change in the application of these high wing-loading aircraft in addition to the inexperience of its new pilots led to an alarming number of stall/spin accidents. In the post-war period, 48% of the fatal accidents were because of stall, and spin [4].

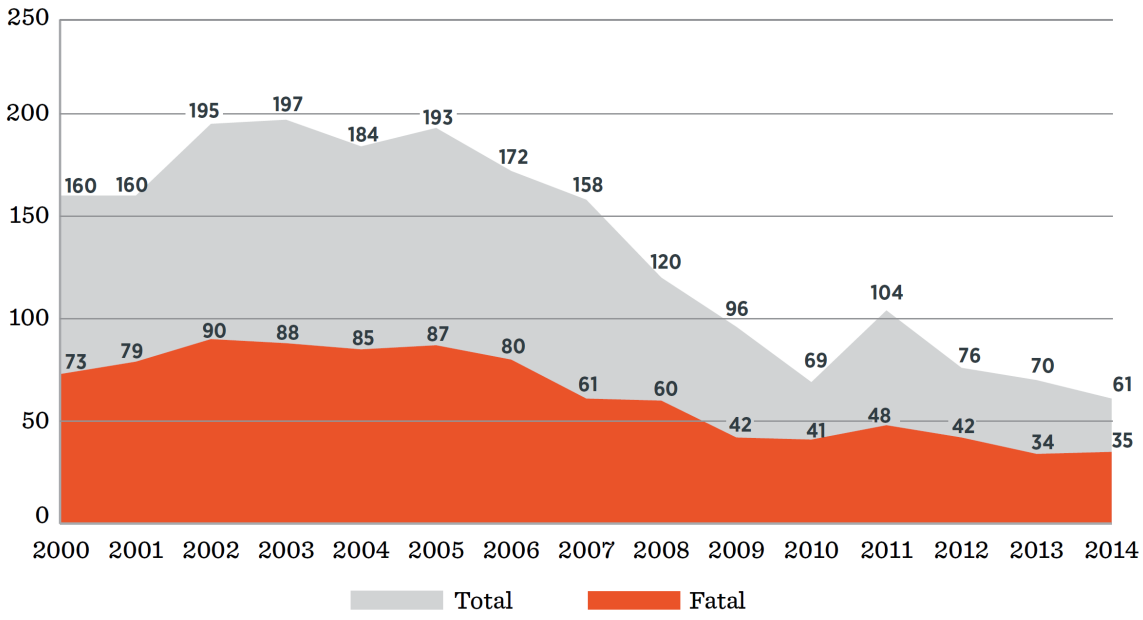

Figure 1.1: Annual number of stall accidents from 2000 to 2004 [2].

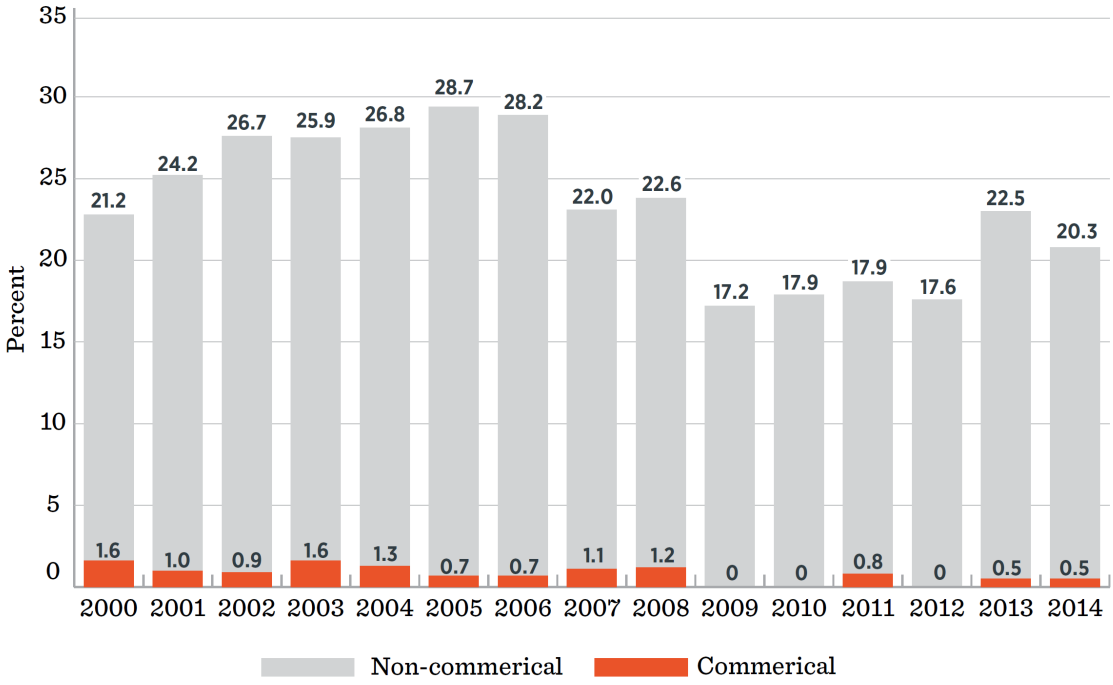

Figure 1.2: Stall accidents percentage in the total fatal accidents based on the fixed wing airplane size [2].

In the military aviation field, flying a fighter airplane at high angles of attack, near the stall or even post-stall, is a common maneuver, especially if this airplane is equipped with thrust vectoring. However, there is always a need to enhance the military airplane's stability and maintain some control authority in the stall.

Stall typically happens during the high angles of attack and low-speed phases such as takeoff, climb, and landing phases. The low speed decreases the critical stall angle, while the necessary flaps' deflection in these phases increases the relative angle of attack. Both parameters, the lower critical stall angle and higher relative AOA make a good recipe for stall in these low-altitude phases. The trained pilots do not have sufficient altitude to dive and recover the laminar flow over the wing.

In our view, the widely spread definition of stall as a drop in the lift force and a rise in the drag force is not enough to justify this high fatality rate. According to many wind-

tunnel testings, including this one, and many successful recoveries from stall and spin, there is a dramatic loss in the rolling stability and significant deterioration in the aileron control authority associated with stall. This rolling instability leads to the spin, and the only way to recover from spin is to dive the airplane. In all categories of aircraft, stall and spin remain common causes of fatalities due to departures from controlled and coordinated flight. Still, unrecognized stalls and poor recovery techniques have contributed to accidents even in the transport category.

For these fatal reasons and military needs, the stall phenomenon has always been under investigation since the tragic death of Otto Lilienthal, father of flight, in 1896 as a result of a stall accident. Stall does not only affect fixed-wing airplanes, but also the efficiency and reliability of the rotating wings, such as helicopter's and wind turbine's blades. This endless engineering and research work has led to classifying the stall phenomenon into different categories based on the application. For the fixed wings application, the stall has been classified into the leading-edge stall, trailing edge stall, and thin airfoil stall [5] and into light and deep stall [6] according to the tail configuration. It is also classified into a static stall and dynamic stall based on the wing pitching rate and the associated unsteadiness[7, 8].

1.2 Lift Development

Holger Babinsky [9] carried out an interesting flow visualization experiment by injecting pulses of smoke over an airfoil at a positive angle of attack. Injecting the smoke intermittently enables a better assessment of the flow field, as the velocity magnitude could be estimated in addition to the velocity vector direction by measuring the distance cut by the smoke particle from a video frame to the next frame and then multiplying it by the frame rate. In this experiment, smoke is injected at 21 equispaced positions; 10 streamlines span the upper half of the test section, and another 10 streamlines span the lower half except in the vicinity of

the test section walls, while the middle one looks to be aligned with the test section center line. The airfoil seems to be pitched up at about 19% of its chord, i.e., the center line of wind tunnel test sections intersects with the chord line at about 19% of the chord length from the leading edge at this angle of attack. At this angle of attack, the flow field is split by the wing, where 13 streamlines move above the airfoil and 7 streamlines move below the airfoil. The flow field is not split equally, maybe because the lower half of the test section is blocked by about 81% of the airfoil times the ArcTan of the angle of attack, while the upper half is less blocked by only the remaining 19% of the airfoil times the ArcTan of the angle of attack (Fig.1.3).

The main finding of this experiment is that fluid particles moving above the airfoil are faster than those moving below the airfoil, in accordance with the basics of airfoil theory. In fact, the upper fluid particles reach the trailing edge of the airfoil before the lower particles, which refutes the widely spread and groundless misconception that the two adjacent fluid particles separating near the leading edge have to meet again at the trailing edge. Frame 1, in figure 1.4, shows the smoke lines reach the inlet of the test section at the same moment. Frames 2 and 3, in the same figure, show that fluid particles moving above the airfoil accelerate with respect to their counter particles below the airfoil. The advancement gap between the upper and lower particles looks to be maintained in the following frames (frames from 4 to 6), which implies that the upper particles stop accelerating and do not decelerate with respect to the lower particles while moving over the remaining portion of the airfoil.

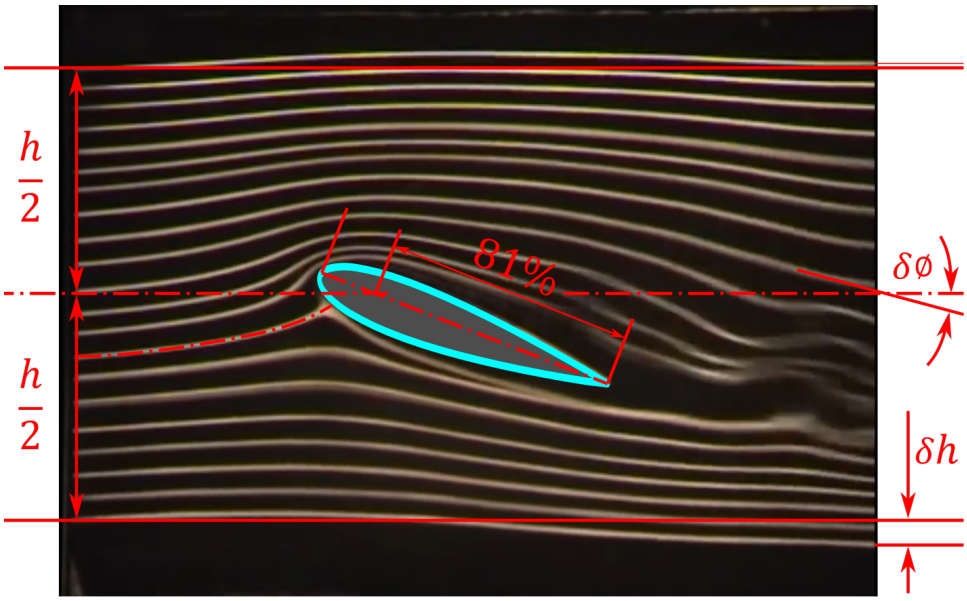

Figure 1.3: Flow visualization over an airfoil at positive angle of attack adapted from Babinsky (2003)[9].

It is controversial whether the decreasing static pressure over the upper surface results from the increasing velocity or the opposite. The important conclusion here is that the decreasing pressure on the upper surface is the major contributor to the lift force. On the other side of the airfoil, the lower surface blocks the flow and converts some of the dynamic pressure of the flow to a static pressure acting on the lower surface. In fact, this blockage-induced lift on the lower surface was considered the main lift source according to the Newtonian theory of fluid mechanics. This hypothesis led to calculating a much smaller lift than what is typically observed in reality, which was deemed by some scholars as a reason for delaying the birth of aviation; If nature followed the Newtonian theory, flight would be impossible [10].

Babinsky attributed this pressure/velocity difference to the pressure gradient across the streamlines due to curvature. In order for the fluid particle to move along a curved path over the airfoil, there must be a centripetal force that pulls the fluid particle towards the airfoil; otherwise, it will move in a straight line according to Newton's first law. The reaction of this

centripetal force from the airfoil on the fluid particles represents a lift source on the airfoil [11, 12, 13]. Below the lower surface of the airfoil, the situation is reversed, leading to an upward lift force too.

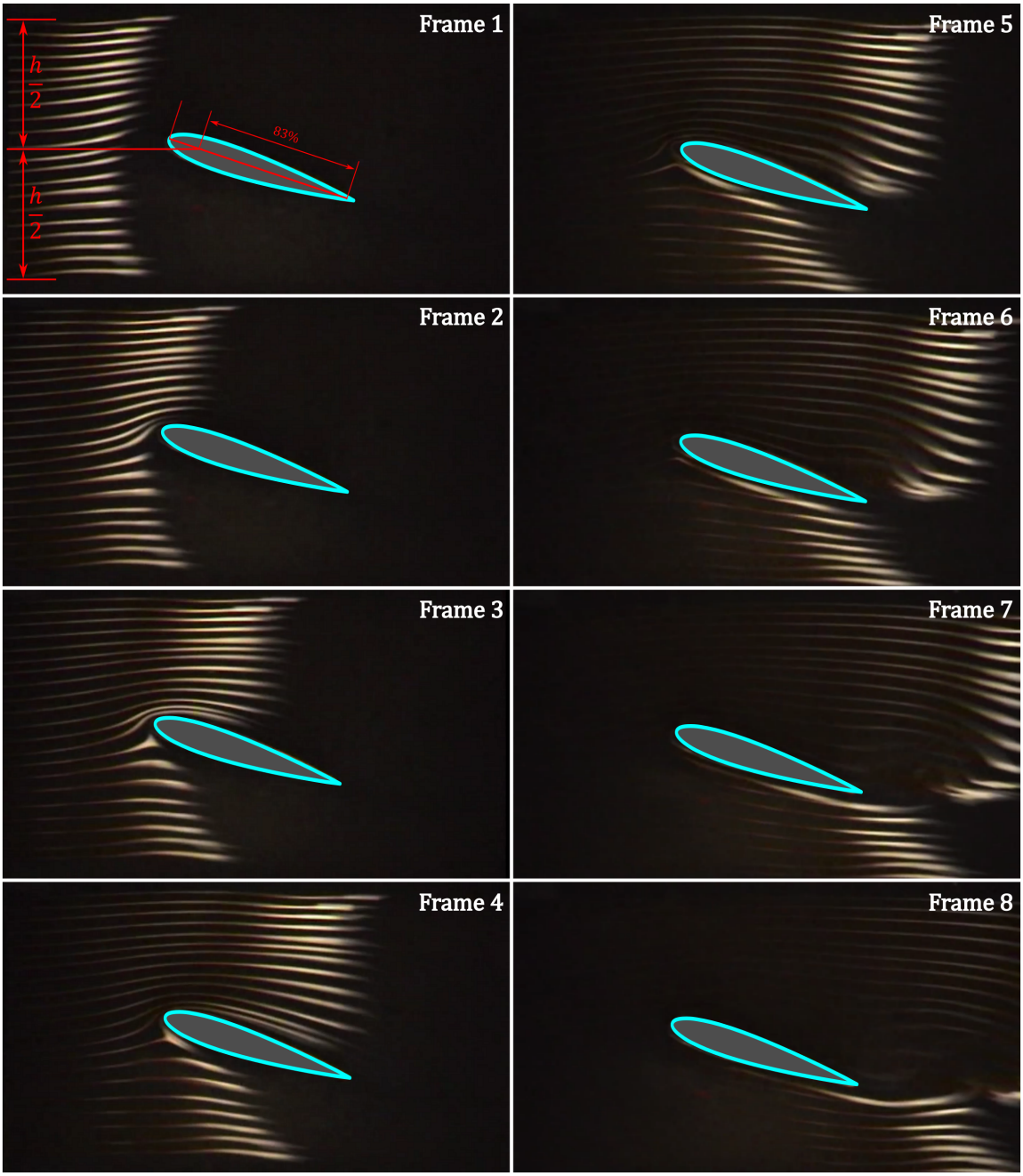

Figure 1.4: Intermittent smoke flow visualization over an airfoil at positive angle of attack, adapted from Babinsky (2003) [9]

The questions are now: why do the upper fluid particles accelerate above the airfoil in

the first portion of the wing, and why do not the lower fluid particles accelerate in the second portion of the wing sufficiently to catch up with their upper counterparts at the trailing edge according to the widely spread misconception? To answer these two questions, let's propose the analogy to the convergent-divergent nozzle shown in Figure 1.5. However, this analogy should not be taken as a strict explanation for lift generation but an analogy that may be useful in answering these two questions. Figure 1.5 shows that fluid particles moving over the upper surface of the airfoil are analogous to fluid particles moving in the axial mid-plane of a subsonic convergent-divergent nozzle (de Laval nozzle), while those below the airfoil are analogous to fluid particles moving in the axial mid-plane of a subsonic divergent-convergent nozzle. The top straight/uncurved streamline, near the ceiling of the wind tunnel test section or at the infinity of an unconstrained experiment, could be considered as a symmetry plane to hypothesize a mirrored half of this convergent-divergent nozzle. The bottom straight streamline will be considered as the symmetry plane for the hypothesized divergent-convergent nozzle of the fluid particles moving below the airfoil. The upper fluid particles in the convergent part of the nozzle are compressed while approaching the airfoil because of the reduced area. It is an acceleration region to the minimum pressure peak [14]. The highest point of the airfoil creates a virtual throttle, at which the maximum velocity and the minimum pressure occur. At high angles of attack, the highest point of the airfoil will act as an orifice. This orifice analogy shifts the maximum velocity and the lowest pressure location slightly downstream of the highest point, which is known as the Vena contracta [15]. On the lower side of the airfoil, in the divergent part, the fluid expands subsonically, reducing the velocity and increasing the pressure slightly, as the nozzle divergence is not as much as the convergence on the upper side. The low gradient of the boundaries of the second halves of both nozzles is not enough to decelerate the fluid particles moving above the airfoil and accelerate those moving below, such that they meet again at the trailing edge. It is interesting to note that after we established this analogy, it appeared to us that Einstein had made a similar analogy, though with pipe flow [16].

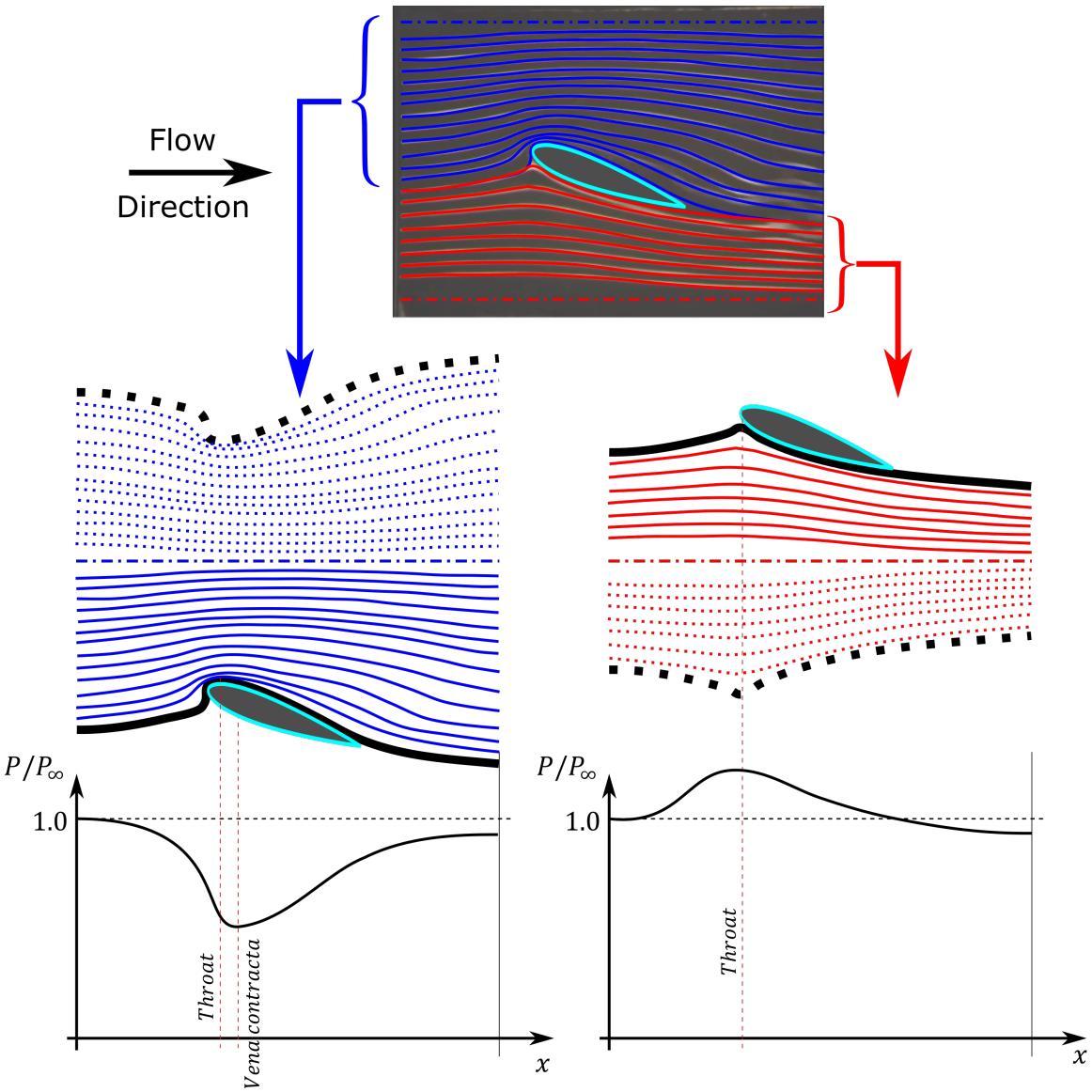

Figure 1.5: Flow field around an airfoil from convergent-divergent nozzle perspective

This pressure distribution creates a significant suction on the upper surface with a minimum pressure at (or slightly downstream) the highest point on the airfoil's upper surface. It also creates a high-pressure region under the airfoil. Both pressures on the upper surface and the lower surfaces contribute to the production of the lift. Pressure distribution is commonly represented by plotting the pressure coefficient versus the normalized distance from the leading edge (Fig. 1.6). The pressure coefficient is the ratio of the difference between the local pressure and the static pressure to the dynamic pressure as follows:

$$C_p = \frac{P_{Local} - P_\infty}{\frac{1}{2}\rho V_\infty^2} \tag{1.1}$$

The benefit of using the pressure coefficient is to indicate whether the local pressure is greater or less than the static pressure, while the lift generated by the airfoil is a function of the enclosed area of the C_p plot [5]. Figure 1.6 shows the contribution of the upper surface in the lift production is higher than the contribution of the lower surface.

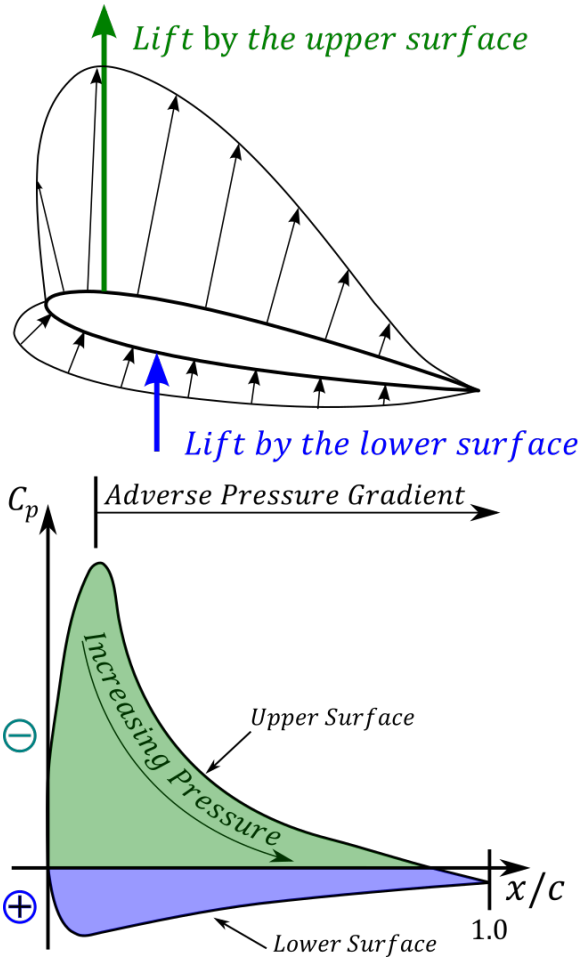

Figure 1.6: Pressure coefficient distribution over an airfoil

1.3 Stall Development

Fluid viscosity generates part of the drag on the wing. This part is called skin friction drag. Prandtle hypothesized that for a fluid with a small viscosity (such as air), the effects of viscous actions are confined to a thin transitional shear layer adjacent to the surface[17]. In this layer, there exists a velocity gradient, where the velocity increases from this solid velocity to the velocity of the stream at the edge of the layer (Fig. 1.7). The thickness of this layer, which is known as the boundary layer, is usually considered the normal distance from the surface to the first streamline having 99% of the local inviscid velocity, just outside the transitional layer [18].

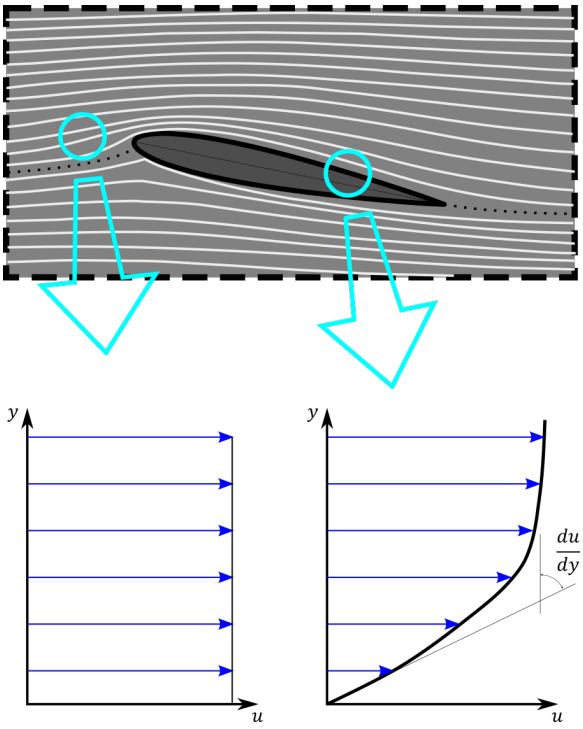

Figure 1.7: Boundary layer adjacent to the skin of a streamlined body in a moving fluid

As the angle of attack increases, the adverse pressure gradient on the upper surface increases. At a certain angle of attack, the low inertia fluid particles near the surface within the boundary are not capable of overcoming this large adverse pressure to maintain the

motion. The low inertia fluid particles near the surface flip their motion direction under this adverse pressure gradient, while their adjacent higher inertia fluid particles maintain their motion causing flow separation from the surface (Fig. 1.8). In other words, stall occurs on a two-dimensional airfoil section when the angle of attack exceeds a certain critical value (that mainly depends on the airfoil geometry and Reynolds number) [19, 20]. When the flow separates from the upper surface, the wing becomes stalled. Wing stall decreases the lift force and increases the drag force, (i.e. the two components of the aerodynamic forces), significantly.

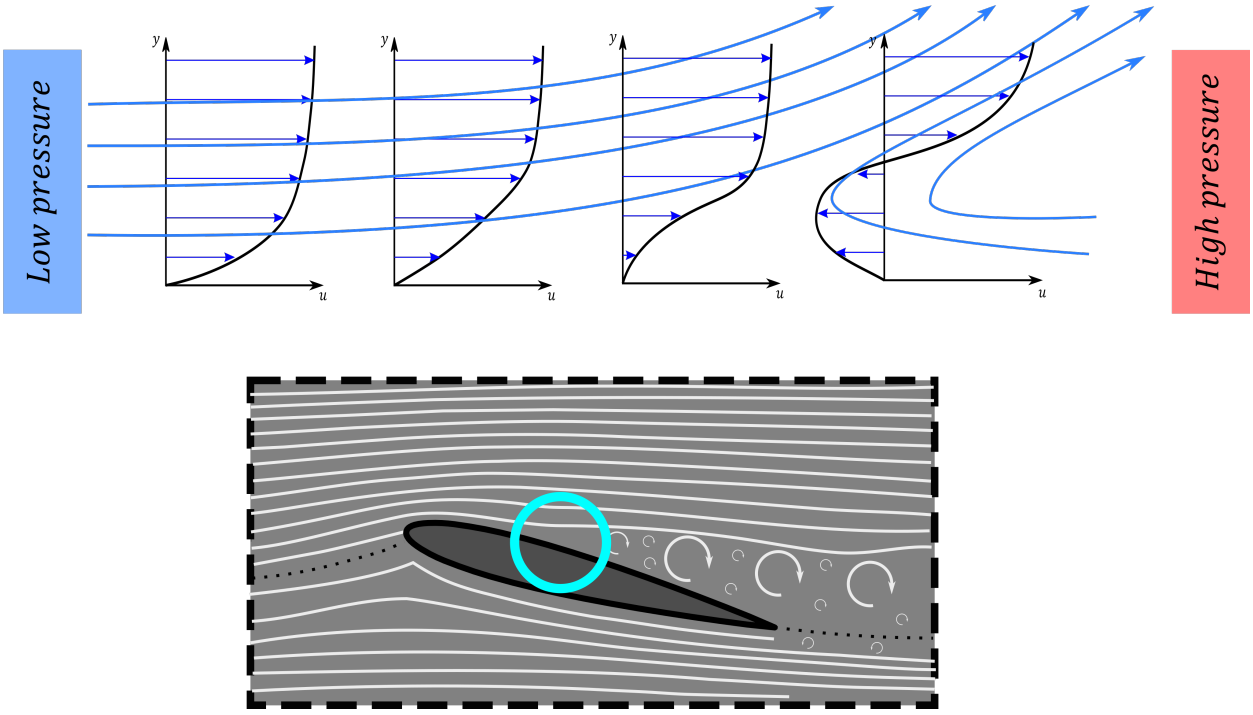

Figure 1.8: Flow in the boundary layer in an adverse pressure gradient at the point of separation, adapted from Schlichting (1979) and Hoerner (1965) [18, 21]

There are three types of stall on subsonic wing sections based on the thickness of the airfoil [22, 5]:

1. Trailing edge stall of thick airfoils of thickness to chord ratios of about 15% and above (Fig. 1.9 -a): Boundary layer point of separation occurs almost at the trailing edge due

to the upward and sudden flow from the region below the airfoil to the region above the airfoil. The separation then propagates over the upper surface towards the leading edge as the angle of attack increases. This stall is a favorable stall type as it produces a rounded lift curve at the stall angle. This gradual lift loss gives the pilots the time to recover the airplane from stall.

2. Stall of moderately thick airfoils of thickness to chord ratios of about 9% (Fig. 1.9 -b); Boundary layer point of separation occurs immediately downstream of the pressure suction peak (Fig. 1.6). The flow re-attaches again, creating a short separation bubble compared to the airfoil chord length. The effect of this separation bubble on the pressure distribution is local. Increasing the angle of attack moves the separation bubble towards the curved leading edge of the airfoil, which makes it difficult for the flow to reattach again, and the separation bubble is said to burst. The lift force suddenly decreases, making it difficult for the pilots to avoid stall and the emerging spin.

3. Leading edge stall of thin airfoils of thickness to chord ratios less than 6% (Fig. 1.9 -c): A separation bubble occurs at very small angles of attack. It is like a sacrifice by some fluid particles to create a less-curved way for the flow to minimize the required curvature for the main stream fluid particles to remain attached to the upper surface without separation. At a certain critical angle of attack, the short separation bubble at the leading edge expands dramatically, covering a big portion of the upper surface of the airfoil or almost the whole upper surface of the wing, creating a long separation bubble. This separation bubble expansion slightly decreases the lift curve slope and makes a short plateau in the lift force during this expansion. It is like an additional sacrifice to change the airfoil section for the other fluid particles from a thin airfoil to a thick and cambered airfoil. The lift curve peak is slightly rounded in this type of stall.

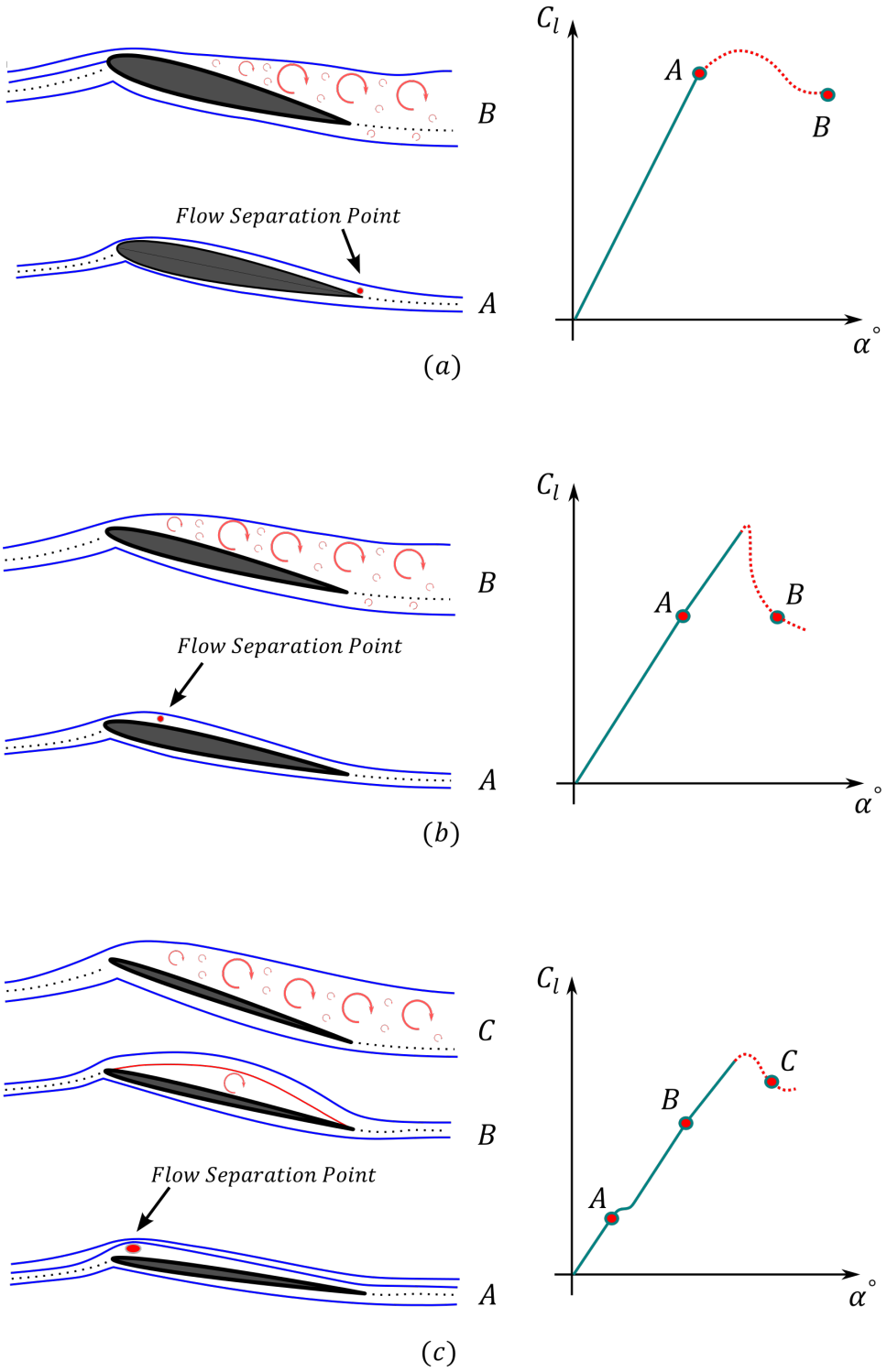

Figure 1.9: Low-speed airfoil stall types, adapted with changes from Torenbeek (1982) and Whitford (1987) [22, 5]

In the previous paragraphs, stall is explained with respect to the two-dimensional wing

cross-section, and the airfoil, but in three-dimensional wings, the stall phenomenon is more complicated. In the three-dimensional wing, each airfoil section operates at a different angle of attack, due to the spanwise variation of lift and downwash according to Prandtl's lifting line theory [23, 10]. The wing root sections of the straight rectangular wings experience separated flow at values of lift coefficient slightly below the maximum lift coefficient of the wing. The stalling wing root sections give the pilots adequate stall warning before stalling the ailerons [24]. The tapered and swept-back wings shift the section of the maximum local angle of attack towards the tips, while the decreasing chord length of the outboard wing sections reduces the Reynolds number and accordingly the critical stall angle of attack. Both parameters make the outboard ailerons of the tapered and swept-back wings vulnerable to stall [25]. This scenario is usually resolved in a proper wing design by washout (down twist of the outboard wing sections) [26]. Another way that is not recommended because it reduces the overall maximum lift coefficient of the wing, is to move the stall starting point towards the wing root by selecting wing sections for the inboard wing section with less maximum lift coefficient (aerodynamic twist)[24]. Yet, with all these clever design guidelines, proper adjustment of airplane stall characteristics remains to be quite a challenging task [26].

1.4 Wing Drop Development

The high rate of fatalities associated with stall could not be attributed only to the rapid lift force drop (about 25%) and/or to high deceleration due to the sharp rise in the drag force (about 100%) at stall (Fig. 1.10). Let us assume a hypothetical situation to prove that the drop in the lift force at stall is not that fatal, as typically taught in some undergraduate classes. Assume an airplane subjected to a hypothetical balanced stall, i.e., the two wings are stalled at the same moment, and the airplane will start decelerating due to the instantaneous 100% rise in the drag force. In addition to the 25% rapid drop in the lift force at stall the lift

force will experience another, but slow, decrease because of the decreasing speed. Therefore, the airplane should gain a downward velocity component, i.e., the airplane will lose altitude. This component of the downward velocity increases the effective angle of attack α_e beyond the limit of the critical stall angle α_{stall} which takes the airplane to the post-stall regime. This transition to the post-stall regime hypothetically happens without even considering the decrease in the critical stall angle α_{stall} due to the decreased Reynolds number. The two components (Lift and drag) of the aerodynamic force increase in the post-stall regime. If this aerodynamic force is analyzed in the inertial frame the vertical components will be even higher than the highest lift value before stall (Fig. 1.11-b). In other words, the wings should act as parachutes and decelerate the falling motion giving the time to the pilot to act properly, but this hypothetical situation is unlikely to happen, as shown in this section and the following section. Pilot trainees are encouraged not to try it without sufficient altitude and without sufficient training on spin recovery.

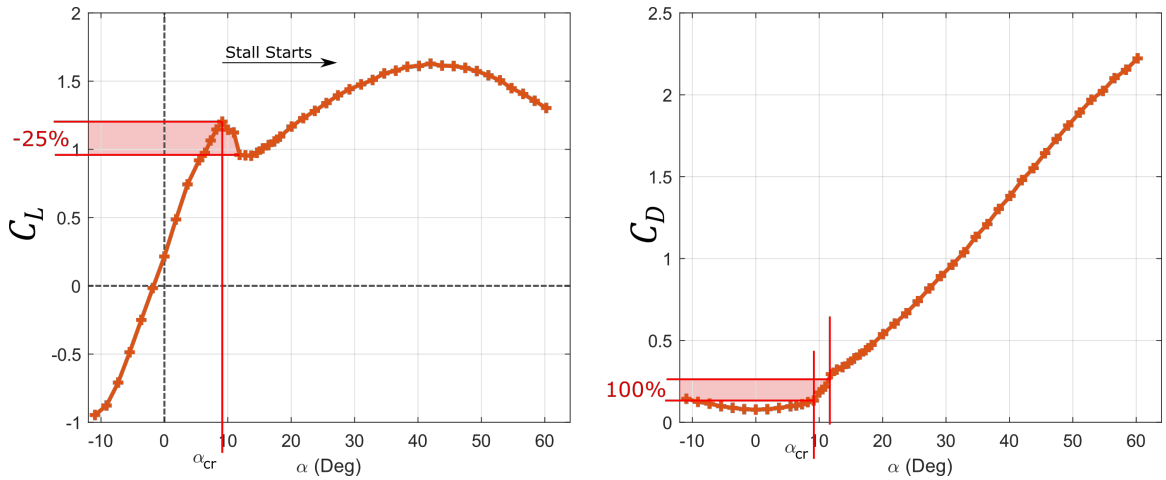

Figure 1.10: Lift force 25% rapid drop and Drag 100% instantaneous increase at stall - Wind tunnel testing on airplane model under this experimental research

We found in this study that stall starts at a certain wing section for every wing planform and then propagates quickly over the wing [27]. This experimental result, which will be discussed in detail later, is in line with the stall patterns in the Aerodynamics for Naval Aviators book and the USAF Test Pilots' Flying Qualities Textbook [28, 29]. Stall, as

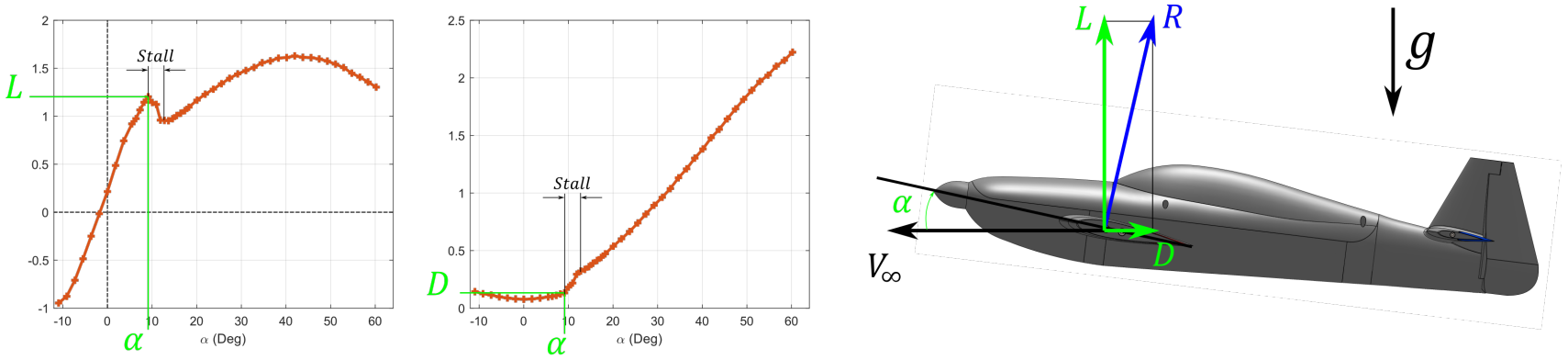

a) Airplane in a leveled flight at the critical stall angle, just before developing a stall

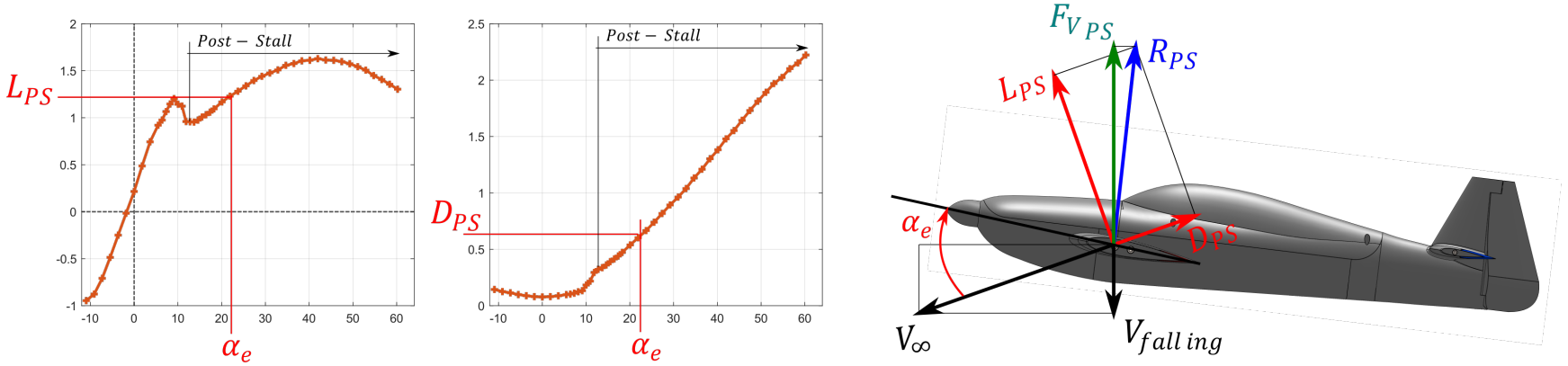

b) Airplane at AOA higher than the critical stall angle due to a downward velocity component at a hypothetical balanced stall

Figure 1.11: Hypothetical situation of a balanced stall never happens; in the post-stall regime, the wings will parachute the airplane.

explained before, is an abrupt change in the flow pattern over the upper surface of the wing. This nonlinear rapid change is extremely sensitive to any little change in any relevant parameter, mainly the angle of attack α and secondarily the Reynolds number and wing cross-section. The geometric angle of attack of the wing α_g is affected not only by the conventional pitching (nose up or nose down by the elevator) but also by deflecting the ailerons or the flaps. Unlike the flaps, ailerons' deflection affects the geometric angle of attack α_g in a differential way, where the downward aileron deflection increases the camber and accordingly it increases the geometric angle of attack (Fig. 1.12-b), while the upward aileron deflection decreases it 1.12-c).

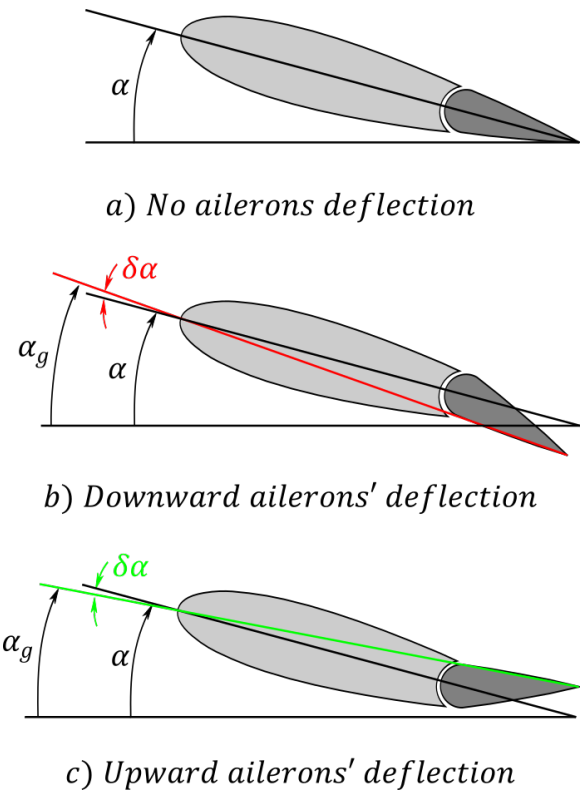

Figure 1.12: Effective of aileron deflection on the geometric angle of attack

Maneuvers like rolling and yawing affect the effective angle of attack α_e in a differential way similar to the effect of the aileron deflection on the geometric angle of attack α_g. The effect of the roll rate on the local angle of attack is a damping effect, as it increases the

effective angle of attack of the down-going wing and decreases that of the up-going wing and accordingly increases the lift force on the down-going wing and vice versa, thereby resisting the rolling motion [30]. Other asymmetric maneuvers such as yaw rate and side slip change the effective angle of attack and speed in a differential way similar to the roll rate changes.

The slight difference in the angle of attack between the right and the left wings accelerates the stall on one wing before the other. This uneven stall will generate a huge rolling motion that reduces the effective angle of attack of the unstalled wing and increase the angle of attack of the stalled wing. It makes the stalled wing more stalled and takes the unstalled wing away from the critical stall angle α_{stall}. It is an unstable situation, as this rolling instability, which is known as Wing Drop, aggravates with time [31, 32, 33, 34].

The very important and legitimate question that will change our understanding of the wing drop and the spin phenomena is: Will the two wings stall at the same moment if there are no asymmetries like the aileron or rudder deflection or side slip? The answer is NO! A wing drop typically happens. In real-life pure symmetry is an impossible situation, and even if life were symmetric, stall would still be asymmetric. The pendulum was always a magnificent simple mechanism that helped the human being to develop mathematics, mechanics, and even nonlinear dynamics. In this stall situation, we have a strong feeling that a stalling airplane is analogous to an inverted pendulum. An airplane in a leveled flight in the pre-stall regime is analogous to a damped pendulum at the lower stable equilibrium. The stiffness is generated by the dihedral angle, while the rolling motion is a damped motion, as discussed earlier. (Fig. 1.13-a). An airplane at the critical stall angle is analogous to an inverted pendulum. Mathematically, without any perturbations, the pendulum should stay at this equilibrium, but we know very well that in the real world, the pendulum will have an infinitesimal deviation to any side. This infinitesimal angular deviation will generate an increasing (aggravating) rolling moment taking the pendulum to the lower stable equilibrium position. This kind of equilibrium point is known as a stable node in the nonlinear dynamics

field. This node is described as stable because it has a single stable invariant direction (eigen vector) [35]. This stable direction represents the hypothetical situation of having no side perturbations. It is named a "stable node" to differentiate from the unstable node, which has no stable directions. We think calling the stable node with this name is misleading, as it is already unstable mathematically in the whole domain except for the eigen vector, and physically and simply, it is unstable. Back to our stalled airplane, The same unstable behavior happens to an airplane at the critical stall angle, with a realistic, and always there, infinitesimal deviation in the effective angle of attack between the right and the left wing will make one wing stall before the other one. The asymmetric stall, the wing drop, will create a huge rolling moment [6, 25, 36, 37] that will roll the airplane to the direction that reduces the effective angle of attack of the unstalled wing and increase the angle of attack of the stalled wing 1.13-b).

In conclusion, Wing Drop or the uneven stall or the asymmetric lift distribution happens at the critical stall angle. The wing drop happened in all wind tunnel tests performed under this research on five airplane models [38, 27]. Later, we will discuss the effect of the wing planform on the perdition of the wing drop direction and its magnitude.

Von Karman noticed that Prandtl's lifting theory results in non-unique solutions of the lift distribution at the angles of attack where the lift- α curve has a negative slope $m(y) < 0$, like what happens at the critical stall angle [39, 40]. The circulation distribution governed by Prandtl's integral equation is proportional to the lift- α curve slope $m(y)$, as follows:

$$\Gamma(y) = \frac{1}{2} U c(y) m(y) \left\{ \alpha(y) - \frac{1}{4\pi} \int_{-b/2}^{b/2} \frac{\Gamma'(\eta)}{y - \eta} d\eta \right\} \tag{1.2}$$

$\Gamma(y)$: is the span-wise distribution of the circulation.

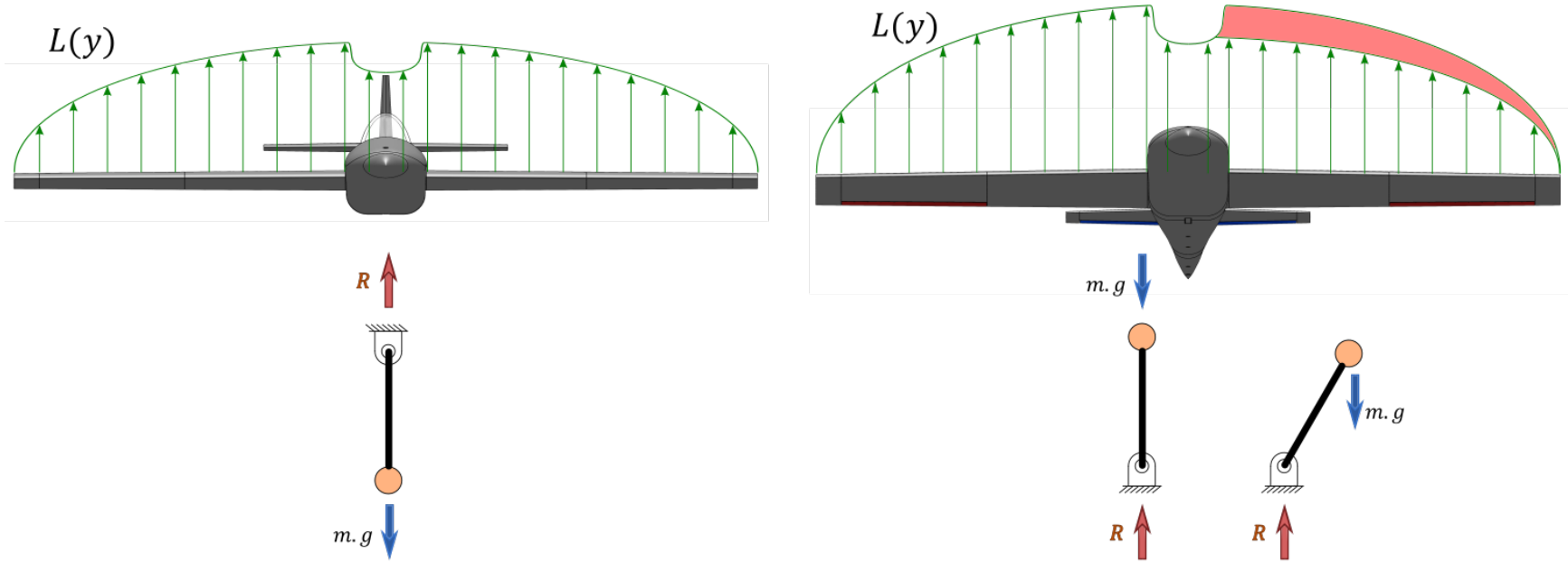

a) Leveled flight in the pre − stall regime b) Leveled flight at the critical stall angle

Figure 1.13: Stalled airplane analogy to an unstable inverted pendulum

U: is the free stream velocity.

$c(y)$: is the span-wise distribution of the chord.

$m(y)$: is the span-wise distribution of the slope of the lift- α curve. It will be variable in case of aerodynamic twist (i.e., different wing airfoil sections.)

$\alpha(y)$: is the span-wise distribution of the angle of attack. It will be variable in case of aerodynamic twist.

Von Karman predicted that lift distribution would have nonunique solutions where the lift-α curve has a zero slope or "portions of positive and negative slopes or having discontinuities. "If this were true, the appearance of asymmetric distributions and large rolling moment near the stall might be explained without postulating an initial rolling velocity," according to Von Karman's student William Sears[39, 40].

Schairer, who was another student of Von Karman worked on the same topic of the unsymmetrical lift distribution of a stalled wing and concluded the following points in his Ph.D. thesis [41]:

1. An unsymmetrical lift distribution across the span at stall is possible.
2. This unsymmetrical lift distribution generates a rolling moment of a magnitude as much as that generated by the fully deflected ailerons.
3. The unsymmetrical lift distribution occurs in a very small range of angles of attack beyond the critical stall angle of attack.

Sears followed this statement with another statement referring to the usual textbook explanation, which postulates an initial rolling velocity to have this asymmetric stalling wing. Sadly, most of the textbooks and pilot handbooks issued by governmental authorities such

as the Federal Aviation Authorities (FAA) still, after almost 85 years, postulate asymmetric angle of attack to generate spin, as discussed in the following section.

At the end of this section, it is noteworthy to point out some other instabilities at stall that may cause confusion with the wing drop phenomenon. One of these instabilities is known as wing rock. Due to the increasing speed of jet-engine airplanes after the world war, the leading-edge sweep angle was increased to reduce transonic and supersonic drag [42, 43]. This high sweep angle requires a high angle of attack during landing to maintain reasonable landing speed. This high angle of attack landing conditions initiates flow asymmetries which trigger limit cycle roll oscillations, known as wing rock. The limit cycle oscillations are sustained by nonlinear aerodynamic roll damping [44]. The wing rock degrades control surfaces' effectiveness and handling qualities during air combat maneuvering[6, 45].

Like the wing rock, another phenomenon occurs in the transonic region, referred to as the Heavy wing. It results from asymmetric shock-induced separation over the aileron portion of the wing. This flow separation usually reduces aileron effectiveness and the wing's overall lift. In addition, heavy wing causes uncommanded asymmetric roll like the wing drop [46].The time response of the bank angle ϕ and the pilot stick side force F_Y of these uncommanded transonic lateral-directional motions are shown in figure.

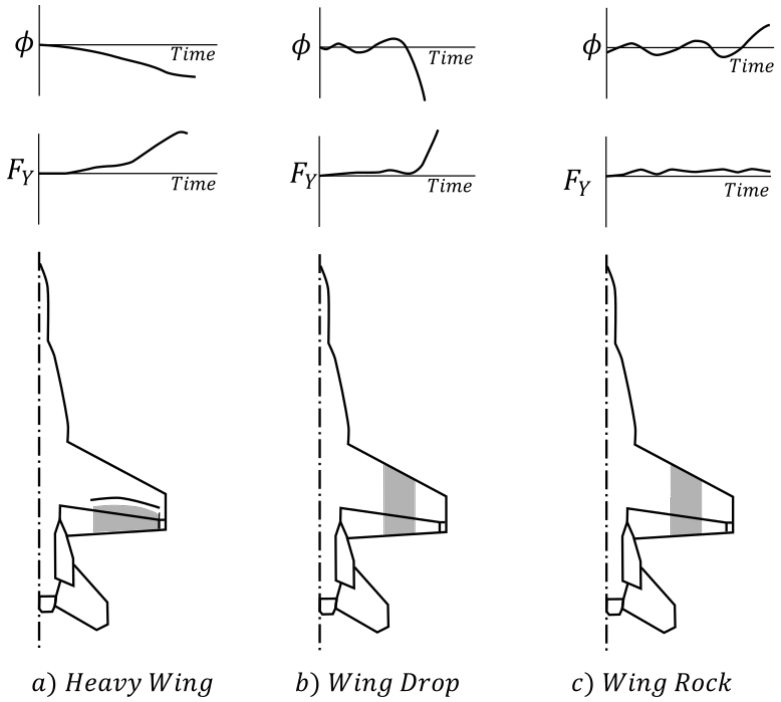

Figure 1.14: Transonic lateral-directional instabilities [46].

Those transonic lateral-directional instabilities caused by stall occur in high-performance military aircraft. F/A-18E/F experienced a wing drop in the pre-production phase, which has been corrected by leading-edge flap scheduling and a porous door for the wing fold fairing. Although this pre-production F/A-18E/F wing drop problem had been resolved, it initiated a program by NASA, the Navy, the Air Force, and the Boeing company called the Abrupt-Wing-Stall (AWS) Program [47, 48, 49]. Under this program, NASA conducted transonic free-to-roll and static wind tunnel tests for four military aircraft – the AV-8B, the F/A-18C, the pre-production F/A-18E, and the F-16C in the NASA Langley 16-Foot Transonic Tunnel. In this study, they observed 5 types of transonic lateral directional instabilities [50, 51]:

- Type I: Limit-cycle wing rock, which is a lateral oscillation with fixed amplitude.
- Type II: Wing rock with almost constant frequency and varying amplitude.
- Type III: Occasional damped wing drop and wing rock.

- Type IV: Frequent damped wing rock and wing drop.
- Type V: Divergent wing rock.

This Abrupt Wing Stall Program extended free-to-roll and static wind tunnel tests to evaluate various wing configurations of the Joint Strike Fighter (F-35) aircraft. This study concluded that sealing the gap of the leading edge decreased the lateral stability, increased roll damping, and caused an earlier break in the lift curve. Additionally, they found Vortex generators ineffective [52].

Another instability is a large asymmetric yawing moment at high angles of attack (in the range of 40° to 60°). This large moment is caused by asymmetric shedding of vortex sheets off the long pointed fuselage nose. It could be eliminated by the use of symmetrically arranged strakes on the nose [53] or by blunting the fuselage nose delays the onset of flow asymmetries to higher angles of attack [54].

Another interesting instability, known as tumbling, which usually happens in the flying wing configurations. Tumbling is defined as an autorotative pitching motion about an axis parallel to a vehicle's lateral axis, plus translation in a vertical plane along an inclined flight path [55]. Tumbling happens in flying wings because the longitudinal moment of inertia I_{xx} is larger than the lateral moment of inertia I_{yy} [43].

1.5 Spin

Spin involves complicated interactions between the aerodynamic forces and the inertial loads. It is extremely hard for the design engineer to predict these interactions because estimating the aerodynamic forces associated with the separated flows in the post-stall regime makes the design problem formidable [4]. Spin is classified into the following phases:

1. spin-entry phase [56]: It is the change from a controlled flight at the stall to the incipient-spin phase. If the yaw moment is produced following a wing drop at the stall without a proper correction rudder input, the airplane will enter spin.

2. Incipient-spin phase[56, 57, 1]: The flight path of the airplane becomes vertical, and the angle of attack increases to values higher than the critical stall angle. During this phase, the rolling rate increases from zero to the rate exhibited in the fully developed spin.

3. Developed-spin phase [56, 57, 1]: Airspeed and vertical speed and rate of rotation are almost constant. Airplane angles become repeatable from turn to turn, and the flight path is almost vertical. The spinning motion is sustained under the balance of the aerodynamic and inertial loads. The developed spin may be steady or oscillatory and distorting to the pilot.

4. Spin recovery[56, 57, 1]: recovery is accomplished by changing this fatal balance between the aerodynamic forces and the inertial loads, by applying some control surfaces' deflections. These control inputs depend on the airplane mass matrix, stability derivatives, and aerodynamic coefficients. But for general aviation airplanes, it is recommended to follow these steps [56]:

   (a) Power idle

   (b) Ailerons to be maintained at the neutral position

   (c) Rudder to be deflected in the opposite direction of spin and maintained deflected.

   (d) After the autorotation stops, the rudder is to be neutralized and the aircraft may be recovered from the dive by careful pitching.

In some dangerous cases, the spin becomes flat, i.e., the fuselage is almost horizontal, and the spin axis passes through the center of gravity of the airplane, and the spin radius is

very small. Recovery from a flat spin is extremely difficult because the control surfaces are ineffective. During the early spin flight tests, unrecoverable spins may occur. For this fatal reason, the test aircraft is equipped with a parachute to terminate the spinning motion and reduce the angle of attack to values below the stall angle. After this emergency recovery, the pilot separates the parachute and resumes the conventional flight [36].

1.6 Spin Development

The high fatality rate of unintentional stall accidents in light airplanes is likely caused by another phenomenon rather than the drop in the lift force or the sharp increase in the drag force. It is a scenario emerging from the wing drop phenomenon and is known as spin. In this section, the spin will be explained as a result of the wing drop phenomenon. In the following section, the definitions and explanations of the Federal Aviation Administration (FAA) and Civil Aviation Safety Authority (CASA), the counterpart of the FAA in Australia, will be discussed. We will discuss why these two formal definitions are incomplete and should be amended, and finally, another definition for the spin will be provided.

As discussed before, the wing drop is an asymmetric lift distribution that happens at stall. This asymmetric lift distribution is due to the inevitable uneven wing stall. At this moment of the uneven wing stall, the lift is not the only asymmetric force but also the drag. In contrast to the lift force, the drag force increases dramatically on the stalled wing and keeps its low value on the unstalled wing. This differential drag generates a huge yaw moment in a direction that steers the airplane in the same direction of the asymmetric-stall induced-roll. This favourable yaw is manifested in the stability coefficient C_{N_P} turning positive at high angles of attack [31]. Both the huge rolling moment (due to the wing drop) and the yaw moment take the airplane into a downward helical path (Fig. 1.15).

A question about fighter airplanes might also be asked, why can those fighter planes fly at high angles of attack, such as the famous Cobra maneuver, without experiencing wing drops or stalls? The wing drop happens in a very small range of angles of attack larger than the critical stall angle [41, 38]. Beyond this unstable range, the two wings become stalled, and the airplane becomes balanced under even lift and even drag forces. Certainly, the high thrust-to-weight ratio of this kind of airplane compensates for the increase in the drag force and for any loss in the lift force happening at angles of attack higher than 42-45 degrees.

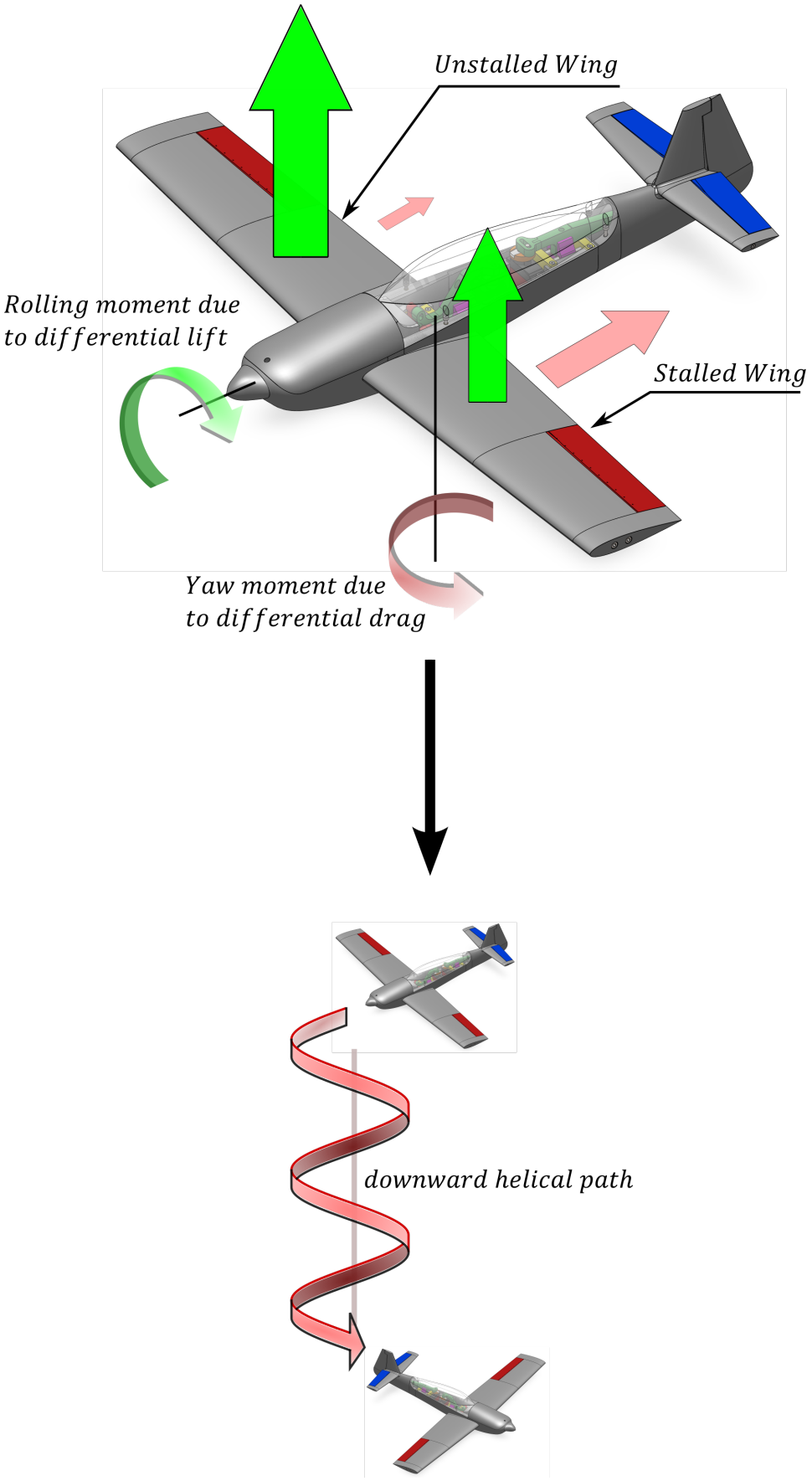

Figure 1.15: Spin development from wing drop

1.7 The Misleading Formal Definition of Spin

Spin is defined in the Airplane Flying Handbook (FAA-H-8083-3A and 3B)-Chapter 4 by the Federal Aviation Administration as [58, 59] as *" an aggravated stall that typically occurs from a full stall occurring* ***with the airplane in a yawed state*** *and results in the airplane following a downward corkscrew path. As the airplane rotates around a vertical axis, the outboard wing is less stalled than the inboard wing, which creates a rolling, yawing, and pitching motion. The airplane is basically descending due to gravity, rolling, yawing, and pitching in a spiral path"*. The yawed state mentioned in the FAA's definition can cause an early wing drop and then a spin if it exists slightly before reaching the critical stall angle, but it is not a condition to trigger wing drop and spin. Based on this research we can conclude that stalling the airplane by increasing the angle of attack to the value of the critical stall angle of attack is a sufficient ingredient to induce a wing drop followed by a spin. Usually, pilots initiate an intended spin for the sake of training by giving a rudder input at a low throttle setting while flying at a high angle of attack, slightly less than the critical stall angle of attack. This rudder input generates a yaw moment that indirectly accelerates the stalling of the inboard wing, so the pilot expects the direction of the spin. These training lessons might confuse pilots that a yaw state is mandatory to enter a spin.

In the last edition of the FAA's Airplane Flying Handbook (FAA-H-8083-3C)-Chapter 5 [1], the FAA added to this definition the statement *"Mishandling of yaw control during a stall increases the likelihood of a spin entry"*. In another context, the FAA issued an Advisory Circular in 2016 on Stall and Spin Awareness Training. In this advisory, FAA highlights a very important situation regarding the need to use ailerons and rudder to correct for the power factor and the asymmetric propeller loading in single-engine general aviation airplanes [60]. In this type of airplane, the pilot has to apply some aileron deflection to overcome the moment due to drag force on the propeller blades. This aileron deflection will change the effective angle of attack differentially on both wings, as discussed earlier, and will initiate

the wing drop even before reaching the critical stall angle. The blades of these propellers undergo changes in the angle of attack like the blades of the helicopter's main rotor, where the downward moving blade, which is usually on the right side, has a higher angle of attack due to the positive angle between the propeller axis and the air speed and vice versa for the upward moving left blade. Helicopter pilots utilize the swash plate to change the geometric angle of attack with respect to the azimuth angle of the rotor to compensate for the changes in the relative velocity of each blade with the air. The pilots of the fixed wing general aviation airplanes do not have this luxury, so they accept this deficiency in the propeller performance and apply some rudder deflection, usually to the right, to overcome the undesirable yaw moment generated by the propeller. The conclusion of this situation is aileron deflection, and rudder deflection sometimes are mandatory for maintaining the flight path. Those deflections will be dangerous near stall and may accelerate wing drop followed by a spin.

Many other resources adopt this paragraph and the inaccurate hypothesis that asymmetry sources like uncoordinated flight and deflected ailerons or rudder are required to develop uneven stall and accordingly spin. For example, the Aircraft Owners and Pilots Association, AOPA, website states *" After all, we know that a spin results from uncoordinated flight and stalled wings"* [57]. Wikipedia, in its page about stall, references the misleading paragraph of the FAA's handbook [61]. Air Facts journal for pilots links spin to the wing drop phenomenon but links the wing drop to uncoordinated flight following the FAA [62].

Another important regulating body, CASA (Civil Aviation Safety Authority), the counterpart of the FAA in Australia, issued an advisory circular No AC 61-16v1.0 on Spin avoidance and stall in 2020 [56], four years after the FAA issued their advisory circular [60]. In their advisory circular, CASA provides a conservative definition of spin and links it with the wing drop avoiding the incomplete explanation of the FAA's handbook. CASA gives another definition of the wing drop without referring to the FAA's "yaw state." CASA, in simple straight words, advises to use the elevator to unstall the stalled wing, use the rudder to over-

come the yaw moment caused by the wing drop, and avoid using ailerons at that moment. Any mishandling of the recovery from the wing drop is likely to result in a spin[56]. CASA describes the spin in a way that does not conflict with the finding of this research, like the FAA, where they state that the stalled airplane yaw will be towards the down-going wing, which has an angle of attack greater than the critical stall angle of attack. The down-going wing is stalled and produces more drag than the unstalled wing.

In his book on NASA Langley Research Center Contributions to U.S. Civil Aircraft of the 1990s, Joseph Chambers agrees with both definitions of FAA, and CASA [4]. He stated that some airplanes might develop large amplitude rolling motion, wing drop tendencies, and unexpected responses to the control commands. If these instabilities happen rapidly and in a disorienting way, pilots may lose control of the airplane and enter the incipient-spin phase. Also, Pilots can enter the Incipient-spin phase intentionally through rudder-aileron-elevator commands near stall.

Finally, we conclude that both FAA's and CASA's definitions for the spin are correct but incomplete and misleading. We recommend merging the two definitions stressing on the definition of the wing drop as an introductory phase for the spin. We propose defining spin as follows:

Spin is a sustained rotational falling motion of an airplane along a helical (corkscrew) path. Spin results from lateral-directional instability, occurring naturally at the critical stall angle. The lateral instability is known as Wing drop, which is a vast rolling moment that occurs due to asymmetrical lift distribution, while the directional instability occurs because of a yaw moment due to asymmetric drag distribution. The rolling moment (wing drop) and the yaw moment typically occur when the airplane flies at the critical stall angle without the need for any other factors. Spin could be accelerated before reaching the critical stall angle with the aid of asymmetric catalytic maneuvers/control inputs such

as aileron deflection and/or rudder deflection, side slip, side wind, dirty wing, propeller vortex, etc.

1.8 Loss of Control and Aileron Effectiveness at Stall

As part of a NASA research program on stall and spin during the 70s', Grafton et al. [63] investigated experimentally the features that affect the high-angle-of-attack characteristics of a high-performance twin-engine fighter airplane, which demonstrated excellent stall characteristics with a good resistance to spin. This airplane model was of scale 17:100, making an average Re of 650,000. It is equipped with controllable ailerons, elevator, and a rudder. They built three different wing planforms for this airplane model; tapered (the basic), swept, and delta wing. It was one of NASA program's wind tunnel airplane models. Their wind tunnel testing was divided into three categories:

- Static test somehow similar to the test we did this study. The model is mounted on a load balance. Aerodynamic forces are measured for a range of angles of attack from -5° to 45°, while the flow is visualized using tufts.
- Qualitative free-flight wind tunnel test based on the opinions of two pilots; longitudinal stability pilot and lateral and directional stability pilot.
- Forced oscillations in pitch, roll, and yaw to determine the stability derivatives. Forced oscillations were made with an angular amplitude of $\pm 50^\circ$ and an oscillation frequency of 1 Hz.

Grafton found asymmetric lift distribution at stall. This asymmetry provokes the wing drop phenomenon and the sudden yaw moment with lateral-directional divergence or nose slice. Their results show that the static directional-stability derivative was stable in the

pre-stall regime. The magnitude of this derivative decreased at stall at an angle of attack near 17°; and then it became increasingly stable in the post-stall angles regime, which is consistent with our data. Ailerons were slightly effective in the post-stall regime. The latter result is consistent with our results too. We believe the differential drag caused by the aileron deflection is the reason for this partially regained effectiveness at high angles of attack. As the downward-deflected aileron creates more drag than the upward-deflected aileron, leading to a differential drag.

The wind tunnel flight tests found that the taper wing planform without artificial damping in roll or yaw flew smoothly and with little effort by the pilots in the pre-stall regime. There was some nose wandering at stall, or directional "looseness," as noted by the lateral-directional pilot. The pilot effort was increased to fly the model smoothly because of the reduced aileron effectiveness at stall and post-stall.

The rate of stability divergence of the swept and the delta wing planforms was about the same as for the tapered planform. Since we mentioned that wing rock phenomenon, it is worth mentioning that the lateral-directional pilot noticed some oscillations in roll, the wing rock, while flying the swept wing at $\alpha = 30°$.

NASA is also conducting three wind tunnel studies on two full-scale models as part of the same program. The first study was done by Shivers et al. [64, 65] on a light single-engine low-wing airplane with maximum take-off weight of 2750 lb. Wind tunnel tests were done for a range of angle of attack from $-4°$ to $22°$ and side slip angle range of $-15-°$ to $15°$, at thrust coefficients of approximately 0.03 and 0.23. This study showed that ailerons remain effective and unaffected by flap deflection in the pre-stall regime. The data also show that the positive rolling moment generated by the ailerons decreases with increasing angle of attack. Generally, their airplane is directionally stable at stall. Ailerons and rudder are effective at stall and powerful enough to trim out all unstable rolling and yawing moments at stall. The latter result is not consistent with our finding, or the finding of the work of their colleague

Grafton [63]. Maybe they did not notice the reduced aileron effectiveness as the maximum angle of attack of this wind tunnel test was 22°. Another reason that may be attributable to this less reduction of aileron effectiveness is the relatively large aileron inboard distance (Fig. 1.16).

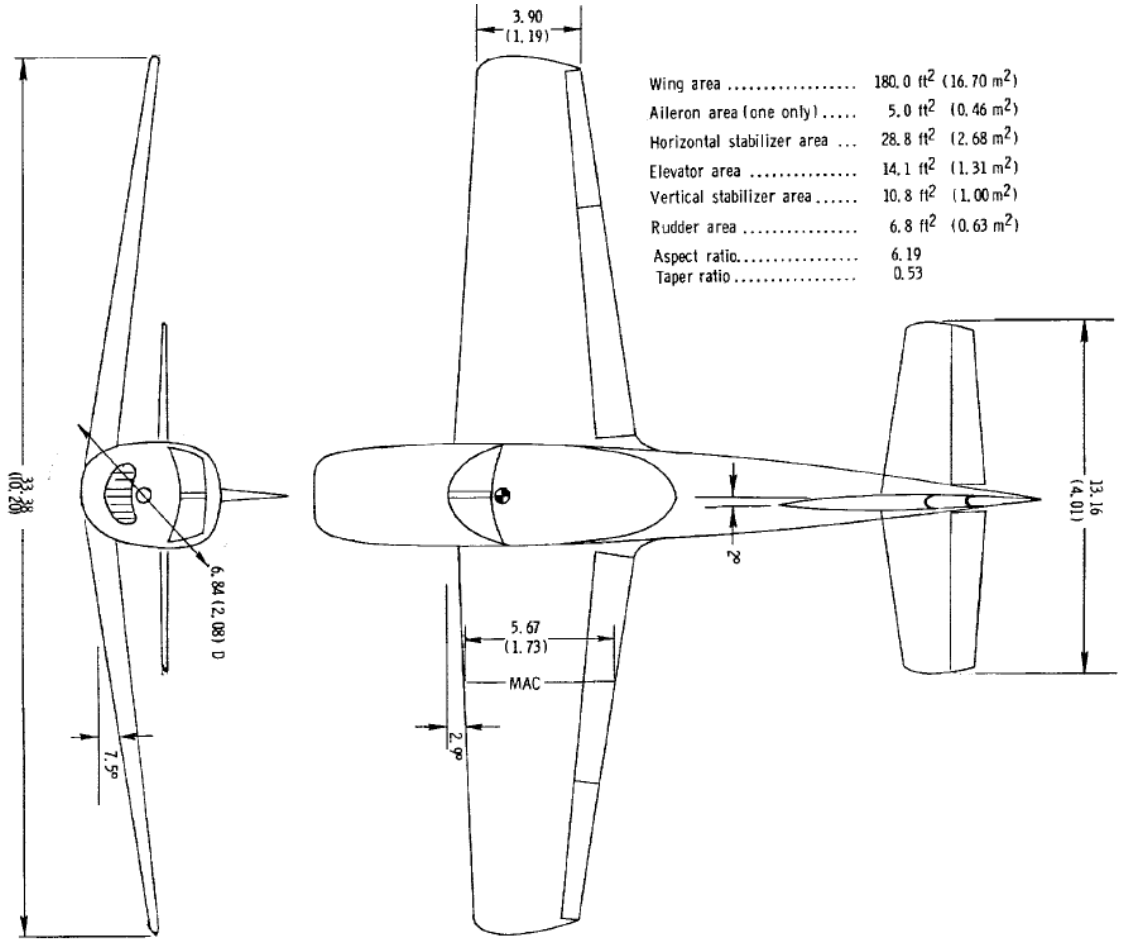

Figure 1.16: NASA full-scale light single-engine low-wing airplane for wind tunnel testing [65].

As part of the same NASA research program, Greer et al. carried out a full-scale wind tunnel experiment at Langley full-scale tunnel [66]. This airplane is also a light single-engine airplane but with a high-wing this time. The aileron inboard distance is almost the same as it was in the previous experiment, but the aileron area is increased by about 39% (Fig. 1.17.

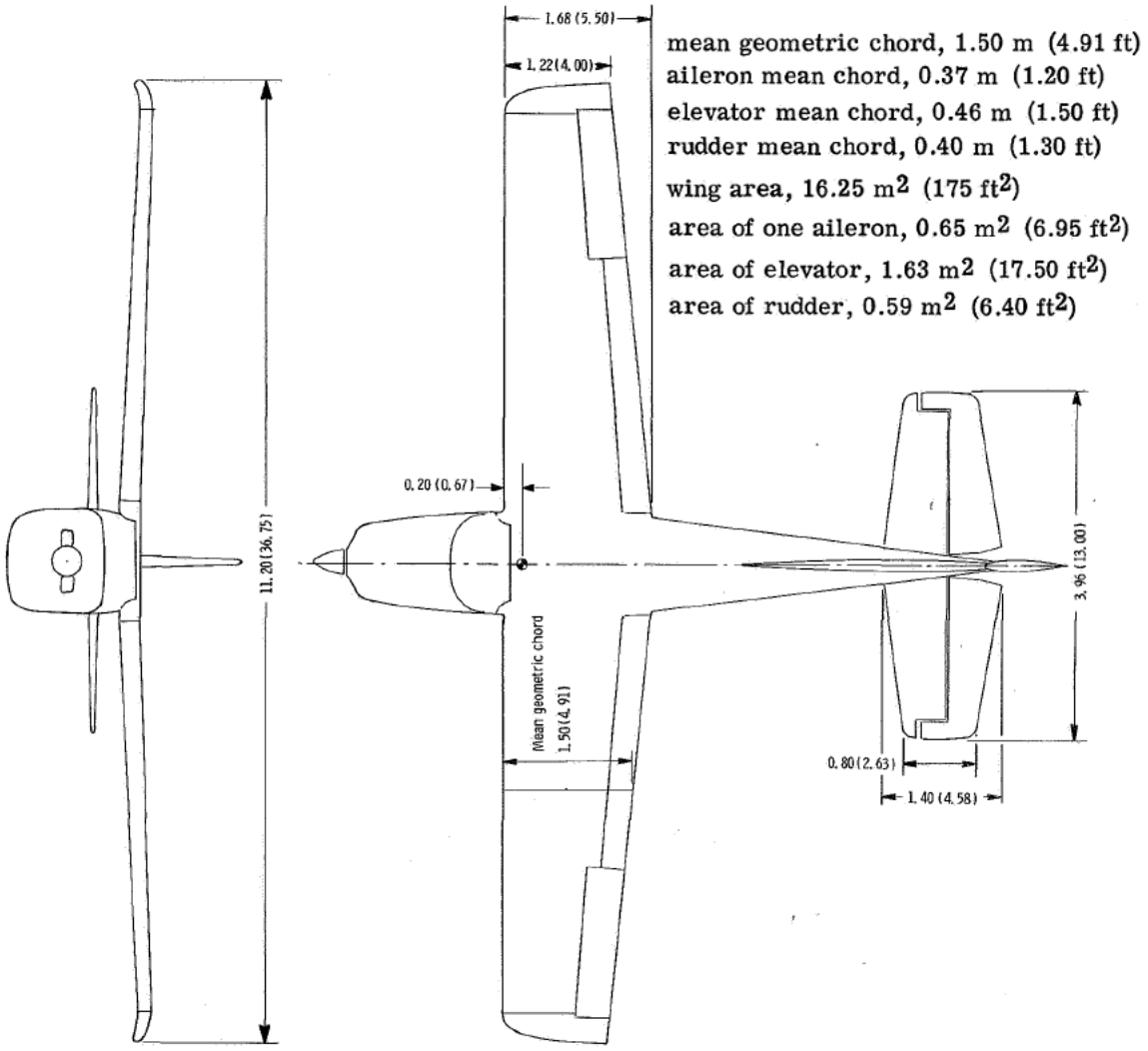

Figure 1.17: NASA full-scale wind tunnel mock-up of a light single-engine high-wing airplane [66]

Similar to the previous NASA experiments and to our experiments on different wing planforms, there is sufficient aileron effectiveness in the pre-stall regime that gradually reduces with the increase in the angle of attack. This experiment highlighted clearly that there is a large rolling moment caused by asymmetric wing stall is in line with our results. As expected, and similar to Shivers's results [65], Ailerons and rudder are effective at stall and powerful enough to trim out all unstable rolling and yawing moments at stall. Certainly, if Shivers' model exhibits good aileron effectiveness at stall, this enlarged-aileron model will

have better effectiveness.

The last NASA full-scale wind tunnel experiment to discuss in this section is done by Fink et al. on a light twin-engine full-scale airplane [67]. Like other NASA wind tunnel studies, this study was to determine the static longitudinal and lateral stability, and the wind tunnel tests were done for a range of angle of attack from $4-^{\circ}$ to 18°

Similar to all other wind tunnel experiments (including ours), ailerons are effective and fairly linear, and the airplane is directionally stable in the pre-stall regime. At the stall, large rolling and yawing moments occur. This paper agrees with our analysis that the reason for these large moments is asymmetric stall. They also use tufts to see how the stall propagates, and they found that a large part of the left wing, outboard of the engine nacelle (Fig. 1.18, stalled at $\alpha = 20^{\circ}$. The important finding of this paper is they studied the effect of the leading edge radius in the asymmetric stall. They changed the leading edge radius and repeated the experiments and found that the increased leading edge radius reduces the magnitude of the wing drop but it does not eliminate it. Aileron and elevator effectiveness is reduced at stall, although the authors gave a contradicting statement in the conclusion section by stating that "aileron and elevator effectiveness is maintained through stall."

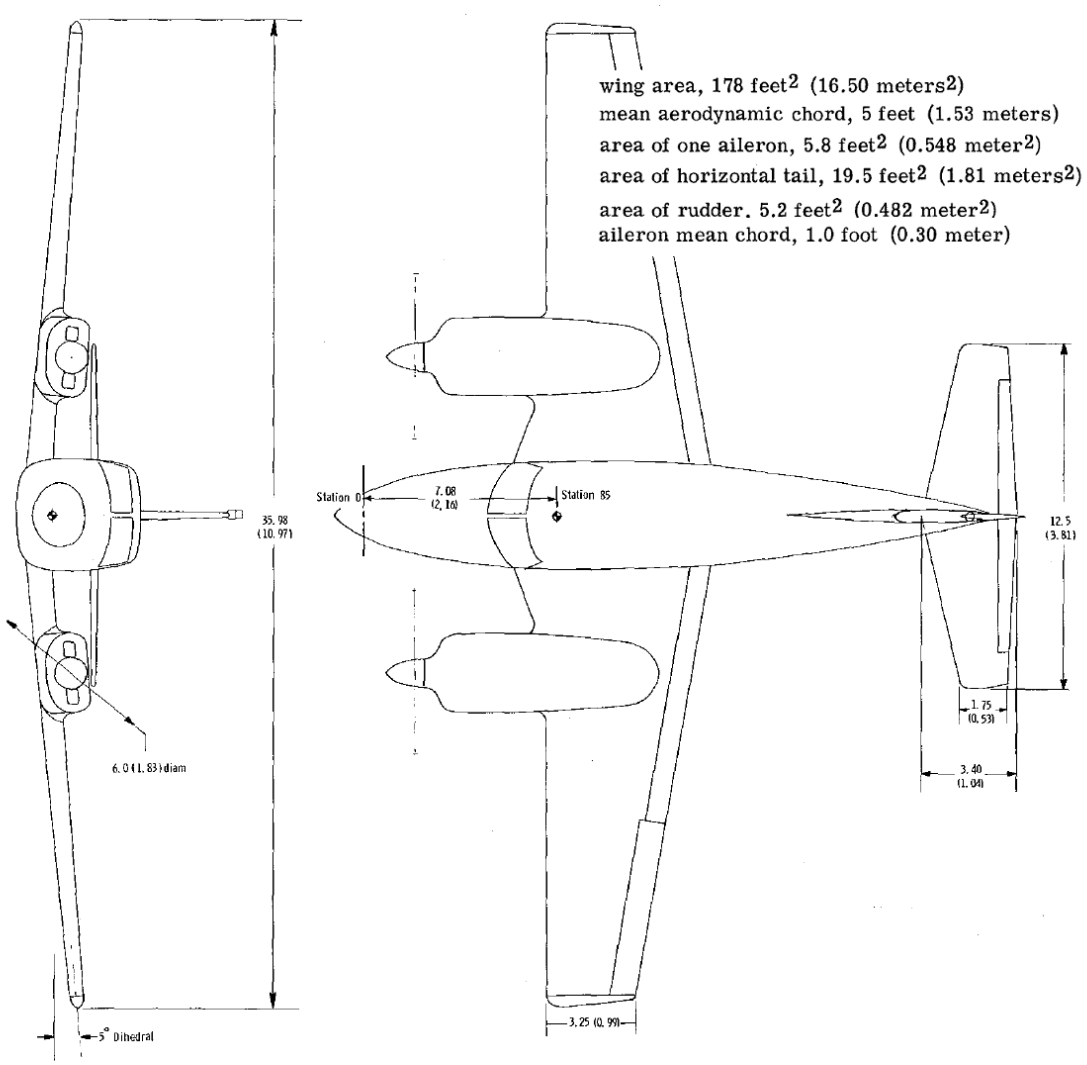

Figure 1.18: NASA full-scale light twin-engine low-wing airplane for wind tunnel testing [67].

1.9 Dynamic Stall of Rapidly Pitching Wings

As mentioned before, fighter airplanes can mitigate the effect of the wing drop significantly by pitching the airplane rapidly to jump the region of instability of the lift- α curve, where the slope of the curve is negative or rippling around the zero value. In the post-stall regime, both wings become stalled, and accordingly, the airplane becomes balanced. The drag is almost doubled, reducing the speed, which reduces the lift in a quadratic relation. The fighter

airplane has a high thrust-to-weight ratio, and pilots can increase the thrust in this post-stall regime to overcome the increased drag and compensate for the reduced lift. Different post-stall maneuvers have been developed for air combat, such as the Herbst maneuver and Pugachev's Cobra maneuver. These maneuvers require maintaining stability and control authority which could not be achieved during a small range of the angles of attack [68]. Dynamic stall boosted the interest in enhancing the handling qualities and the maneuverability of fighter aircraft in the post-stall regime[69]. This interest led to another fancy terminology of the aerospace industry; supermaneuverability, which is defined as the capability of a fighter aircraft to execute tactical maneuvers with controlled side slipping and at angles of attack beyond maximum lift [70].

This high pitching rate does not only help in passing the stall region of instability, but also it delays the critical stall angle α_{Stall} (Fig. 1.19), resulting in a stall delay in a phenomenon known as Dynamic Stall. The effect of unsteady rapid pitching on enhancing aircraft stall characteristics has been recognized by some engineers since 1950[71]. As the pitching rate increases, α_{Stall} increases [72, 8, 73]. On the opposite direction, as the pitching rate decreases, α_{Stall} decreases, resulting in lowering the critical stall angle, and this is shown in Figure 1.19 at AOA=360°. The fluid particle at the leading edge of the pitching airfoil, in this case, is like a car moving a rotating surface. If the car wants to make a turn with specific angular displacement with respect to a global stationary frame in a specific time, and the surface rotates in the same direction of the particle rotation, this will reduce the relative angular velocity between the car and the surface and accordingly it will reduce the centripetal force applied by the surface on the car tires. On the other hand, if the surface rotates in the opposite direction, the car will be required to steer rapidly and for a longer relative angular displacement with the surface to achieve the desired global angular displacement in the same specific time. This longer relative angular displacement in the same time period would create a greater centripetal force, which may lead to flipping of the car if it exceeds a certain critical value. When the wing pitches up, it reduces the relative angular displacement between the

fluid particle and the leading edge of the airfoil, so the fluid particle can keep moving on the surface without separation. But if the wing pitches down, the fluid particle need more centripetal force to stay attached to the wing surface at the leading edge because of the higher relative angular velocity. If AOA exceeds the delayed α_{Stall}, the fluid particles separate from the surface, creating a strong vortex known as a Leading Edge Vortex (LEV) during this unsteady motion [7, 8]. This vortex moves downstream over the upper surface of the airfoil, distorting the pressure gradient and producing transient aerodynamic forces and moments that are different from their static stall counterparts [74, 75, 76]

In our experiment on pitching airfoils over an angle of attack range from 0° to 360° and pitching rate from 1.8°/sec to 360°/sec (Fig.1.19), we found that pitching up the airfoil or even a reversed airfoil delays stall and increase the critical stall angle while pitching down both the normal and the reversed airfoil decreases the critical stall angle as follows:

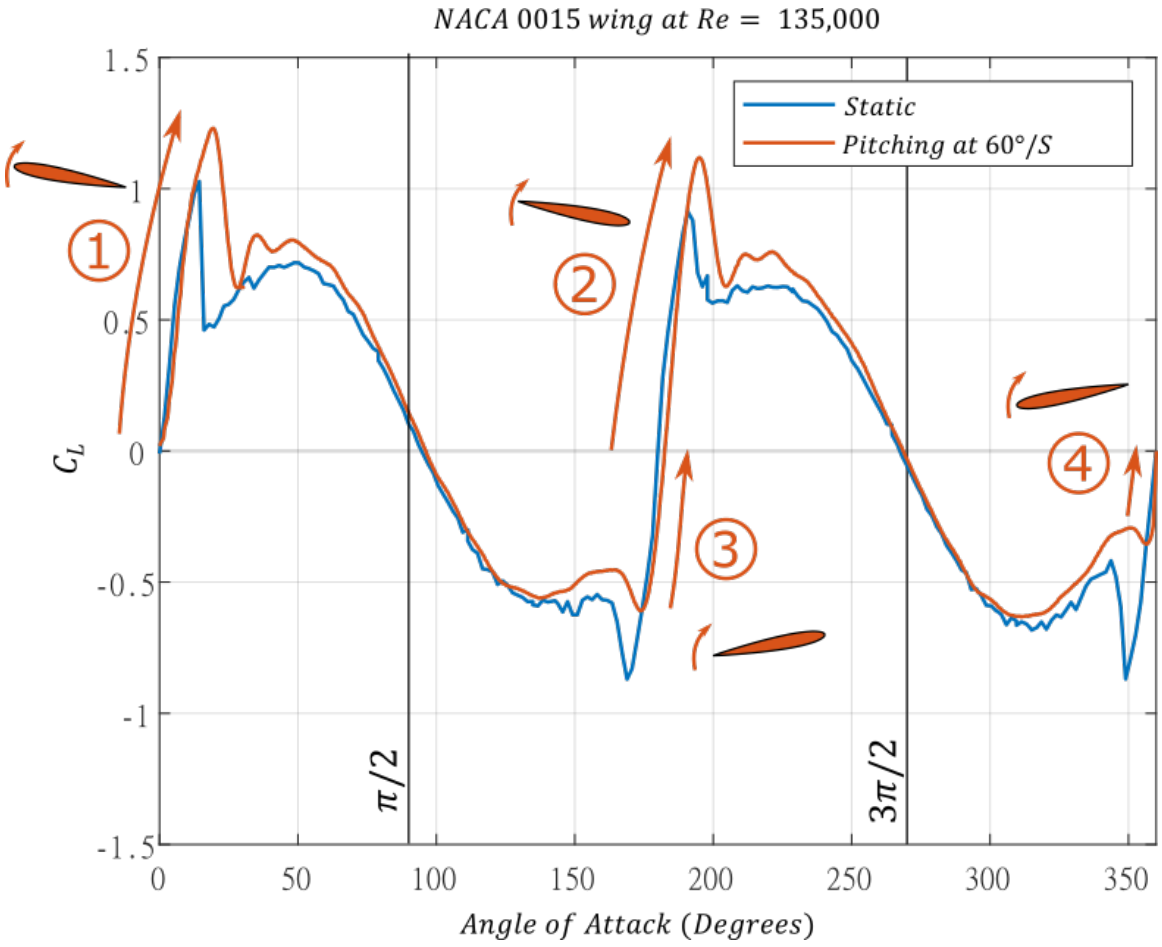

Figure 1.19: Dynamic stall $C_L - \alpha$ curve. Wind tunnel experiment of pitching NACA 0015 from 0° to 360° pitching rate of $60°/sec$.

1. Pitching up airfoil from 0° to 90° (Fig.1.19-1): Both the critical stall angle α_{Stall} and the maximum lift coefficient $C_{L_{max}}$ increase.

2. Pitching up a reversed airfoil from 180° to 270° (Fig.1.19-2): Both the critical stall angle α_{Stall} and the maximum lift coefficient $C_{L_{max}}$ increase.

3. Pitching down a reversed airfoil from 90° to 180° (Fig.1.19-3): Both the critical stall angle α_{Stall} and the maximum lift coefficient $C_{L_{max}}$ decrease.

4. Pitching down a airfoil from 270° to 360° (Fig.1.19-4): Both the critical stall angle α_{Stall} and the maximum lift coefficient $C_{L_{max}}$ decrease.

If the wing stops pitching, i.e., the pitching rate becomes zero, after exceeding the static α_{Stall} and before reaching the delayed α_{Stall} caused by dynamic stall, the stall happens suddenly. Based on that, we can conclude that rapid pitching could be used to "bypass" this region of instability from the lift- α curve and avoid wing drop and the consequent spin during pitching up. It is like moving on the enhanced lift- α curve of the dynamic stall while pitching up and suddenly jumping to the static lift- α curve, avoiding moving across the region of instability right after the static α_{Stall} (Fig. 1.20). Fortunately, the same maneuver could be achieved during pitching down to avoid this region of instability to bring the balanced, stalled airplane to another balanced, yet unstalled, state without triggering instability. This technique could be achieved by rapidly pitching down the stalled airplane to an angle of attack lower than the static α_{Stall} and stop pitching to restore an attached flow around the wing and jump to the static lift- α curve.

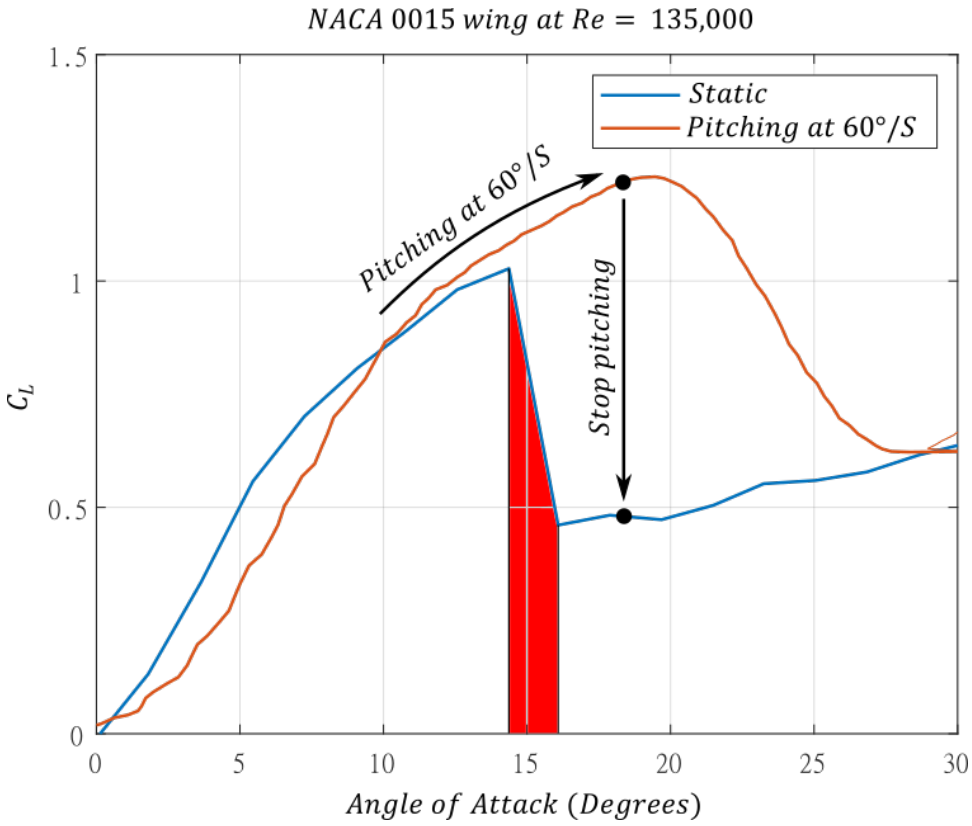

Figure 1.20: Stall instability region avoidance by high pitching rate during pitching up.

The attention to dynamic stall outgrew rapidly in the 60s when design engineers found large contradictions between the performance and aerodynamic models of helicopter blades[72, 77]. Helicopter blades undergo rapid flapping motion because of the time-varying angle of attack, especially during the high forward speeds. As advancing blade operates at a relatively low angle of attack but at a high Mach number close to its shock wave limit for flow separation. The retreating blade operates at much lower Mach numbers but at relatively high values of angle of attack close to the critical stall angle. The angle of attack of each blade element is time-varying because of blade flapping, cyclic and pitch inputs. Flow separation and stall become dynamic and time-dependent too. The dynamic stall will occur on an airfoil that is subjected to unsteady pitching, plunging or surging motion [78].

This flapping motion and the dynamic stall generate severe dynamical loads on the blades, the rotor hub, the swash plate, and the actuators. The large amplitude oscillations caused by these dynamical loads generate unsteady three-dimensional effects on both the advancing and the retreating blades [75]. Helicopter design and operation continue to be challenged by the emerging large transient loads encountered at high forward speeds [79].

Helicopter rotor and the high α maneuvers of the fighter aircraft followed by a new rising application, wind turbines, mandated the need of a robust model for better prediction of the dynamic stall and the associated unsteady aerodynamic loads [7]. The situation was worse in the wind turbines field than others, where the life span was far below the predictions [80, 81]. Many researchers found that dynamic stall happens when the wind turbine blade passes through the shadow of the wind turbine tower and due to rapid yaw motion[82, 83, 84, 85].

Designers needed robust and reliable models for separation prediction to solve the problems of helicopter rotors and wind turbines as well as to expand the flight envelope of fighter airplanes. Banks in 1962 [86] was one of the first to develop an aerodynamic model to predict the laminar separation of rotating blades.

Leknys et al. [87]studied the flow structure and surface pressure of NACA 0021 airfoil tested under a constant pitching rate and multiple reduced frequencies (k) up to different maximum angles of attack. At the beginning of airfoil rotation, force generation is delayed, and the delay angle increases with the increase of the reduced frequency. Increasing the reduced frequency generally increases C_{Lmax} in most cases. Both results are in line with the results of this study. The delay was mainly attributed to the response delay of the low pass filter (LPF) used to filter the load balance signals. The delay in the response of the aerodynamic force could not be assessed due to the significant delay of the LPF. The cut-off frequency of the LPF could not be increased to minimize the delay, as the maximum cutoff frequency is constrained by the structural response of the experimental setup.

This study found separation is also sensitive to k and α_{max}[87]. For an angle of attack amplitude $\alpha_{max} = 40$ and $k = 0.05$, complete separation is observed at $\alpha = 20°$ where the leading edge vortex (LEV) begins shedding into the free stream. For higher reduced frequencies, k=0.1 and 0.2 lift are maintained until $\alpha = 40°$, which equals the amplitude in this case. The LEV begins to detach as soon as the trailing edge vortex (TEV) forms, causing the reduction of C_{Lmax}. The same study found for k=0.2, Increasing $alpha_{max}$ to 60∘ delays the separation up to $alpha = 55°$ after which a secondary TEV is formed, promoting the separation of LEV and the vortical structures. For k=0.05,0.1 the situation is similar to α j=40. We believe the attribution of this research is not fully correct, as the reduced frequency is the only parameter that controls the stall angle α_{stall} for the same wing and the same Reynolds number. If $alpha_{max}$ in this experiment is less than α_{stall} of this reduced frequency, the stall will happen at this $alpha_{max}$ as the wing becomes static at $alpha$ higher than the static α_{stall}. Changing the amplitude of the pitching motion allows an inaccurate interpretation that $alpha_{max}$ is an effective parameter.

In their study, Benton et al. [88] performed a large eddy simulation on a pitching NACA0012 at $Re = 10^6$ with different pitch rates. This study found that the length of

the laminar separation bubble (LSB) depends primarily on the airfoil and α while the pitching rate has a limited effect. The interesting result of this study is that the pitching rate has little effect on the delay of the onset of the dynamic stall on NACA 0009. In contrast, it noticeably delays the onset of the dynamic stall of NACA 0012. This study attributes the delay of the NACA 0012 to the insufficient pressure gradient that couldn't propagate upstream to interact with the LSB.

The same authors of the previous papers performed another Large-eddy simulation to study the effect of the leading edge radius on characteristics of the onset of the dynamic stall for four NACA airfoils at $Re = 2X10^5$ [89]. The increase of the leading edge radius and the addition of a leading edge droop delay the onset of dynamic stall by reducing the susceptibility of the LSB to pressure gradient-induced bursting. For NACA 23012, the dynamics stall occurs due to the development of the turbulent separation from the trailing edge upstream to the LSB. This indicates that the bubble has been stabilized to pressure-gradient-induced bursting until the TS reaches the LSB.

Bangga et al. [90] carried out a computational investigation on seven NACA airfoils to study the effect of airfoil thickness on the dynamic stall of high solidity vertical axis wind turbines (VAWTs) [90]. The leading edge vortex bubble is found to be the main cause of power loss for high solidity VAWTs.It is also found that increasing the thickness to chord ratio reduces the thrust up to 40% due to the reduction of suction peaks, yet it also increases the power coefficient up to 25-30 % before the trailing edge separation gradually reduces this effect. Although the effect of the dynamic stall is found to decrease with increasing the thickness to chord ratio, the study recommends using medium airfoil thickness ranging from 18 to 30 % because the thicker airfoils suffer from trailing edge separation even at small angles of attack.

Using both experimental and computational methods, S.Guntur et al. (2015) [91] analyzed the dynamic stall and the rotational augmentation separately on the inboard parts of

experimental wind turbine blades. They presented a method for estimating the AOA on a rotating/pitching blade, and the estimates were used as inputs to the dynamic stall model of Hansen et al.(2004) [92]. The model provides reasonable results at low K values and over-predicts torsional aerodynamic damping at higher K values. However, their dynamic stall model, when used along with a robust preprocessor for rotational augmentation in BEM-based aeroelastic codes, is said to provide reasonable estimates for unsteady aerodynamic loads on wind turbines subject to constraints imposed by flow field flow physics and model physical fidelity.

Adema et al. (2020) [93] suggested improvements to Snel model through experimental data that could predict the amplitude and frequency of vibrations more closely to the measured data. The normal force distributions also matched the results of earlier turbine design codes, yet the mean value of the normal force was not correct. Since their model is based on variations in angles of attack, the authors recommended further research to adapt this model to dynamic variation in inflow velocity for the case of rotating and vibrating blades.

Holierhoek (2013) [94], used three dynamic stall models, namely, the ONERA model, the Beddoes–Leishman model, and the Snel model, to simulate available experimental data to compare their prediction capabilities. Although it was found that using any of these models will improve the calculations compared with using steady lift coefficients, there is no model that outperforms the other two in all cases, and all of these models have limited accuracy, especially in the deep stall regime.

McCroskey et al. (1976) [74] studied the dynamic stall and the unsteady boundary-layer separation on NACA0012 with varying leading edge geometry which was oscillated sinusoidally at moderately large Re, and three different types of boundary-layer separation were observed. The dynamic stall was found not to originate with the bursting of a laminar separation bubble, as is commonly believed, but with a breakdown of the turbulent boundary layer. Vortex shedding has been observed for all airfoils, yet with significant differences in

the dynamic loads.

Pla Olea [95] applied the tools of the geometric control theory to break the symmetry to generate forces in non-intuitive directions. This study applied these tools to the unsteady aerodynamics of a harmonically pitching-plunging airfoil based on Beddoes-Leishman model. This model is a semi-empirical model that represents the unsteady lift, drag, and pitching moment of a two-dimensional airfoil [96]. This study expects to lift and drag enhancement if the wings oscillate at these angles of attack of $C_{L_\alpha} = 0$ with certain frequencies and amplitudes. This result was validated by numerical simulations using the Improved Delayed Detached Eddy Simulation (IDDES) solver.

Khalifa et al. compared different solvers for dynamic stall simulation [97]. It was found that the dynamic stall vortex creation and bursting depend highly on three-dimensional turbulent effects. Moreover, a solver that is capable of resolving different scales in the turbulent boundary layer is a must for capturing different phenomena to accurately predict various forces. All of the above leads to the fact that a high-fidelity scale resolving modeling technique is required for dynamic stall modeling, and averaging models do not suffice.

Chapter 2

Experimental Setups

2.1 Airplane Stability and Control Authority at Stall Experimental Eetup

2.1.1 Airplanes Models

Five airplane models with five different wing planforms were designed to withstand the high aerodynamic loads associated with high angles of attack wind tunnel testing. The trapezoidal wing planform, which was the first one to build, and the fuselage are a scale of 7:100 of the aerobatic monowing airplane Extra EA-300 [98, 99] without matching many parameters such as wing cross-section, sweep angles, dihedral angle, and wing position to the fuselage. This odd scale has been selected to maximize the airplane model's size without affecting the safe spacing between the model and the walls of the wind tunnel test section. Extra EA-300 has been selected because of its outstanding aerobatic performance and because it is equipped with a symmetrical airfoil like the one used in this experiment. These airplane models were made of Polycarbonate/Acrylonitrile Butadiene Styrene (PC/ABS) alloy [100, 101] to

maximize the strength of the 3D printed parts. The fuselage, the wing, and the tail are split into small components to ease the 3D printing process. All non-controllable components have been glued together using thin CA. Carbon fiber rods are used to align the fuselage and wing parts during the welding process and then to reinforce the welded section. The wing is composed of three irremovable components which are glued together, and then the whole wing is glued to the fuselage. The assembled parts and the removable parts were post-processed by fine sanding and painting with matt black for future flow visualization. The wing and the fuselage are reinforced with two removable ϕ6 mm carbon fiber spars (Fig. 2.1). These two high-stiffness spars transfer all aerodynamic loads on the airplane model, mainly the wing, to the load balance through a metallic mount. Servo motors and the driving mechanisms, including the pushrods, are installed in the fuselage to keep the surfaces of the wing and the tail clean of any objects that may cause any unneeded turbulence. Wing tips and horizontal tips are removable to install the ailerons and the two elevator's halves from the side and engage them with the driving mechanism Fig. B.2). The aluminum mount is attached to the airplane model at four distributed points, including the two wing CF spars, to increase system overall stiffness and torsional rigidity (Fig. 2.3).

2.1.2 Wing Planforms of the Five Airplane Models

Figure 2.4 shows the planforms of the five airplane models. Aileron inboard distance is the same for the five airplane models; in order to properly compare the rolling moment coefficient of the five airplanes, Aileron planform is the same for the rectangular, delta, and hybrid wing planforms. Aileron planform is slightly different from the tapered wing planform because of the swept forward trailing edge and from the Zimmerman because of the elliptical profile of the trailing edge. This change in the aileron profile slightly affects the aileron centroid to centroid distance (Table 2.1). The location of aileron rotational axis of the five airplane models is at the same location with respect to the fuselage and the tail. Therefore, the

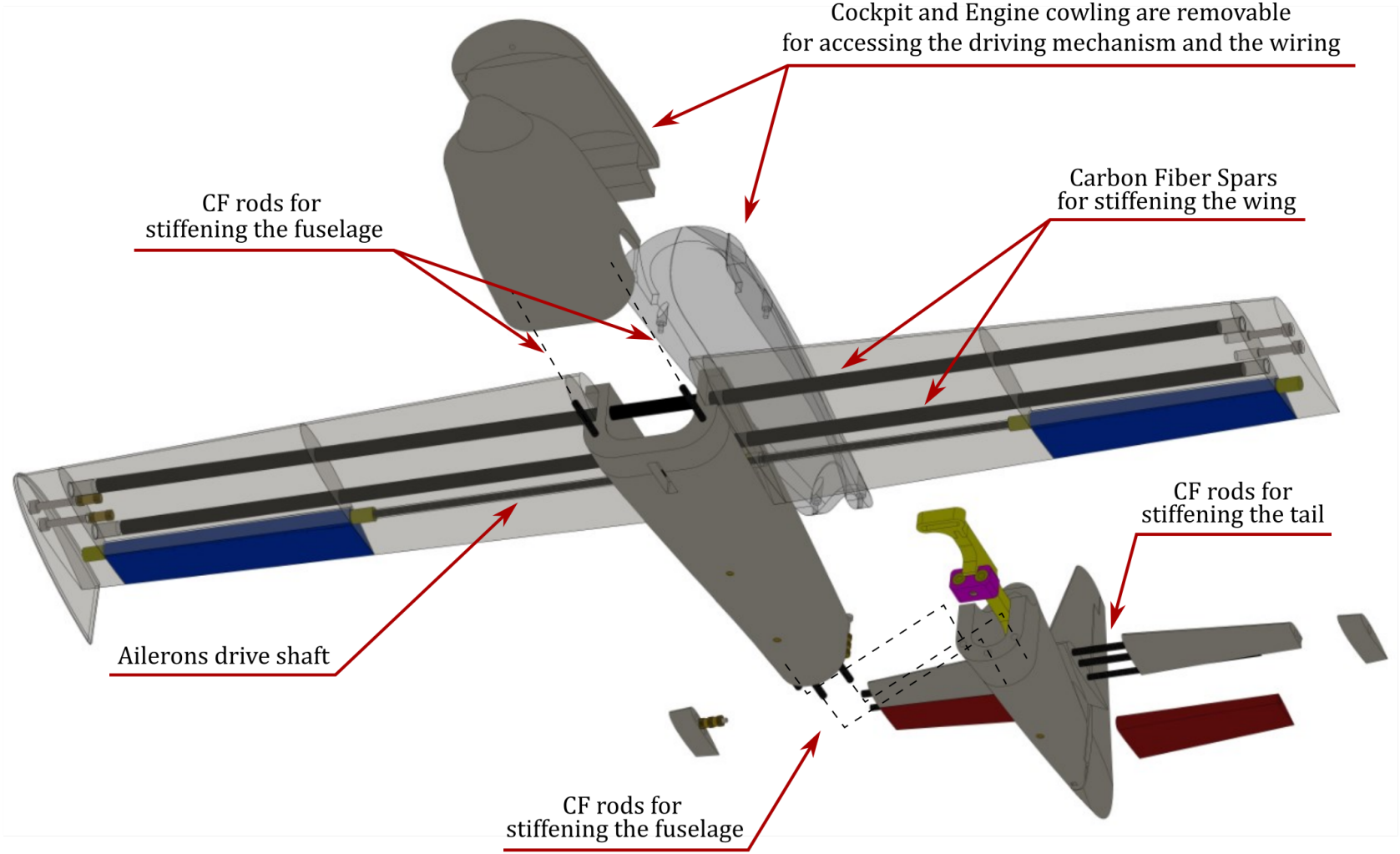

Figure 2.1: Exploded view showing the airplane components the internal reinforcing structure.

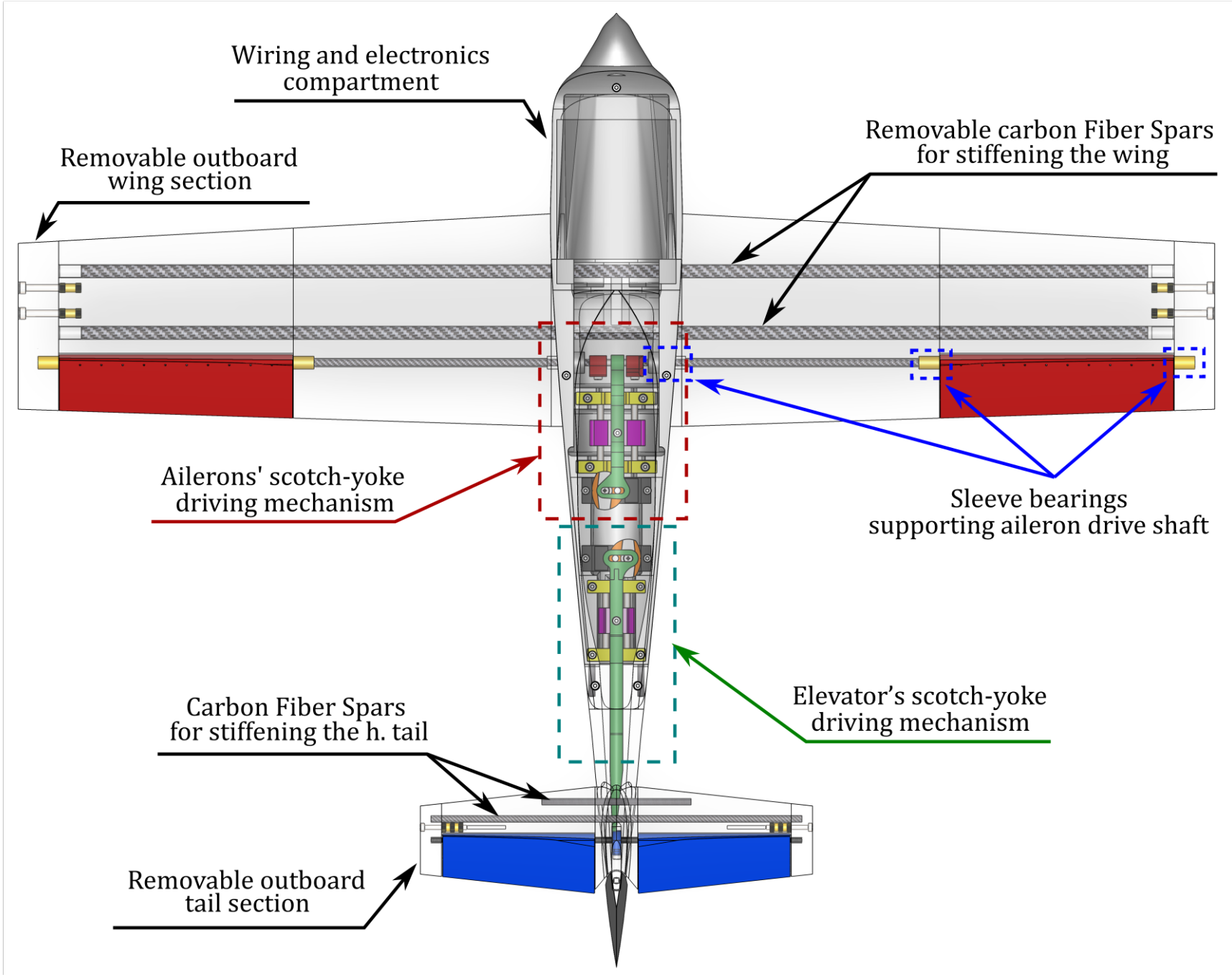

Figure 2.2: Control surfaces driving mechanisms arrangement.

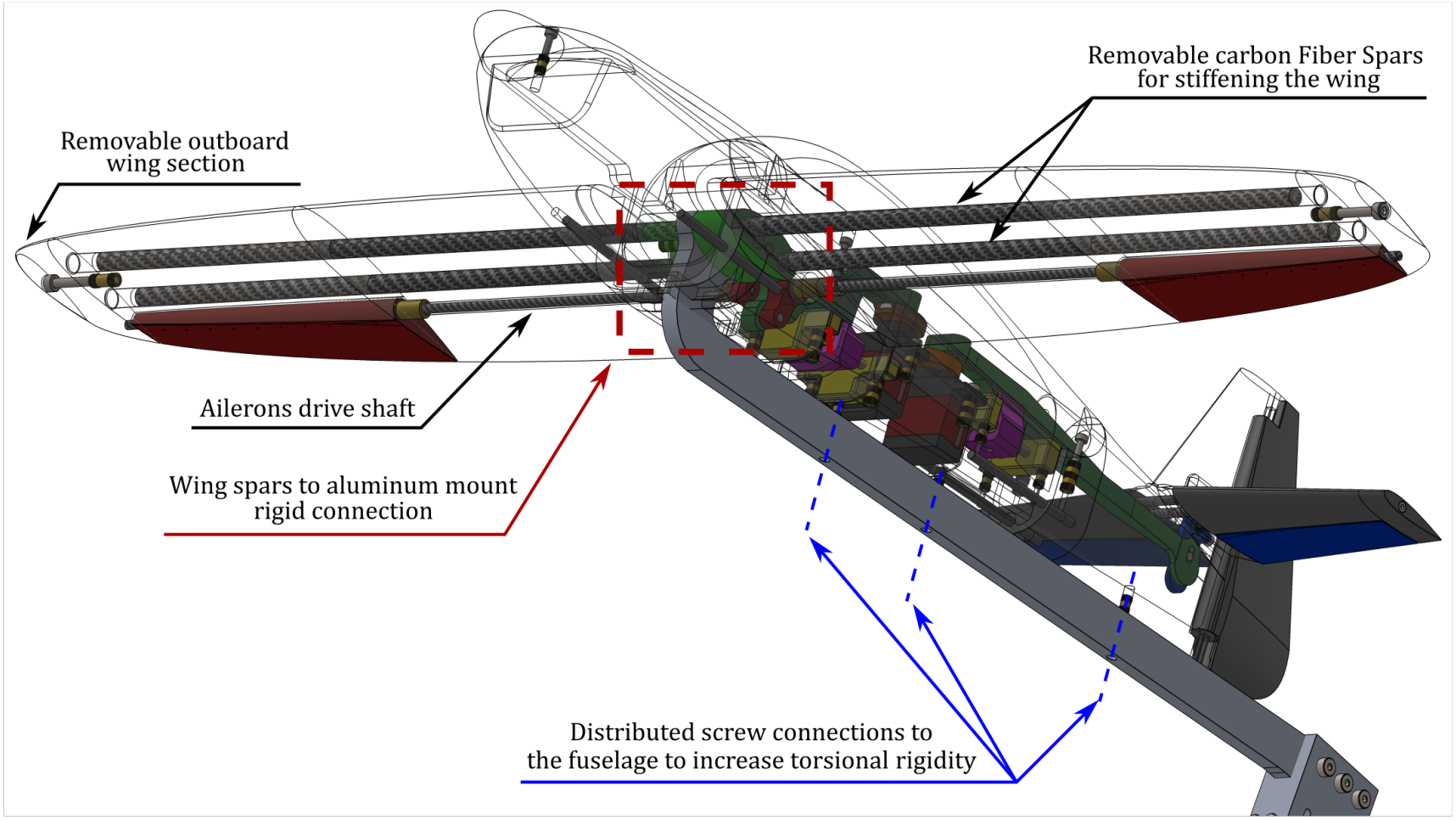

Figure 2.3: Airplane model to the load balance assembly.

aileron rotational axis is the reference point for calculating the pitching moment.

The parameters of five wing planforms are listed in table 2.1 with the overall dimensions, Reynolds number leading trailing edges profiles, ailerons dimensions, area, and locations. Table2.2 lists tail and elevator characteristics which are the same for all airplane models.

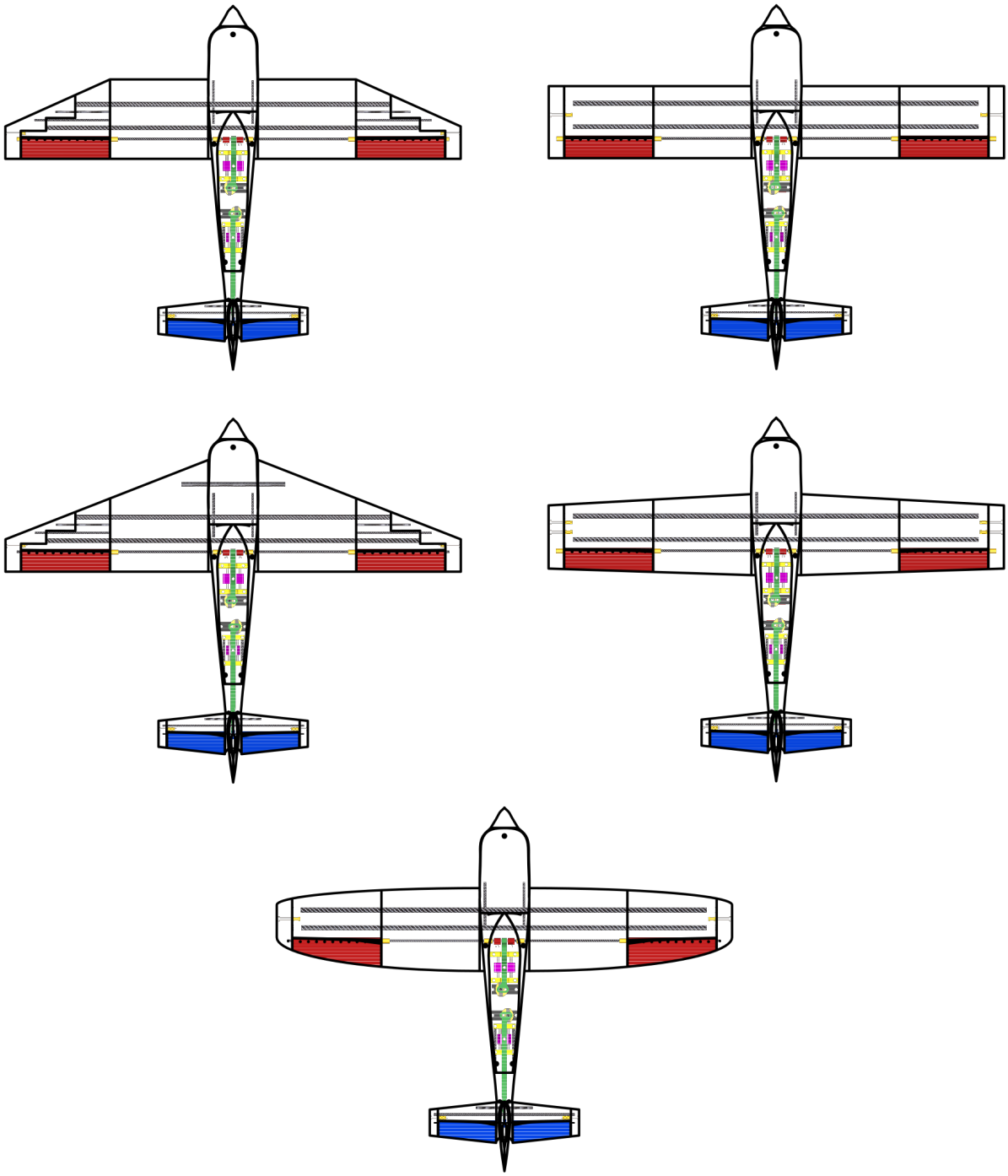

Figure 2.4: Wing planforms of the five airplane models.

Wing Parameter:	Rectangular Straight	Tapered	Hybrid: Rectangular /Tapered	Cropped Delta	Cropped Zimmerman
Cross-Sectional Airfoil	NACA 0015				
Span b (mm)	561.2				
Angle of Incidence Deg	4.0				
Root Chord C_r (mm)	89.0	100.0	105.0	138.0	102.4
Tip Chord C_t (mm)	89.0	78.0	40.0	40.0	a4=40
Mean Aerodynamic Chord MAC (mm)	89.0	84.1	75.0	75.6	91.2
Aspect Ratio (AR)	6.31	6.22	6.23	5.95	6.20
Taper Ratio λ	1.00	0.78	0.38	0.29	0.39
Wing Average Reynolds Number Re_{avg}	162,000	153,000	137,000	138,000	166,000
Leading Edge Sweep Back angle (deg)	0.0	3.2	24.2 from 65% to 100% of the span	21.4	a1=20.83
Trailing Edge Sweep forward angle (deg)	0.0	1.9	0.0	0.0	a2=41.54 a3= 41.54
Area S (mm^2)	49,946.8	50,620.0	50,541.0	52,945.6	50,763.0
Fuselage area (mm^2)	4,899.5	5,505.0	5,780.3	7,596.9	5,636.0
Aileron Area (mm^2)	3,077.0	3,077.0	3,077.0	3,077.0	3,078.4
Ailerons Area to Wing Area Ratio	13.7%	13.6%	13.7%	13.6%	13.6%
Single Aileron Span (mm)	109.5	109.5	109.5	109.5	109.5
Ailerons span to wingspan Ratio	39.0%	39.0%	39.0%	39.0%	39.0%
Aileron Root Chord (mm)	28.1	29.9	28.1	28.1	36.0
Aileron Tip Chord (mm)	28.1	26.3	28.1	28.1	15.6
Aileron to Wing Chord Ratio	31.6%	33.4%	37.5%	37.2%	28.3%
Aileron Inboard Span b_ai (mm)	303.7	303.7	303.7	303.7	303.7
Aileron area Centroid to Centroid Distance (mm)	413.2	410.9	413.2	413.2	400.8

Table 2.1: Wings characteristics of the five airplane models.

Cross-Sectional Airfoil	NACA 0015
Span b (mm)	184
Angle of Incidence Deg	2.0
Root Chord C_r (mm)	50.0
Tip Chord C_t (mm)	32.0
Mean Aerodynamic Chord MAC (mm)	37.4
Aspect Ratio (AR)	4.46
Taper Ratio	0.64
Reynolds Number Re	68,000
Leading Edge Sweep Back Angle (deg)	6.3
Trailing Edge Sweep Forward Angle (deg)	6.3
Area S (mmˆ2)	7,588.6
Vertical Tail (mmˆ2)	864.6
Wet Area (mm^2)	6,724.0
Tail Wet Area to Wing Wet Area Ratio	0.15
Elevator Area $((mm^2)2)$	3,031.0
Elevator Area to Tail Area Ratio	45.1%
Elevator Span (mm)	72.0
Elevator Root Chord (mm)	25.0
Aileron Tip Chord (mm)	17.0
Aileron to Wing Chord Ratio	50.0%

Table 2.2: Tail same characteristics of the five airplane models.

2.1.3 Cropped Zimmerman Wing Formation

Zimmerman wing planform (Fig.2.5) is formed using two different elliptical equations; one for the leading edge and a different elliptical equation for the trailing edge, according to the following parametric equations

$$y_{L.E./T.E.} = y_{T.E.} = a_3 sint \tag{2.1}$$

$$x_{L.E.} = a_4 + a_1 cost \tag{2.2}$$

$$x_{T.E.} = -a_2 cost \tag{2.3}$$

The leading and trailing edges do not intersect at the wing tip, which is cropped to give sufficient space to mount and support the aileron. The tangents of the leading edge and the trailing edges at the wingtip are perpendicular to the wingspan. The chord at the tip of the wing equals the spacing between the two major axes of the elliptic profiles of the leading and tailing edges.

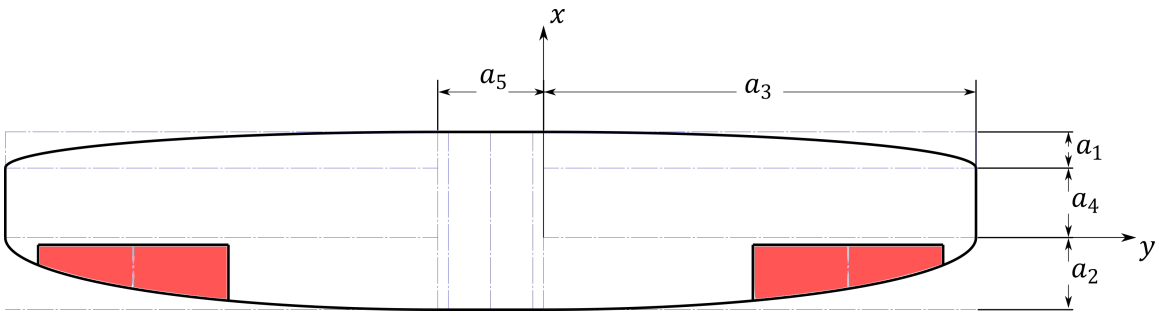

Figure 2.5: Zimmerman wing planform formation.

2.1.4 Control Surfaces Driving Mechanism

Two high-torque micro servo motors are used for controlling the elevator and the ailerons. A scotch yoke mechanism (Fig.2.6)is selected as a basis for designing the mechanism to ensure the same deflection for each aileron surface while moving in opposite directions. A Crank-Rocker mechanism (Fig.2.7 was selected at the beginning to avoid the high friction associated with the slotted joints. Later the design was changed to the scotch yoke mechanism for its

simple transfer function [102] between the servo crank angle and the control surface deflection angle:

$$\delta_A = \arcsin\left[\frac{r_c \sin\theta_c}{r_a}\right] \tag{2.4}$$

where δ_A, and θ_c are the aileron deflection, and servo motor angles, respectively, and r_c, and r_a are the servo motor crank and control surface horn radii, respectively.

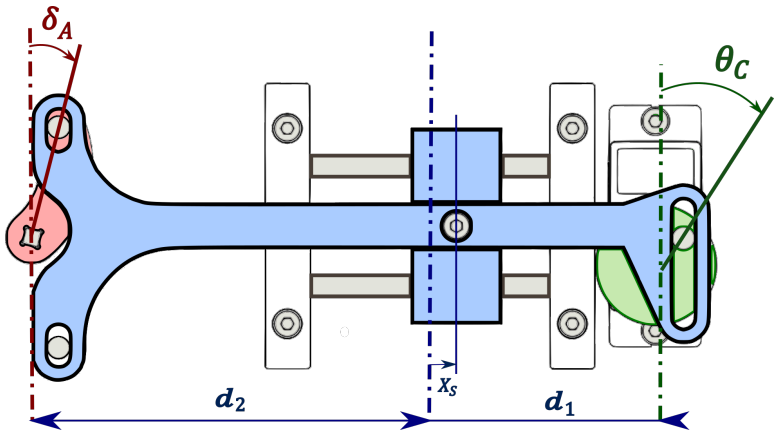

Figure 2.6: The control surfaces driving mechanism based on the scotch-yoke mechanism.

2.1.5 Experiment Configuration and Model Mounting

An aluminum mount fixes the airplane model to the load balance. This load cell is fixed at the top end of the sequential Four bar mechanism of the wind tunnel horizontal model position system (MPS). The two $6mm$ carbon fiber spars are in transitional fit with the aluminum mount inside the fuselage. Then mount is routed outside and underneath the fuselage towards the aft of the airplane model to be secured with the load cell using two $6mm$ shoulder bolts. Moreover, the mount is bolted to the fuselage at three points for additional yaw and rolling stiffness. The load balance is secured to the two ends of the

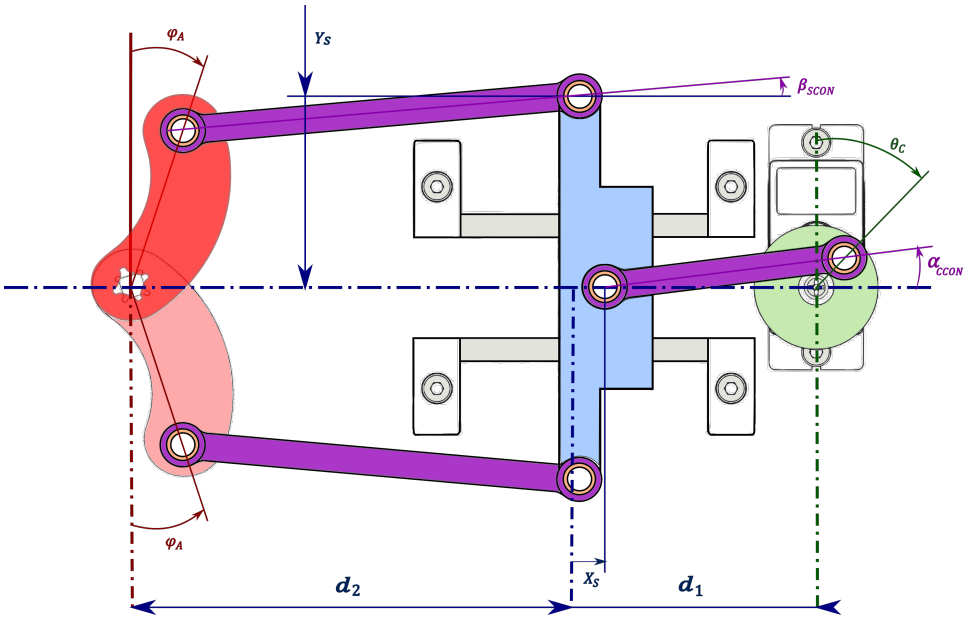

Figure 2.7: Another control surfaces driving mechanism based on the crank-rocker mechanism.

model positioning system using two-barrel screws (Fig. 2.8)

2.1.6 Generalized Forces Transformation

The transformation from the body system of axes of the load balance to the global system of axes of the wind tunnel to calculate; Lift, Drag, Rolling Moment, and Pitching according to figure 2.9 follows the homogeneous transformation matrix in equation 2.5:

$$\begin{pmatrix} D \\ L \\ \mathcal{L} \\ \mathcal{M} \end{pmatrix} = \begin{pmatrix} \cos\alpha & -\sin\alpha & 0 & 0 \\ \sin\alpha & \cos\alpha & 0 & 0 \\ 0 & 0 & -1 & 0 \\ -d_z & d_x & 0 & 1 \end{pmatrix} \tag{2.5}$$

The pitching moment is calculated around the lateral axis passing by the $\frac{1}{4}$ c point of

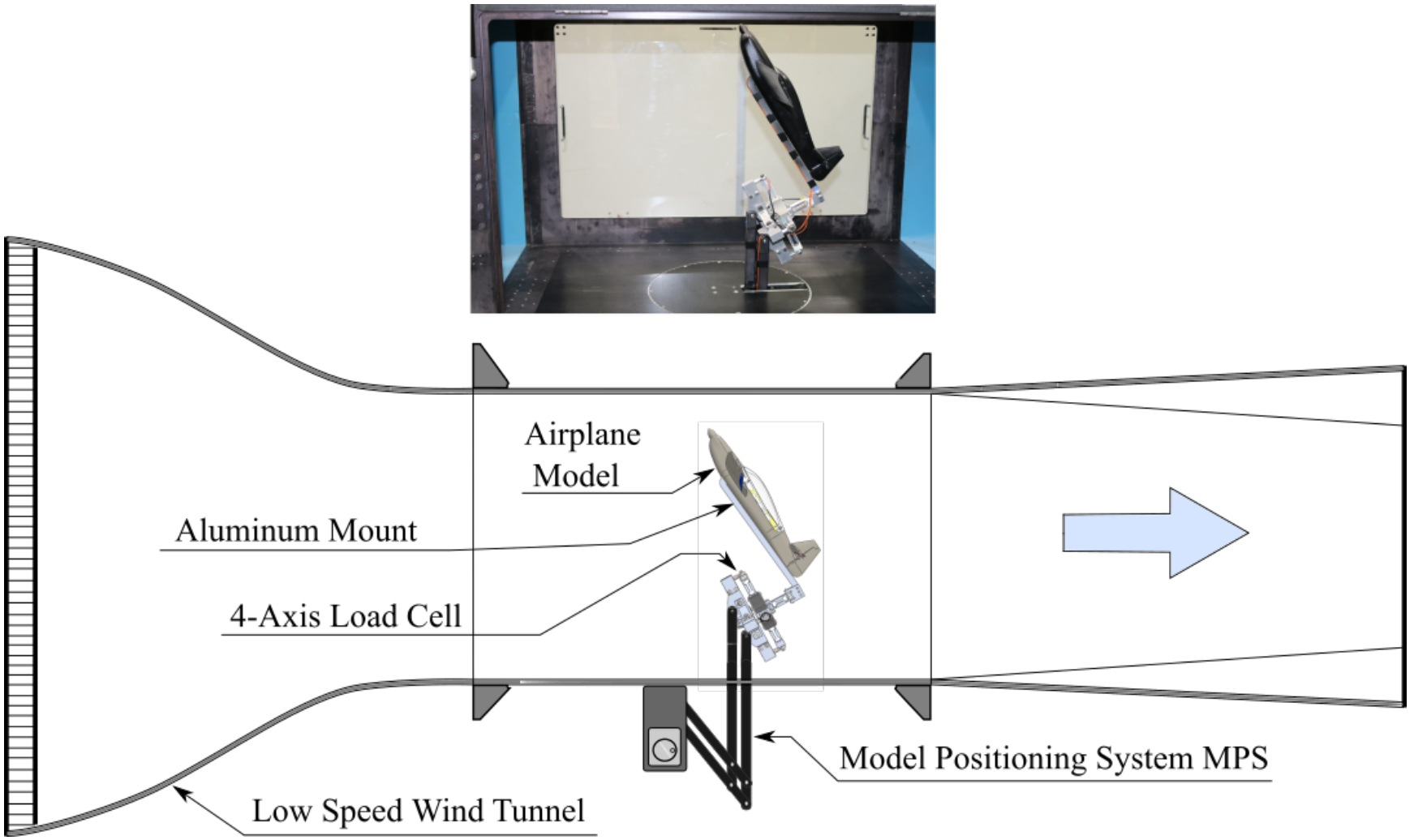

Figure 2.8: Schematic drawing and image of the first experimental setup.

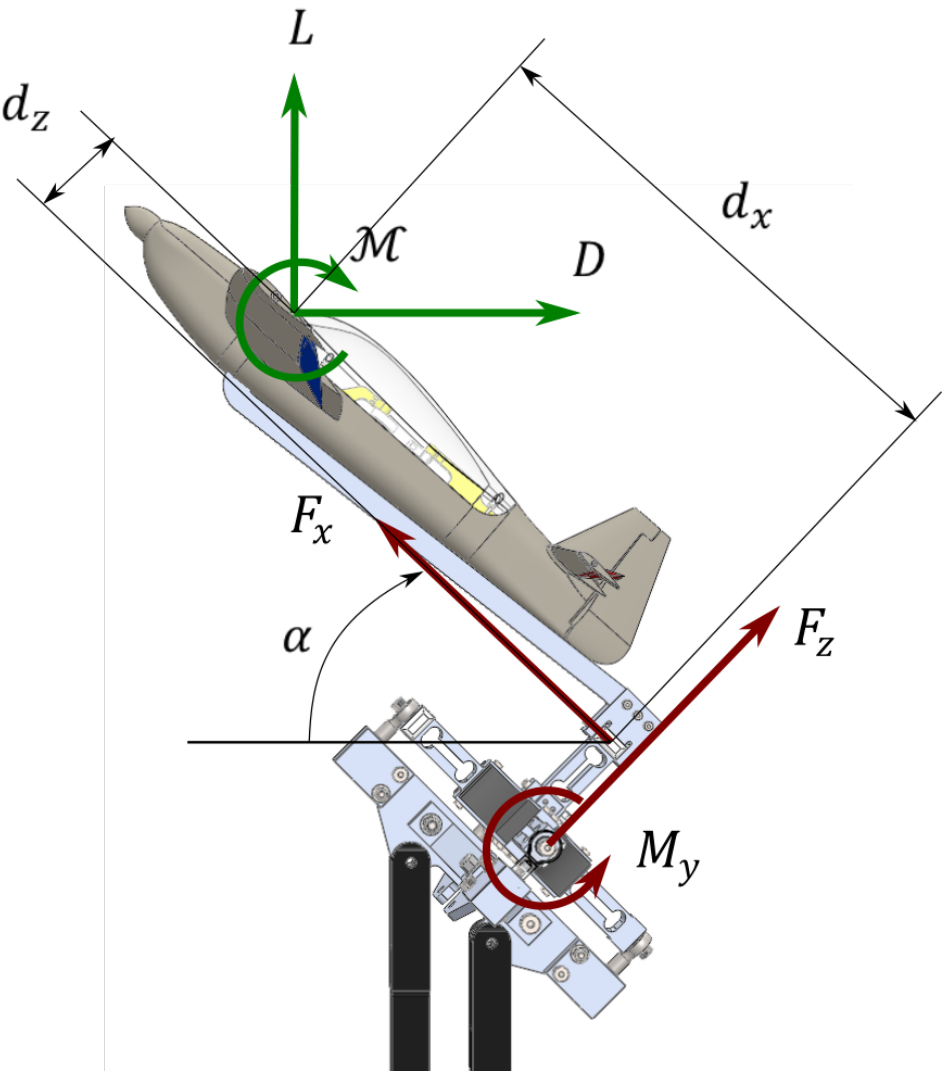

Figure 2.9: Forces' transformation diagram.

the wing root section. The axes of rotations of both ailerons are colinear; accordingly, it is perpendicular to the airplane's longitudinal axis.

2.1.7 Statistical Analysis

The mean and the standard deviation of the measured dataset are calculated online by the LabVIEW program. The standard error $\sigma_{\overline{n}}$ is calculated based on the length n and the standard deviation σ as follows:

$$\sigma_{\overline{x}} = \frac{\sigma}{\sqrt{n}} \tag{2.6}$$

Figure 2.10 shows the calculated standard error (in the form of error bars) in the four signals of the load balance F_x,F_z,M_x and M_y versus angle of attack at aileron deflection of 15°. This Figure concludes two outcomes: First, the error margin in F_x andM_x is greater than in F_z and M_y. The range of F_x is much less than the capacity of the load cell, while the combined error of this load cell is 0.3% of the Full Scale. As for M_x, in addition to the same reason of F_x error margin increase, the stiffness of the Model Positioning System (MPS) about the x-axis is not high in comparison to the y-axis. The low stiffness increases the structural response to M_x. Accordingly, it increases inertial loads, which increases the uncertainty in M_x. Second, the error margin increases after $\alpha = 10°$ because of the turbulent unsteady fluctuations associated with stall and post stall regimes, and the aerodynamic loads become non-stationary.

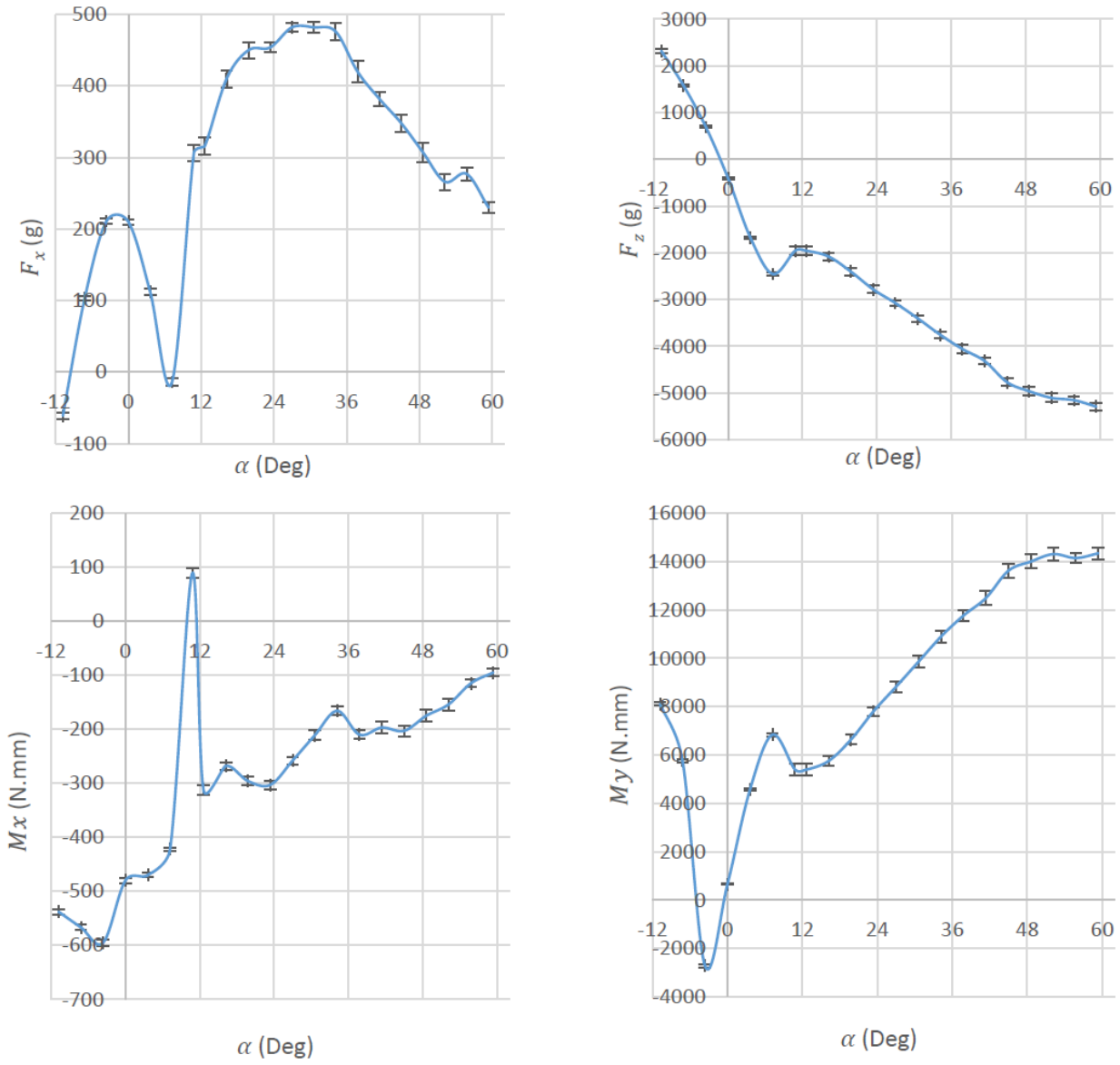

Figure 2.10: Statistical analysis in load balance reading.

2.1.8 Wind Tunnel Corrections

The wind tunnel correction for the total solid blockage and wake Blockage is calculated in equation based on the following suggestion of Barlow et al. [103] for the unusual shapes since the experimental setup in the wind tunnel section includes a complete airplane model

and multi-axis load balance:

$$\epsilon_{tot}(\alpha) = \frac{1}{4}\frac{\text{System Frontal Area}(\alpha)}{\text{Test Section Area}} \tag{2.7}$$

Where:

$$\text{system frontal area}(\alpha) = \text{airplane and LC frontal area}\cos(\alpha) + \text{planform area}\sin(\alpha) \tag{2.8}$$

The frontal area of the airplane, load cell, and position system struts, and the planform area of the airplane model are calculated numerically using the 3d model of the system.

To account for the solid blockage, streamline curvature and downwash, the Lift coefficient, the drag coefficient, and the angle of attack AOA are corrected according to the following equations.

$$\alpha = \alpha_u + \delta\frac{S}{C}C_{Lu} \tag{2.9}$$

$$C_L = C_{Lu}\left(1 - 2\epsilon_{tot}\left(\alpha\right)\right) \tag{2.10}$$

$$C_D = C_{Du}\left(1 - 2.3x\epsilon_{tot}\left(\alpha\right)\right) + \delta\frac{S}{C}{C_{Lu}}^2. \tag{2.11}$$

Where, δ is the boundary correction factor from figure 10.17 in [103], based on an effective span $b_e = 0.9b$ and wind tunnel aspect ratio=1. The effect of applying these wind tunnel corrections on the lift coefficient and drag coefficient for the experiment without deflecting the aileron and the elevator is shown in Fig. 2.11.

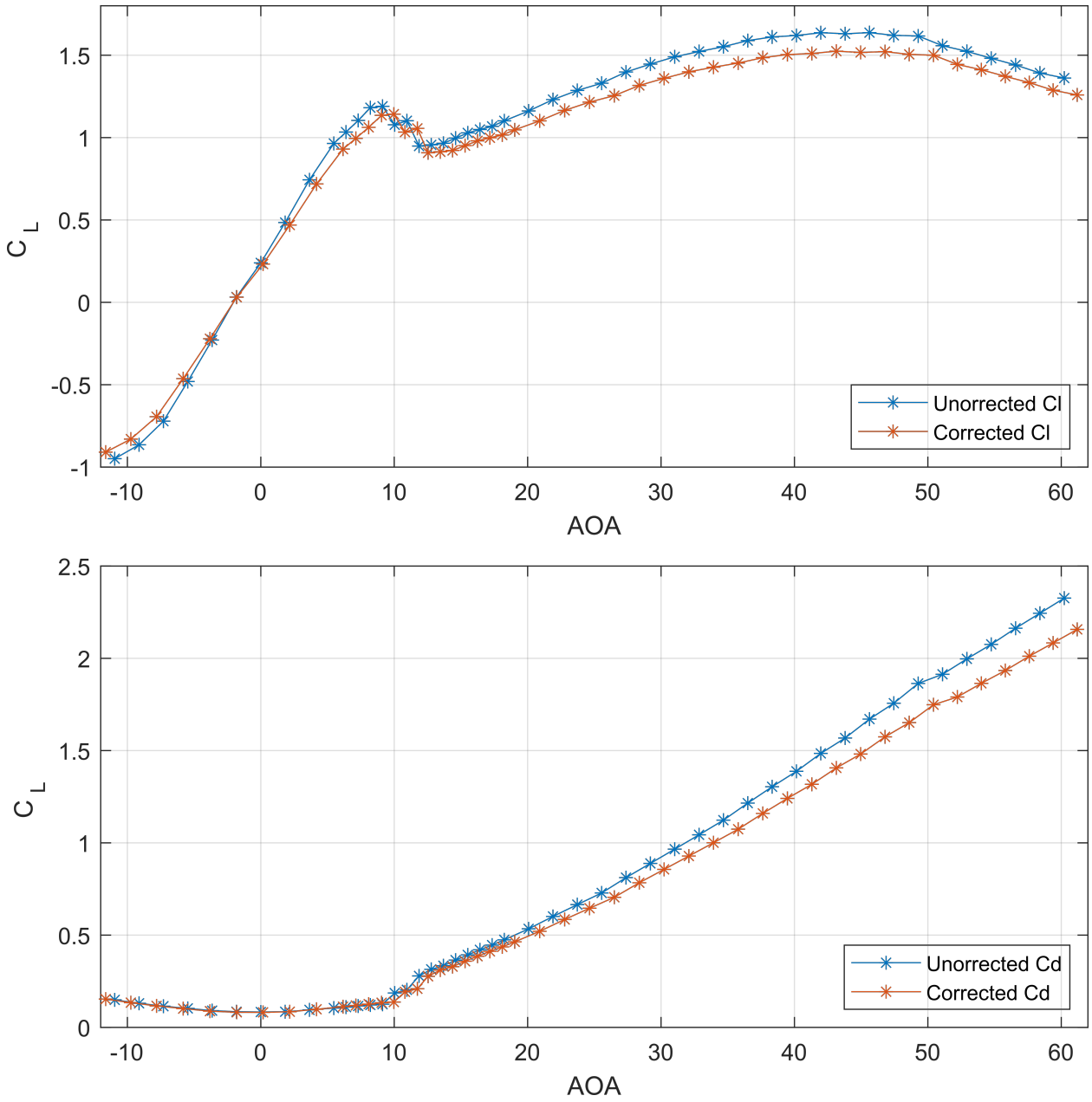

Figure 2.11: Wind tunnel corrections on C_L,C_D ,and AOA without deflecting the control surfaces of the rectangular wing airplane model.

2.1.9 Data Acquisition

The four-axis load balance was designed and fabricated to withstand the high aerodynamic loads associated with high angles of attack wind tunnel testing [104, 38, 27, 73, 105, 106, 107].

The bandwidth of this load cell was found experimentally at 60 Hz, while the sensitivity is 2 mV/V, and the resolution is 0.04 N. The load balance is powered by an AC Wheatstone bridge excitation power supply PSM-R. The Model PSM-R has a split bobbin transformer for high line isolation. In addition, it has remote sensing to eliminate line drop errors and features excellent regulation, stability, and very low noise [108].

Four Anti-aliasing, single-channel, and fully programable low pass filters (LPFs) of type USBPGF-S1 [109] are installed after the four-axis load cell. The cut-off frequency of the LPFs is the same as the bandwidth of the load cell. The signals of the load balance were acquired by National Instrument Data Acquisition (DAQ) device NI USB-6211 [110].

A data flow program was designed using LabVIEW to process the signals of the load balance. This LabVIEW program provides a real-time waveform and averaged values for the four global forces; F_x,F_z,M_x and M_y. Moreover, it monitors, saves, and alarms for overloading saves the maximum loadings, and performs dynamic and static calibration for the load balance. Figure 2.12 shows a wiring diagram for the load balance connections with the power supply, LPFs, DAQ, and the interface program.

2.1.10 Experiment Procedure

The experiment follows the following sequence:

1. Levelling the airplane at zero angle of attack, i.e., the wing chord line should be parallel to the wind tunnel test section floor, which is horizontal.

2. Move the control surfaces to the desired deflection using the micro-controller, which controls the two digital servomotors.

3. Taring the load balance from the LabVIEW dataflow program.

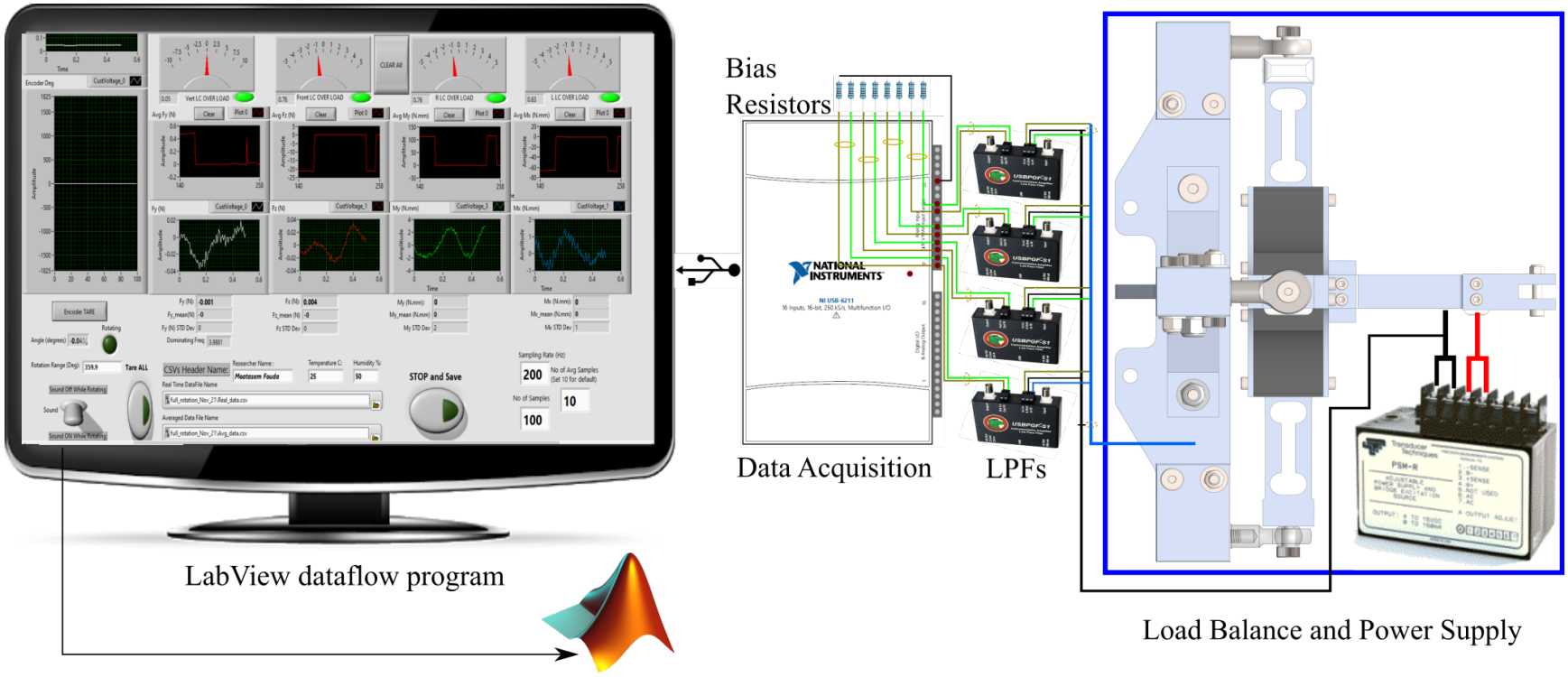

Figure 2.12: Wiring diagram for the load balance.

4. Running the wind tunnel at the desired speed and waiting until it becomes steady.

5. Decreasing the AOA by rotating the handle 3 turns in the counterclockwise direction, which corresponds to -10.95 Deg.

6. Increasing the AOA with the rate of 1/5 turn per step, which equals 1.825 deg/step, and recording the average measurements of the load balance and the wind tunnel speed in addition to the humidity and the temperature at the beginning of the experiment. During the stall range, which is from 6.38 deg to 20.08 Deg, the handle is rotated with a rate of 1/4 turn per step. The experiments continue until reaching AOA of 60.225 Deg.

7. The stall is monitored by tufts equi-spaced over the upper surface of the wing

2.2 Pitching and Rotating Wings Experimental Eetup

2.2.1 Wings

Three rectangular wings of chord 150mm and span of 300 mm were tested. These three wings are of the following sections:

1. NACA 0012

2. NACA 0015

3. NACA 0021

These wings are 3D printed of a PC-ABS plastic alloy, then post-processed and painted in black for future flow visualization. In addition to the steel rod, which attaches the wing

model to the stepper motor, these wings are also reinforced by two carbon fiber rods in a symmetric way relative to the center of mass in order not to affect the center of mass position. Furthermore, all wings are equipped with removable upper and lower end plates to study the effect of the end plate on the span-wise flow.

2.2.2 Vertical Testing configuration

The wing model is mounted vertically using a steel rod reinforcing the rectangular wing model at its center of mass position to reduce the lateral inertial loads associated with the high speed or accelerating rotational motion. Each wing's center of mass is calculated numerically. These centers of masses were found to be as follows:

1. NACA 0012:41.97% of the chord
2. NACA 0015:41.63% for the chord
3. NACA 0021:41.73% for the chord

The metallic rod penetrates the floor of the wind tunnel test section through a hole with a sufficient gap to avoid any reaction forces emerging from the contact with the wind tunnel body under the highest aerodynamic force. The metallic rod is rigidly coupled with the shaft of a high torque NEMA 23 stepper. This stepper motor is mounted on the top of a Four-axis load cell to measure the lateral Lift force, the vertical spanwise force, and the two horizontal moments Mx and My (Fig. 2.13).

2.2.3 Inertial loads filtration and data acquisition

In the first trials of this experiment, we found that the structural response of the experimental setup adds inertial loads to the aerodynamic loads, especially at angular speeds

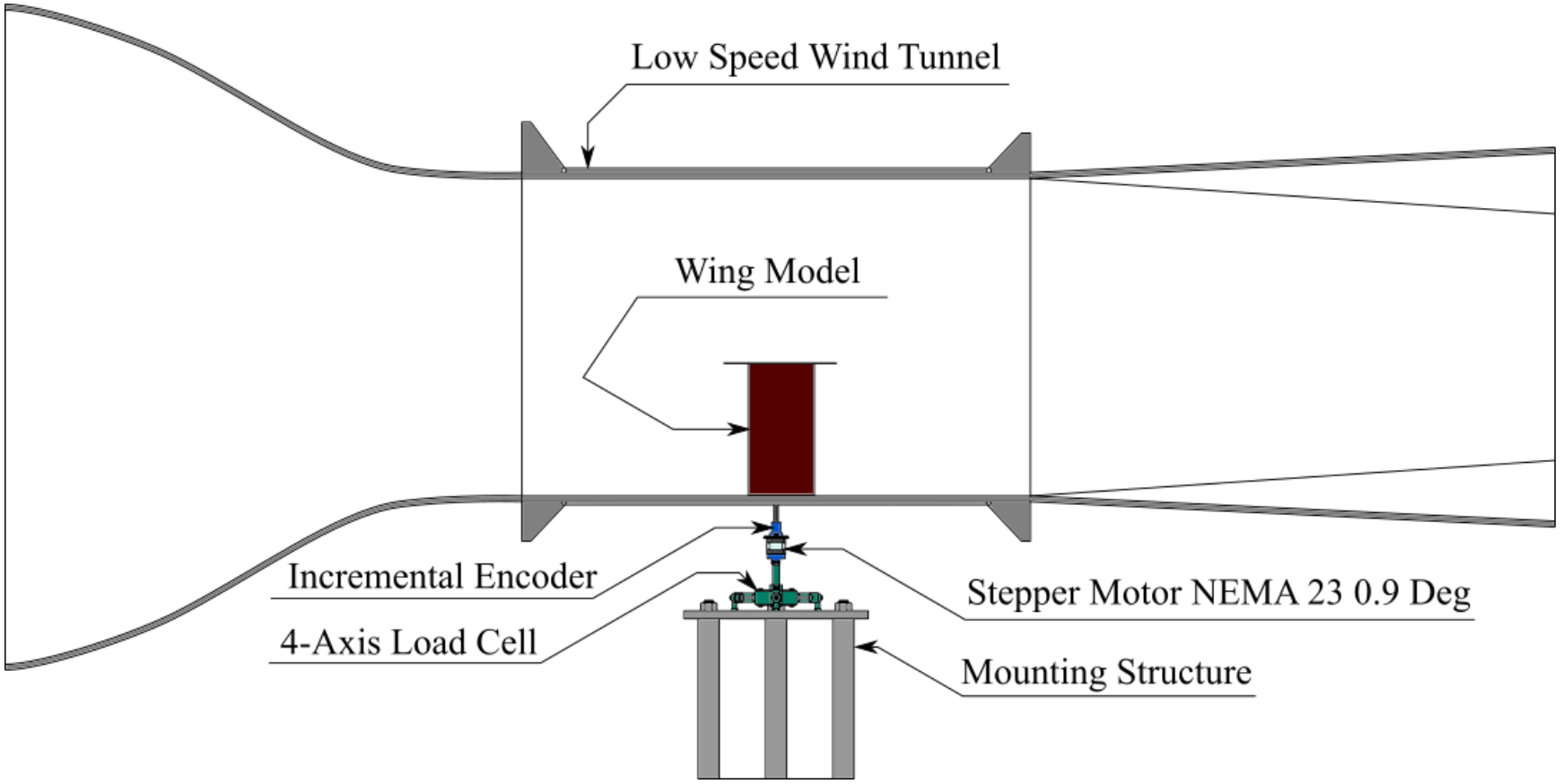

Figure 2.13: Wind tunnel vertical testing configuration.

$\omega > 10Deg/sec$. An anti-aliasing Butterworth analog low pass filter was used before the sampling to filter these high-frequency inertial loads from the low-frequency aerodynamic loads. The LPF cutoff frequency should be low enough to filter the natural frequency of the first mode. Impact hammer modal testing is used to measure the primary natural frequency of the wing-stepper motor-load balance system. The natural frequency of the NACA0012 was found at 11 Hz, while the natural frequency of the heaviest wing model, NACA0021, was found at 10 Hz (Fig. 2.14). The four low pass filters used in this experiment to filter the four signals of the load cell are of model USBPGF-S1 [109]. The maximum cutoff frequency to filter the primary structural response was found experimentally to be at 5Hz Fig. 2.15). The filtered signals are sampled at a rate of 200 Hz by the NI USB-6211 [110].

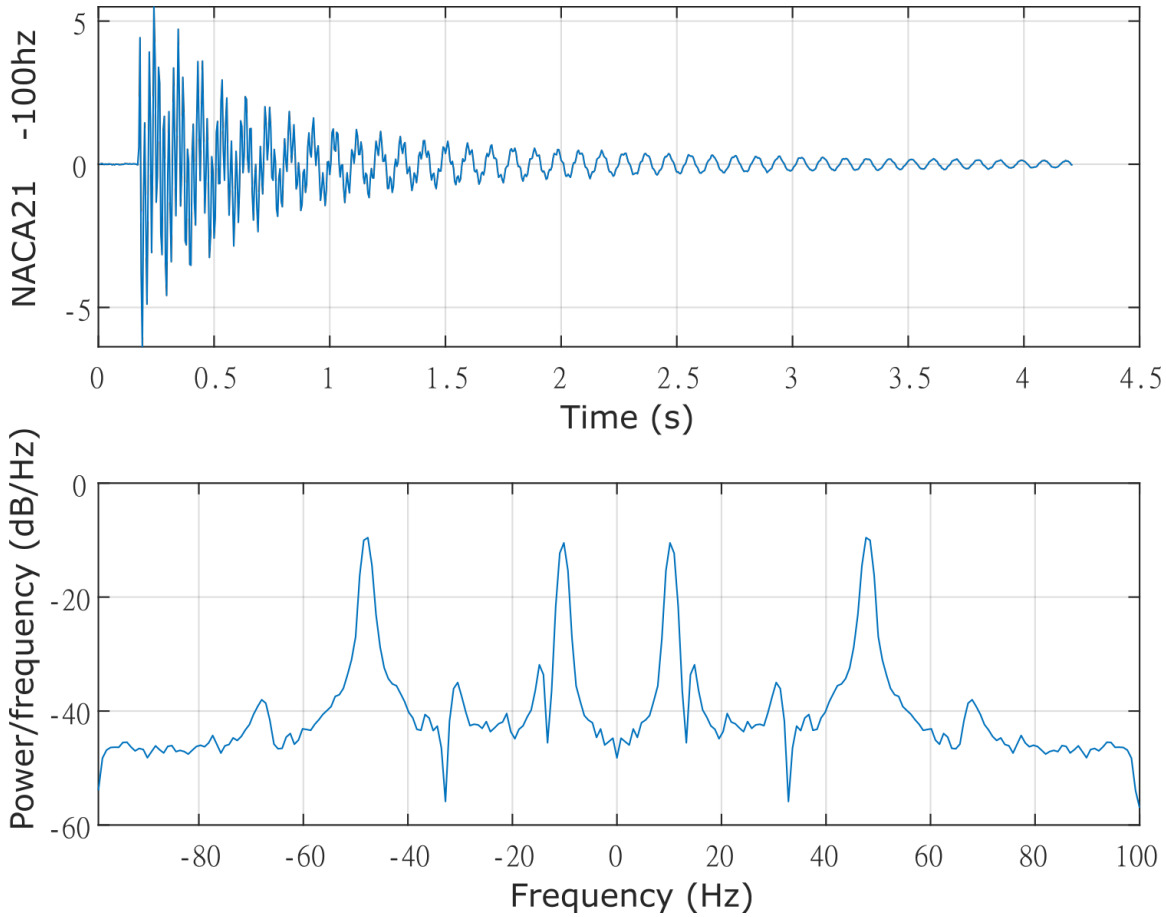

Figure 2.14: The response of the NACA 0021 experimental setup to a hammer test- filtered at 100Hz.

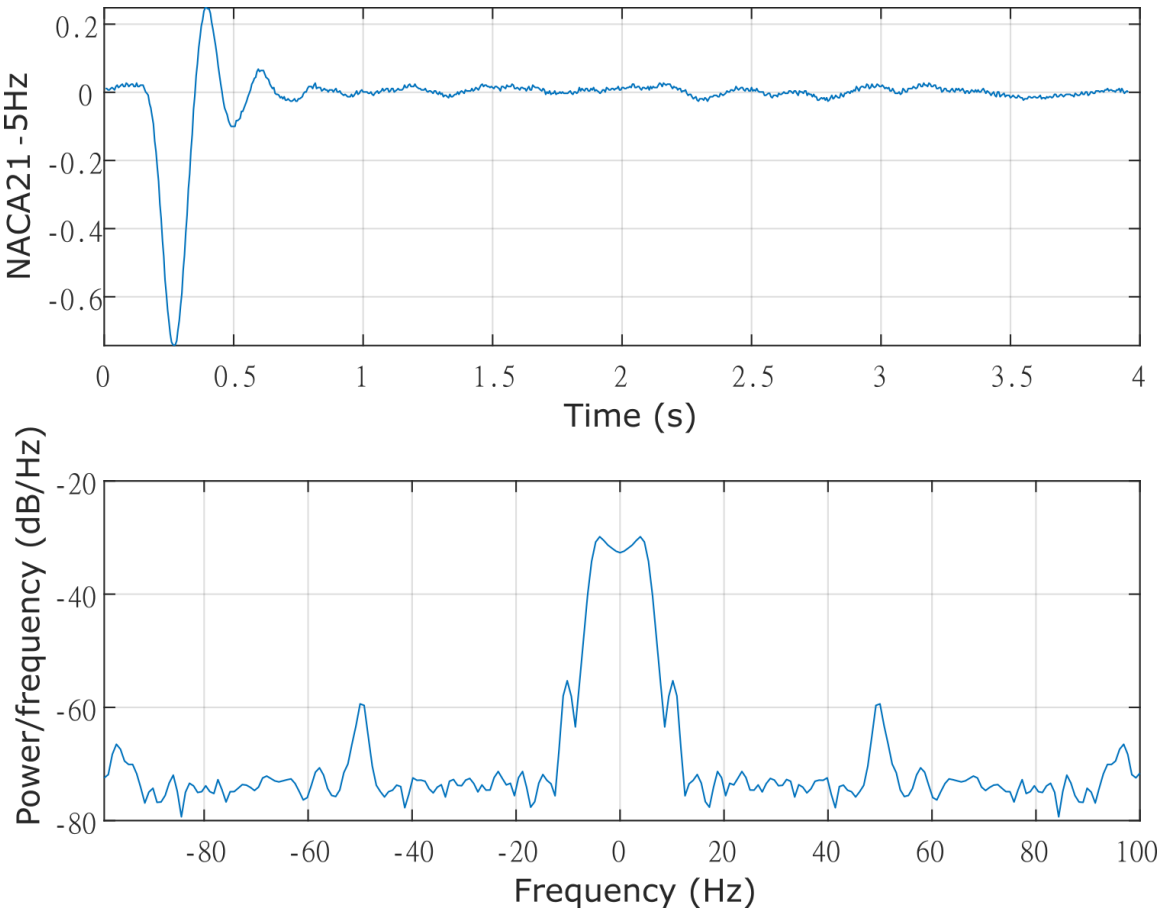

Figure 2.15: The response of the NACA 0021 experimental setup to a hammer test- filtered at 5Hz.

The step of the NEMA23 stepper motor is 0.9 Deg [111]. The stepper motor is driven by a DM542 digital micro-stepping stepper motor driver at 32,000 micro-stepping, making the final step 0.0056 degrees. The stepper motor was sized to provide a maximum torque higher than the required torque at the acceleration and deceleration of the heaviest wing, NACA 0021, at the highest Reynolds number. Although a motor with high output torque will not skip steps during the harshest rotation, the AOA is measured using another independent digital incremental encoder of type CUI AMT10 of resolution 2048 [112]. The digital encoder is mounted on the stepper motor and measures the motor shaft's angular position, while its digital signal is fed into the same DAQ used to sample the load cell signals. Because the analog signals of the load cell are filtered at a cutoff frequency of 5 Hz, while the digital signal of the encoder is not, there is a delay of about 0.12 seconds in the load cell readings

from the encoder readings. This delay will be found in all figures presented in this paper, and it is more evident in the high angular speed graphs. It is also found that the response of the aerodynamic forces becomes immediate if the LPF cutoff frequency becomes higher than 200 Hz.

The motion of the stepper motor is controlled by two Arduino codes designed for two modes of testing:

1. Static complete rotation testing; the code controls the motor motion to rotate 360 deg incrementally with adjustable parameters. For this experiment, the parameters are selected such that the wing rotates at a step of 1.8 deg, its incremental motion is at 30 deg/sec, and the wing stays at each step for 5 seconds to eliminate any steadiness in the flow due to the motion of the wing. At the last second of the five seconds, the aerodynamic forces are averaged for calculating the aerodynamic forces at this angular position.

2. Constant angular velocity complete rotation testing; the code controls the motor motion to rotate 360 deg continuously five times with adjustable parameters. For this experiment, the parameters are selected such that the wing rotates 360 degrees at angular velocities 5, 10, 20, 30, 45, 60, 90, 120, 180, and 360 degrees per second while the wing stays still between the five rotations for the larger of the 10 seconds or the half of the periodic time of the rational motion.

2.2.4 Data processing and frequency analysis

A data flow program was built using LabVIEW to process the load balance signals and the incremental encoder's digital signal. This LabVIEW program automatically exports real-time array for the four global forces; F_y , F_z , M_x and M_y of each experiment run separately.

A Matlab code then handles these arrays for generating the required figures and analyzing the signals using the Fast Fourier and the CZT transforms to identify the lift coefficient's frequency and the frequencies of the shed vortices as measured by the load balance. Moreover, the LabVIEW data flow program monitors, saves, and alarms for any overloading that may occur, saving the maximum loading values reached during the experiments. Figure 2.16 shows a wiring diagram for the load balance connections with the power supply, LPFs, DAQ, and the interface program.

2.2.5 Experimental Procedure and Data Processing

The experiment starts with taring the load balance from the LabVIEW data-flow program and then running the wind tunnel to the desired speed. Once the airspeed in the test section becomes steady, the stepper motor is given a signal according to the type and the speed of the run. When the experiment is finished, two CVS files are exported by the LabVIEW for the real-time and averaged data of the forces and the AOA and

2.3 Wind Tunnel Calibration and corrections

2.3.1 Wind Tunnel Test Section Calibration

The Wind Tunnel used in this experiment is a subsonic AEROLAB Eiffel Wind Tunnel (Fig. 2.8)[113]. Test Section dimensions are 30"x30"x47". The maximum Speed is 30 m/s with zero blockage in case of no model is mounted in the test section. The air velocity in the test section is measured by two static rings; the first ring is mounted downstream of the contraction section inlet, while the second one is mounted upstream of the test section.

The wind tunnel test section was calibrated using a pitot tube and digital manometer.

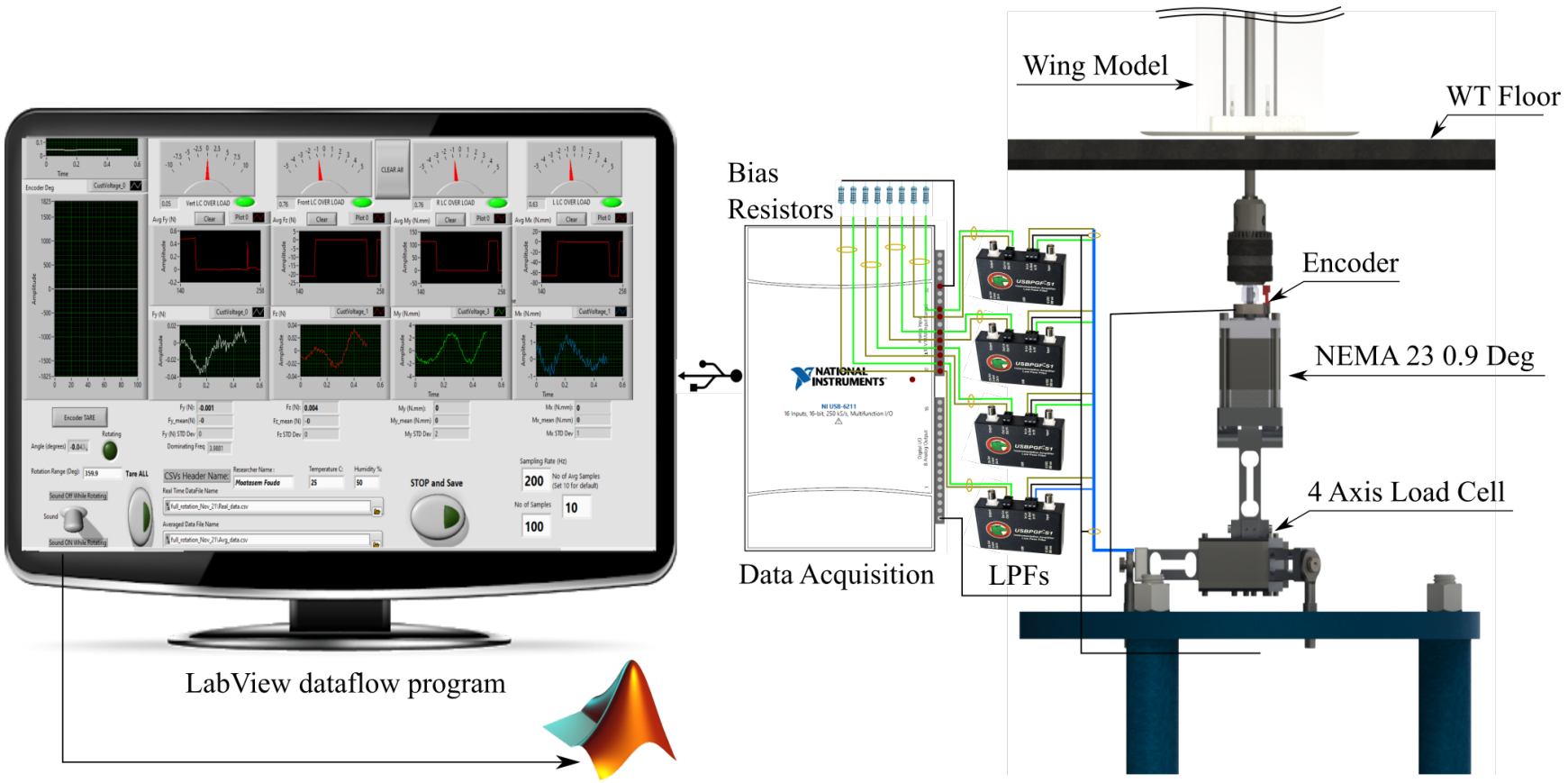

Figure 2.16: Wiring diagram for the vertical testing configuration.

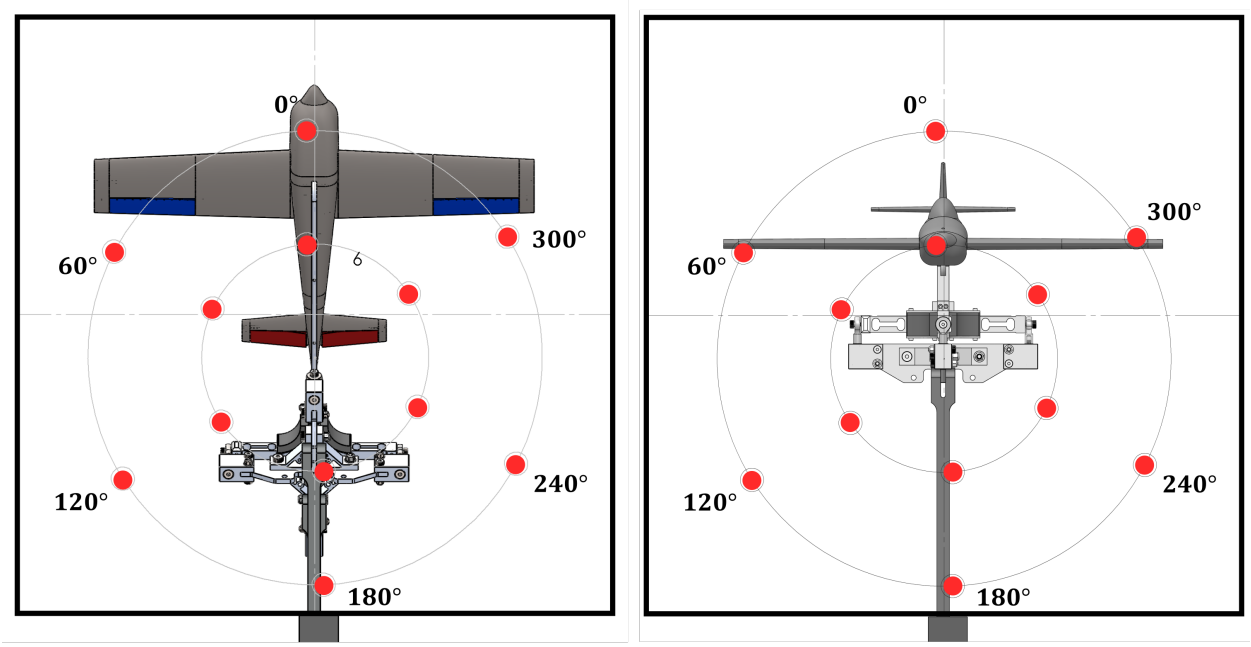

a) Airplane model at AOA = 60°

b) Airplane Model at AOA = 6°

Figure 2.17: Wind tunnel test section calibration points.

The pitot tube was mounted on a rotating mechanism designed to scan the test section. The airspeed is measured at twelve points; Six points at a radius of 290mm, and the other six points are 145mm. The gap between the points at each radius is 60 degrees (Fig. 2.17). The airspeed values measured by the pitot tube are the same at all points of the whole permissible range of the wind tunnel fan rotational speed except for the lowest point near the wind tunnel section floor. This slight decrease in the airspeed at this point may be caused by the boundary layer near the floor(Fig. 2.18-a). The airspeed values are consistent with the airspeed measured by the two static rings (Fig. 2.18-b). The airspeed values became scattered for the airspeeds less than 5m/s. This slight dispersion agrees with AEROLAB guidelines regarding airspeed instability for values less than 5 m/s.

This average airspeed measured by the two static rings is affected by the blockage caused by the airplane model, especially at high angles of attack. The wind tunnel is controlled by a manufacturer-made LabVIEW program equipped with a PID controller. The PID controller could be fed by either the rpm or the airspeed as measured by the two static rings. If the

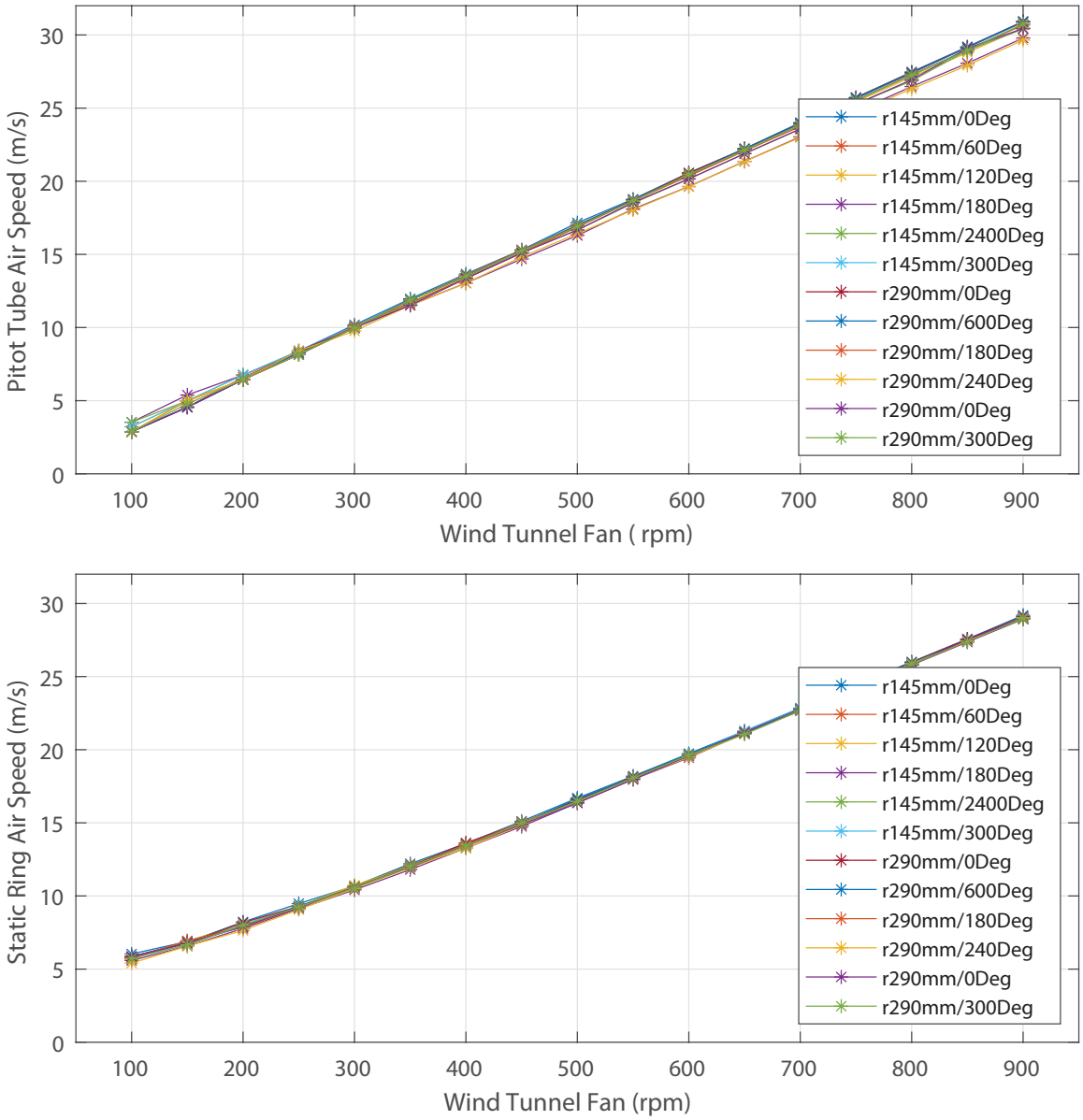

Figure 2.18: Wind tunnel test section calibration results.

PID controller is set to maintain the wind tunnel speed, it will increase the speed to keep the average speed measured by the two static rings and accommodate for the blockage. This compensation looks good for maintaining the average speed, but it will increase the airplane model's local speed. For this reason we used the fan rpm as the feedback parameter.

Chapter 3

Airplane Stability and Control Authority at Stall

In this chapter, the stability of the tapered wing airplane model is investigated by analyzing any disturbances in the four aerodynamic forces coefficients: Lift force coefficient C_L, Drag force coefficient C_D, rolling moment coefficient $C_{\mathcal{L}}$, and the pitching moment coefficient $C_{\Re}$ at the region of instability. C_{L_α} - α curve is generated by differentiating the C_L - α to determine the Region of instability, where the slope of the curve is negative or rippling around the zero value.

Based on the determination of the region of instability, the range of the angle of attack is classified into three regimes as follows:

1. Pre-stall regime AOA from 0° to 9°
2. Stall regime AOA from 9° to 12°
3. Post-stall regime AOA from 12° to 22°

3.1 A. Lift, Drag, and Resultant Aerodynamic Forces coefficient

3.1.1 Lift Force Coefficient

Figures 3.1 and 3.2 show a typical variation of the C_L with the angle of attack. It behaves linearly in the pre-stall regime with two different slopes, which is reminiscent of the NACA 0015 characteristics [114]. C_L experiences a maximum in the stall regime, followed by a drop (i.e., negative slope). It then experiences a second stall peak at $\alpha = 43°$ during the post-stall regime. Aileron deflection has a minor effect on lift force during this linear regime (Fig. 3.1). In contrast, the elevator deflection has a significant effect on lift (Fig. 3.2).

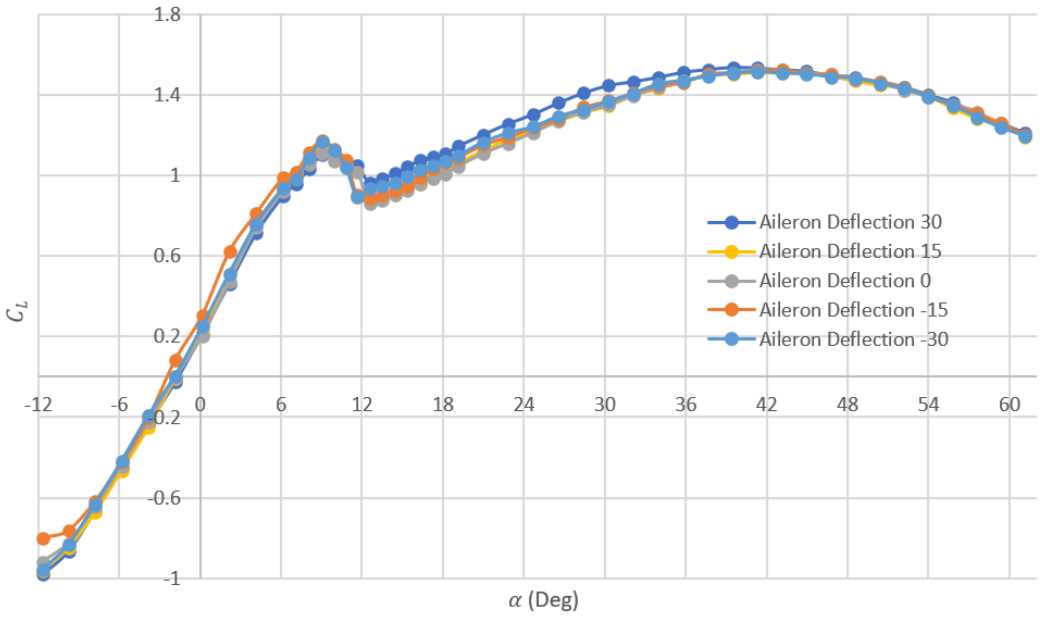

Figure 3.1: C_L vs AOA at different aileron deflections.

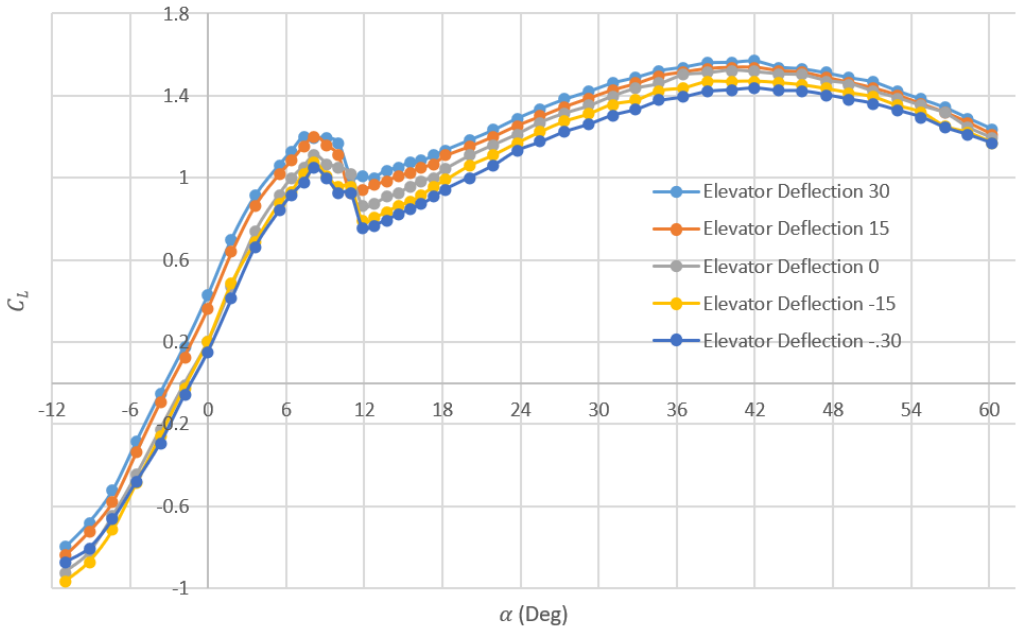

Figure 3.2: C_L vs AOA at different elevator deflections.

Figure 3.3 shows four curves of C_{L_α} for no control surface deflection, full aileron deflection, full positive elevator deflection and full negative elevator deflection. During the pre-stall regime C_{L_α} shows a plateau at a value of 0.11 to 0.13 deg^{-1} until AOA=6°, then it decreases to a value of 0.05 deg^{-1} at AOA=9°. During the stall regime, the sign of C_{L_α} is flipped to a negative sign. This regime of negative lift-curve-slope in stall is associated with reversal of most stability and control derivatives (e.g., negative roll damping), causing unconventional behaviors (e.g., wing drop) [37]. After the stall regime, C_{L_α} recovers its positive sign but at a lower value of 0.03, deg^{-1}; the wing (and consequently the airplane) loses more than two-thirds of its lifting capability/sensitivity. After the second stall peak during the post-stall regime, C_{L_α} decreases linearly starting at a value of 0.03 deg^{-1} at AOA=9° reaching -0.025 deg^{-1} at AOA=61°, crossing zero at AOA=43° (the location of the second stall peak).

Figure 3.3 shows as well that control surfaces have no effect on the lift-curve-slope C_{L_α} except in the instability region where aileron deflection that resists the wing drop seems to reduce the magnitude of the negative peak of the C_{L_α}.

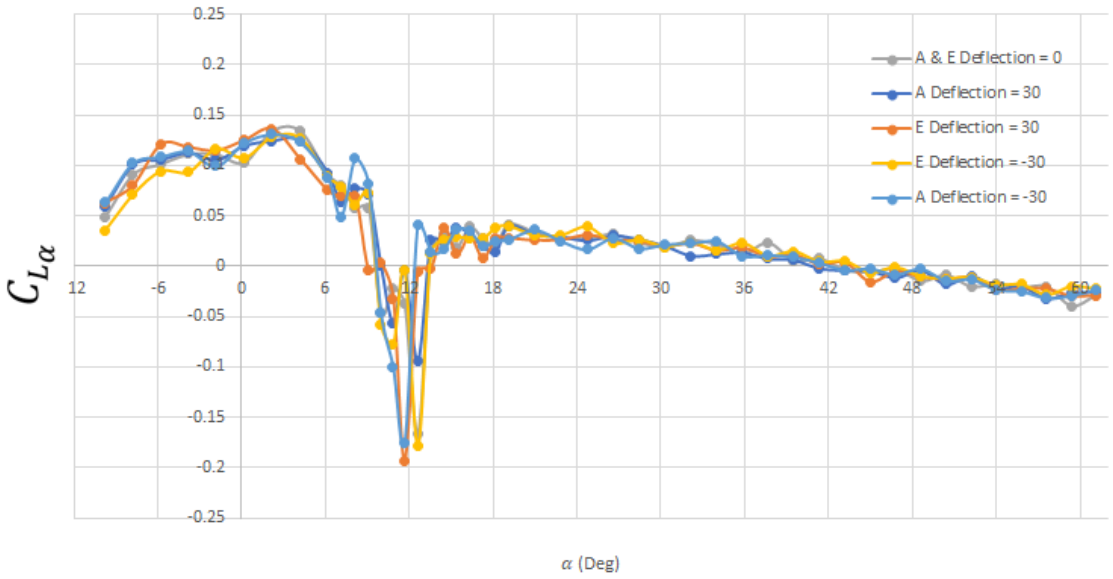

Figure 3.3: C_{L_α} vs AOA at different aileron and elevator deflections.

3.1.2 Drag Force Coefficient and Drag Polar

Figures 3.4 and 3.5 show the typical quadratic behavior of drag in the pre-stall regime. Before stall, with 1° AOA, C_{D_α} jumps from 0.005 deg^{-1} to 0.021 deg^{-1}.

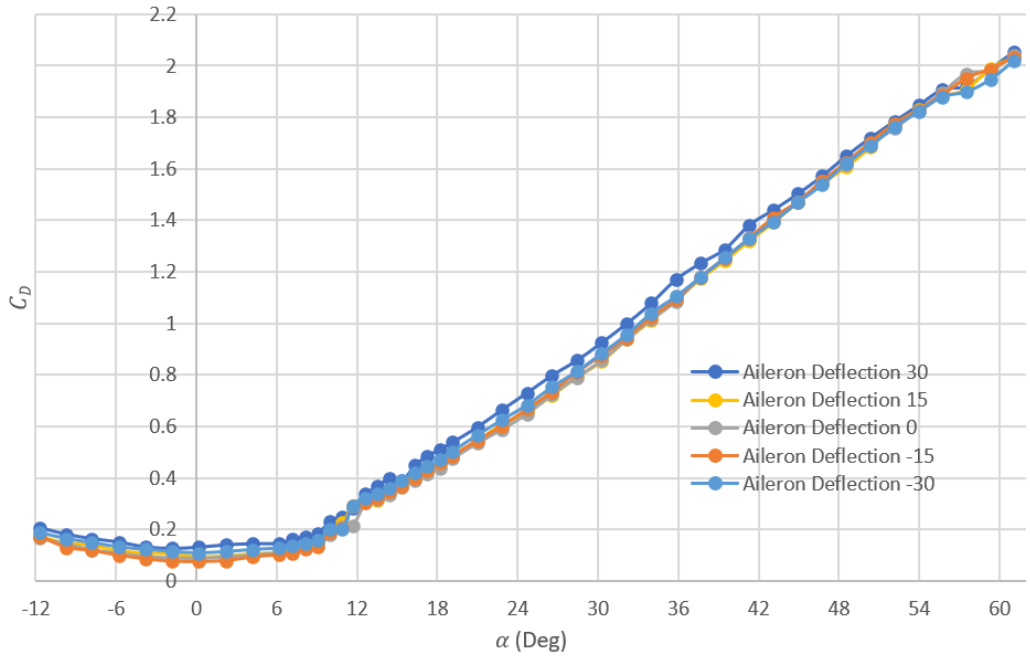

Figure 3.4: C_D vs AOA at different aileron deflections.

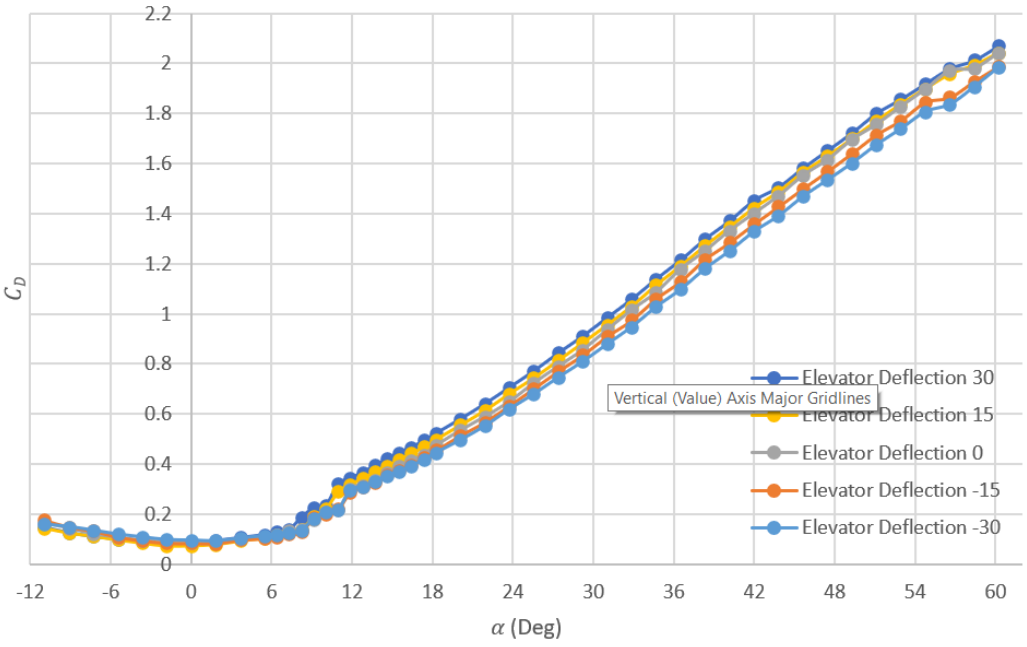

Figure 3.5: C_D vs AOA at different elevator deflections.

Figure 3.6 shows the minor effect of the aileron deflection δ_a on the drag during the pre-stall regime in the drag polar plot and shows no aileron effect during the post-stall regime.

On the contrary, the elevator deflection δ_e has no effect on the drag polar in the pre-stall regime, but it has a minor effect in the post-stall regime, as shown in Figure 3.7.

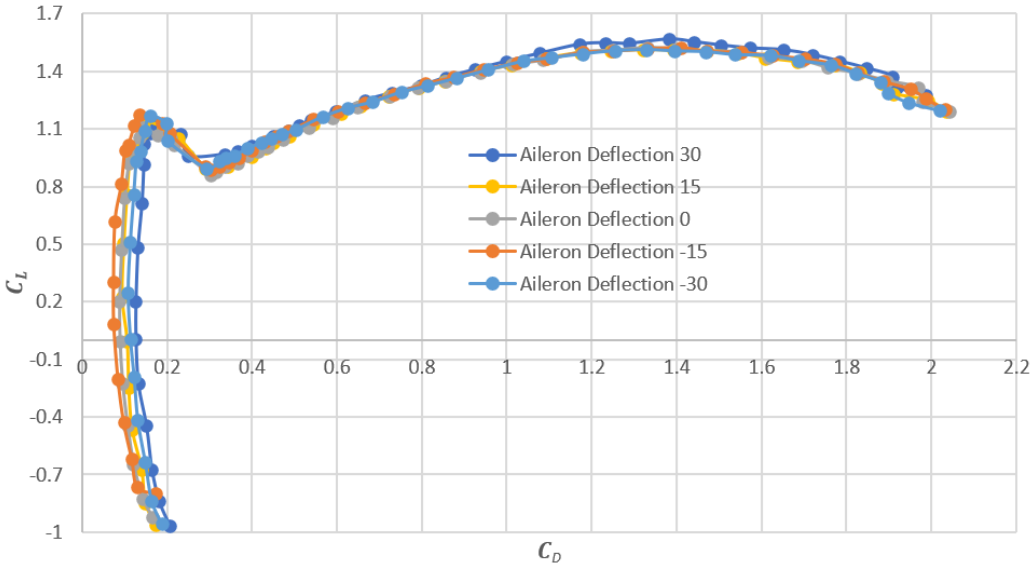

Figure 3.6: Drag Polar C_L vs C_D at different aileron deflections.

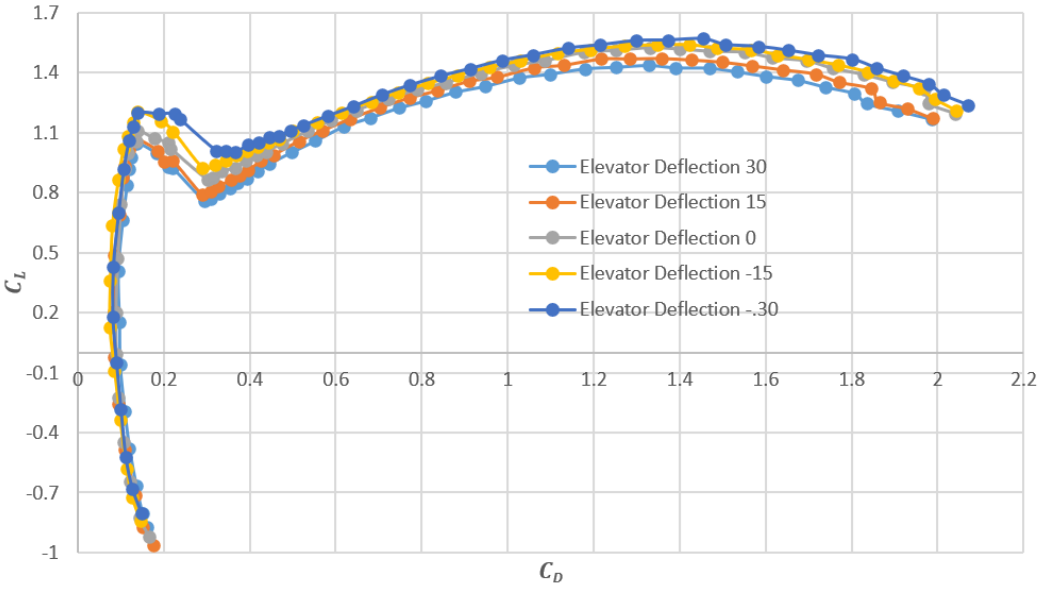

Figure 3.7: Drag Polar C_L vs C_D at different elevator deflections.

3.1.3 Total Aerodynamic Force Coefficient

The total aerodynamic force coefficient C_R gives a different perspective for wing performance since the drag force is relatively high with respect to the lift force in the post-stall regime. In the pre-stall and stall regimes, C_R behaves in a typical way to C_L as C_D profile is low compared to C_L. In this pre-stall regime, C_R is almost linear, changing the slope slightly after AOA=6° similar to the C_L slope change of NACA 0015. At stall, C_{R_α} becomes negative. In the post-stall regime, the total aerodynamic force increases at a rate almost half its increasing rate before stall, when C_{R_α} changes its sign at AOA=43°, C_{R_α} drops again to half and keeps decreasing until the end of the curve, but C_R keeps increasing until the end of the curve (Figures 3.1 and 3.2.

The aileron deflection δ_a has a minor effect on the C_R in the whole range of AOA, while positive elevator deflection δ_e shifts the curve up and the negative deflections do the opposite.

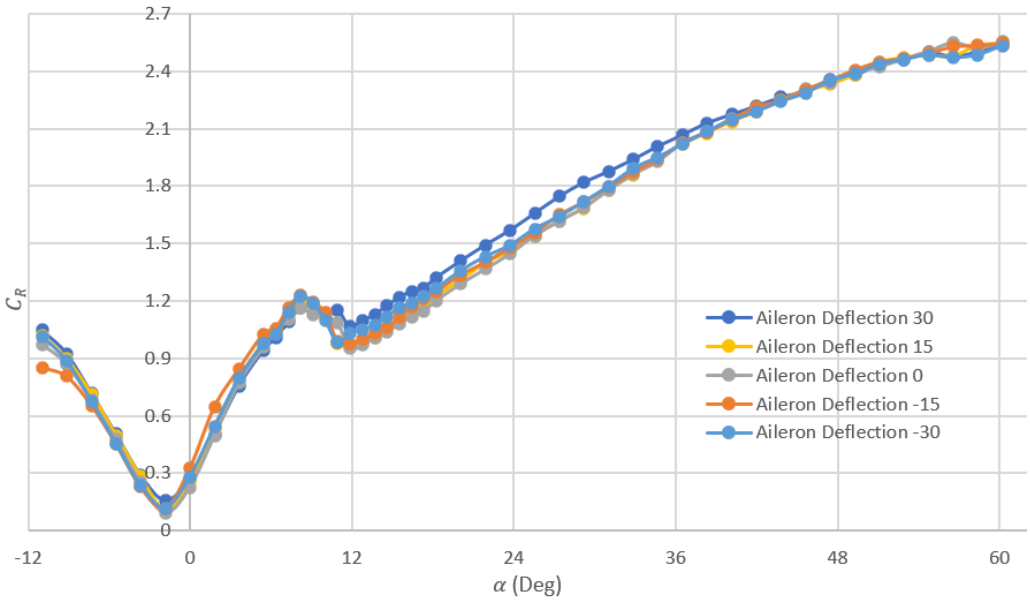

Figure 3.8: C_R vs AOA at different aileron deflections.

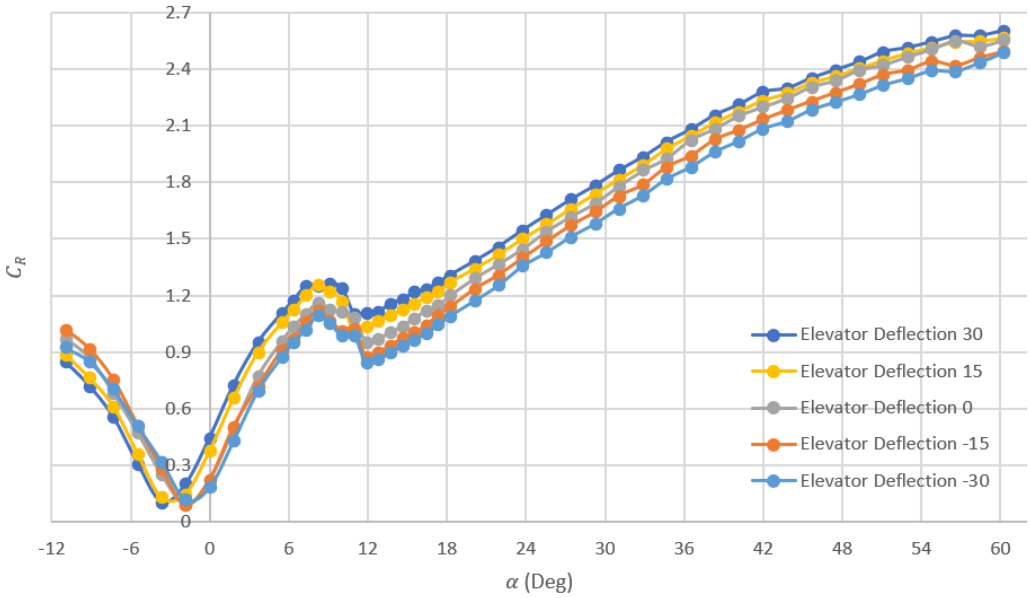

Figure 3.9: C_R vs AOA at different elevator deflections.

3.1.4 Variations of the Rolling Moment Coefficient $C_{\mathcal{L}}$ with AOA and aileron deflection δ_a

Figure 3.10 shows that there is an almost constant roll control authority during the pre-stall regime. The rolling moment does not change considerably with the angle of attack for the same aileron deflection, except for a slight decrease after AOA=6°. This means the aileron effectiveness is almost constant during this range. Figure 3.10 also shows that there is a significant rolling moment (similar to that described by Von Karman, Sears, and Schairer [40, 39, 41]) occurs at angles of attack (9° and 10°) for all aileron deflections; it is akin to the wing drop phenomenon [37]. The sign of this violent rolling moment is negative in most experiments irrespective of the sign of the aileron deflection; it adds a constant value of about -0.23 to the rolling moment coefficient for all aileron deflections. $C_{\mathcal{L}}$ does not recover immediately after increasing the AOA beyond this value until AOA=18°. Aileron effectiveness significantly deteriorates during this range. In fact,$C_{\mathcal{L}}$ is even reversed

at $\delta_a = 15°$ (Fig. 3.10). The aileron effectiveness recovers after AOA exceeds 18° until $C_{\mathcal{L}}$ reaches 60% of its effectiveness in pre-stall over the range $24°to28°$; this is the maximum value of $C_{\mathcal{L}}$ during the post-stall regime. After AOA =28°, $C_{\mathcal{L}}$ deteriorates again reaching about 50% of its effectiveness during the pre-stall regime at AOA =43°. From AOA =43° to 54°, another plateau occurs, then a significant deterioration happens until the end of the curve.

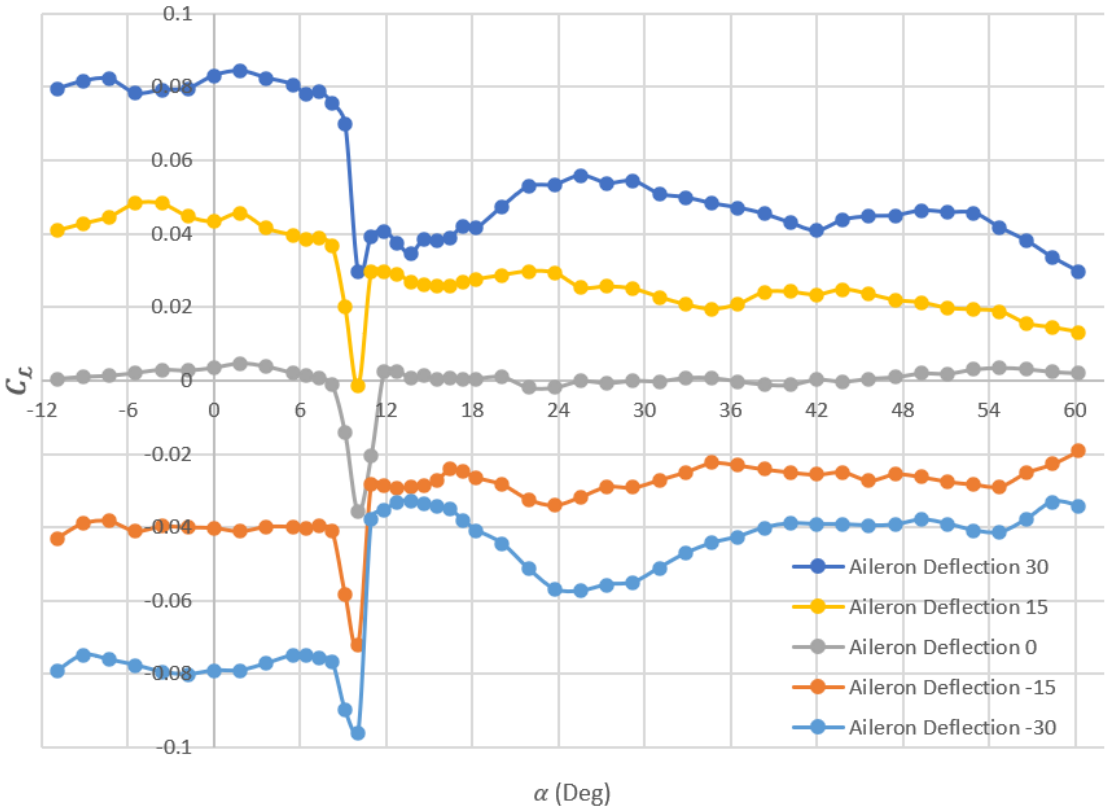

Figure 3.10: $C_{\mathcal{L}}$ vs AOA at different aileron deflections.

Figure 3.11 shows the rolling moment coefficient $C_{\mathcal{L}}$ vs aileron deflection δ_a at selected values of the AOA. This Figure provides insight into the aileron sensitivity during the wing drop phenomenon and during the post-stall regime. At zero AOA, the aileron sensitivity (measured in terms of the slope $C_{\mathcal{L}_{\delta_a}}$ of $C_{\mathcal{L}}$ curve with respect to δ_a in figure 3.11) is almost constant. During the pre-stall regime, $C_{\mathcal{L}_{\delta_a}}$ is almost linear (curves AOA =0°, AOA =3.7° and AOA =6.3° in Figure 3.11). At stall, (AOA =10°) $C_{\mathcal{L}}$ vs δ_a shows that in order to

overcome the moment created by the wing drop phenomenon, the aileron deflection should be higher than δ_a¿17°, noting that the ailerons of this model are slightly oversized with respect to the full-scale airplanes for the sake of this experiment. In the post-stall regime (from AOA =11° to 18°) $C_{\mathcal{L}}$ vs δ_a becomes nonlinear and the large δ_a deflection (i.e.δ_a¿15°) becomes ineffective . The two curves of AOA =18.3° and AOA =23.8° show the enhancement in $C_{\mathcal{L}_{\delta_a}}$ in the range of AOA from 18° to 28°, where the $C_{\mathcal{L}} - \delta_a$ curve changes from being nonlinear to almost linear again. Ailerons are effective in the range of AOA from 18° to 28°, but the value of $C_{\mathcal{L}}$ at any aileron deflection is almost 60% of its value in the pre-stale range. In order to investigate the rolling moment enhancement in the post-stall regime (AOA from 18° to 28°), we needed to calculate the aileron sensitivity $C_{\mathcal{L}_{\delta_a}}$ normalized by the lift curve slope C_{L_α} (Fig. 3.12). This normalized $C_{\mathcal{L}_{\delta_a}}$ is calculated by fitting the $C_{\mathcal{L}} - \delta_a$ curve with 1$^{\text{st}}$ order polynomial for the pre-stall and stall curves and fitting the post-stall curves with 3$^{\text{rd}}$ order polynomial. This curve should be considered carefully because of the low resolution of the aileron deflection data points. The two curves of AOA =18.3° and AOA =23.8° in Fig. 21 show that the normalized aileron sensitivity deteriorates with increasing aileron deflection. This means that there is another source for the rolling moment in addition to the common differential lift contribution. This source is believed to be the differential drag. At high angles of attack, the downward-deflected aileron creates more drag than the upward-deflected aileron, leading to a differential drag. Due to the high angle of attack, a significant component of this differential drag will luckily contribute to the rolling moment in the desired direction.

3.1.5 Wing Drop Direction Dilemma

It is widely spread that a wing drop near stall occurs either because the downward-deflected aileron increases the geometric angle of attack of its wing portion, hence stalling the wing of the downward-deflected aileron before the other wing. This differential stall creates dif-

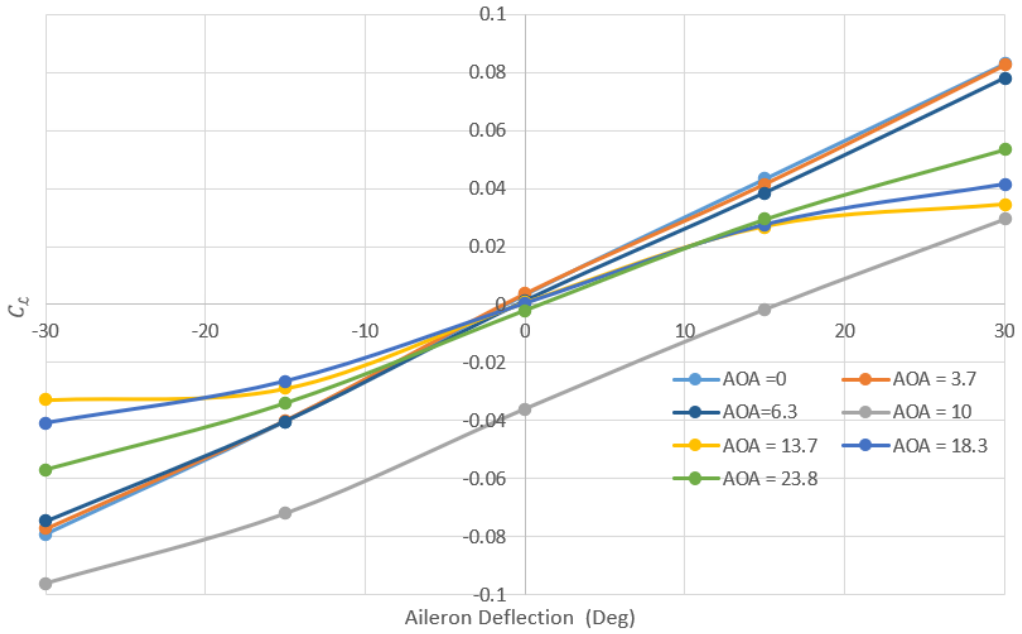

Figure 3.11: $C_{\mathcal{L}}$ vs aileron deflection at selected AOA values.

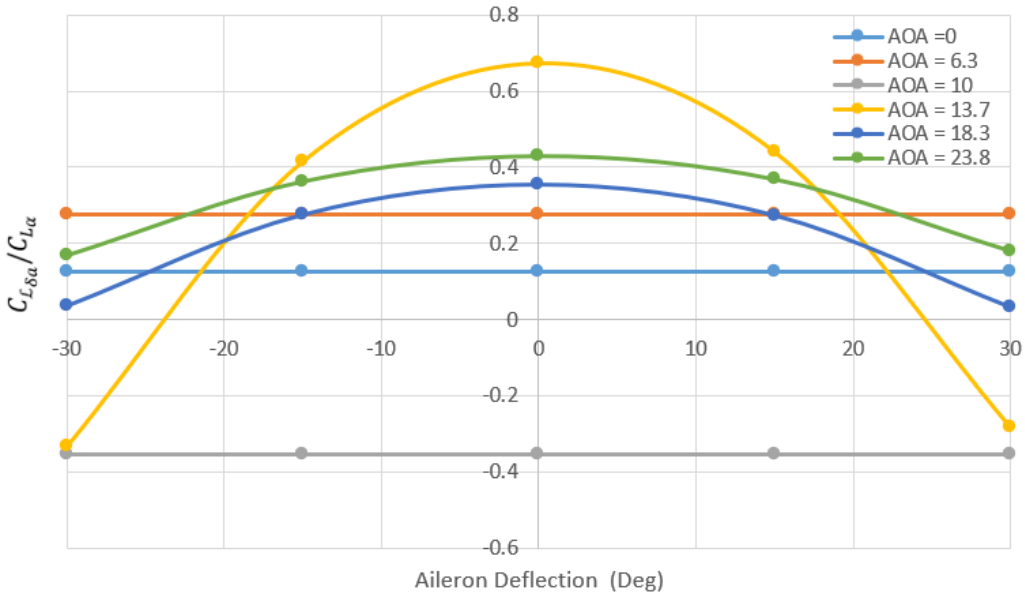

Figure 3.12: $C_{\mathcal{L}_{\delta_a}}/C_{L_\alpha}$ vs vs aileron deflection at selected AOA values.

ferential lift, which is the source of the wing drop rolling moment. According to this understanding, the wing drop rolling moment should typically be in the opposite direction of the rolling moment created by the ailerons (i.e., manifested by a decrease in aileron effectiveness). However, the experimental results presented in the previous sections refute this

hypothesis. The wing drop rolling moment is in the same direction with the same magnitude in most experimental trials; about 95% of the experiments, regardless of the direction of the aileron deflection. In the remaining 5%, it happens in the opposite direction but with the same magnitude, and the direction of the aileron deflection does not affect the wing drop direction too. For example, the wing drop kink in the $C_{\mathcal{L}}$ curve of one of our experiments (presented in Fig. 3.10 is in the same direction regardless of the ailerons deflection.

After this phase of research, and after reviewing the literature presented in chapter 1, especially the work of Von Karman and his students, we become more confident that the wing drop typically occurs at the stall without the need for any other asymmetric catalytic maneuvers/control such as aileron deflection and/or rudder deflection, side slip, side wind, dirty wing, etc. The dilemma that we faced after this phase was why the wing drop direction could not be predicted in this experiment. We expected that the tapered wing planform of this airplane model stalls first at the inboard wing; that's why the aileron deflection at the outboard wing does not initiate the stall, and then the wing drop. To prove this hypothesis, we decided to build four more airplane models with different wing planforms with different taper ratios. In the following chapter, the results of this work are presented.

Chapter 4

Effect of Wing Planform on Airplane Stability and Control Authority in Stall

In this chapter, the effect of wing planform on the stall progression, the wing drop phenomenon, and the roll control authority during stall is experimentally assessed. Five airplane models with different wing planforms are specifically designed for wind tunnel testing at high angles of attack. The aileron and the elevator of the five airplane models are controllable within a range from $-30°$ to $+30°$. Lift, drag, rolling moment, and pitching moment coefficients are measured at a range of angles of attack from -9 to +62 degrees at different control surfaces deflections.

4.1 Effect of wing planform on aerodynamic force coefficients

Fig. 4.1 shows that the wing planform has little effect on the C_L, C_D, C_L/C_D and C_R when the wings have the same span (no) twist, and similar aspect ratios. This behavior is expected in the linear regime. It is interesting to find such a similarity in the nonlinear (stall and post-stall) regime too. The pitching moment coefficient $C_{\mathcal{M}}$ of the hybrid wing is steeper than in the other wings in the whole range of the AOA.

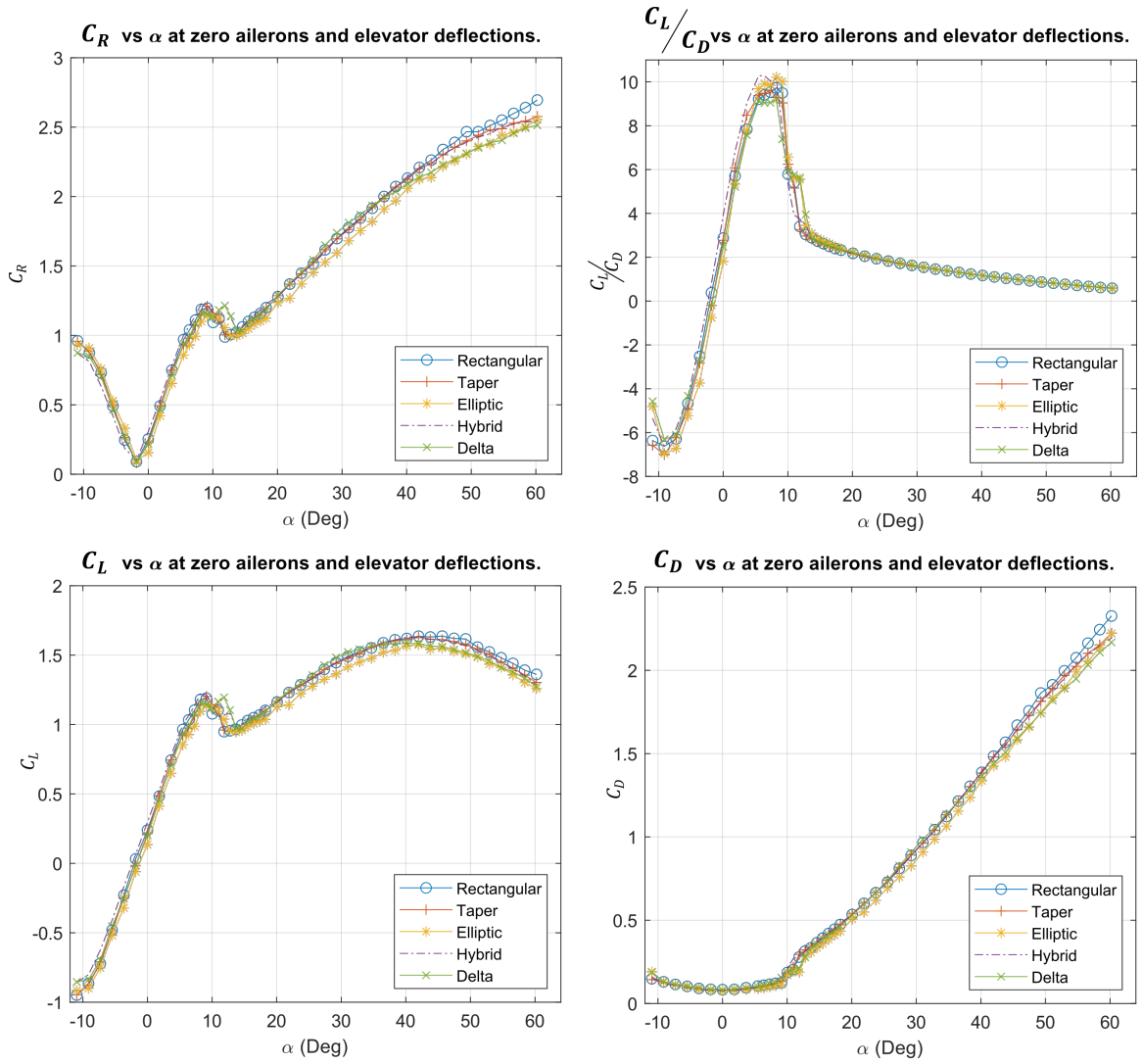

Figure 4.1: Effect of wing planform on aerodynamic coefficients and control derivatives.

Fig. 4.2 shows that the elliptical wing planform provides higher efficiency at the stall angle. This advantage should not be appreciated alone without considering the poor rolling control authority at the same angle of attack, which will be discussed in the following section. The same figure shows that the hybrid wing planform has a higher wing efficiency than the other wings at the stall angle.

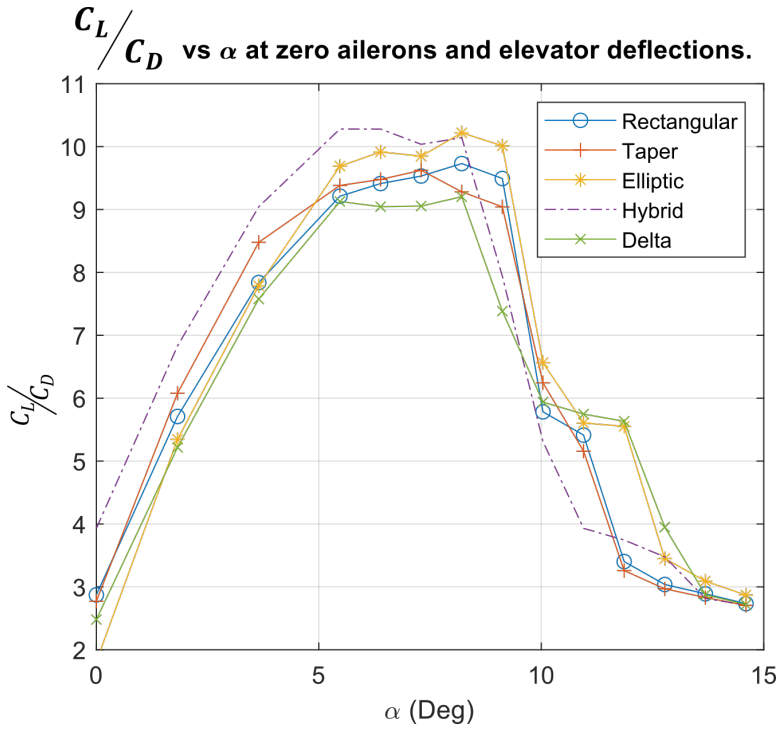

Figure 4.2: Effect of wing planform on the wing efficiency during the stall

4.2 Effect of wing planform on the rolling moment characteristics

Figure 4.3 shows the variation of the rolling moment coefficient over the five airplane models with the angle of attack at different aileron deflections. The figure shows that the rectangular and slightly tapered wing planforms provide higher aileron effectiveness in the linear regime at large aileron deflections $\delta_a \geq 20°$. This interpretation is based on the large spacing found

between the rolling moment coefficient $C_{\mathcal{L}}$ graphs corresponding to $\delta_a = 20°$, $\delta_a = 30°$. This spacing decreases in the elliptical, delta, and hybrid wing planforms.

A flow visualization using tufts showed that the stall starts at the same AOA on the upper surface of both wings in all planforms (Fig. 4.4). After increasing the AOA slightly, the stall propagates only on one wing, leaving the other wing unstalled. This asymmetrical stall pattern creates a huge rolling moment known as the wing drop. This rolling moment which is caused by the asymmetric lift distribution, was expected by Von Karman and studied by Sears, and Schairer [40, 39, 41]. Scharier concluded that the asymmetrical lift distribution could occur only in a minimal range of angles of attack after the stalling angle of attack. [41]. We think of the stability characteristics of the symmetric lift distribution at high angles of attack as saddle point stability, where any slight deviation in the initial and boundary conditions could destabilize the lift distribution from the symmetric configuration and makes it diverge to the other equilibrium: the asymmetric distribution. With the pendulum analogy, we can consider that the symmetric lift distribution at the small angles of attack is like the lower equilibrium point of a pendulum. When the angle of attack becomes large, the symmetric lift distribution becomes like the upper equilibrium point of the pendulum. This upper equilibrium point of the pendulum could be maintained if the "right" initial conditions are given in the lack of (unavoidable) perturbations. As in the real world, the pendulum cannot remain at the upper equilibrium point; the lift distribution cannot stay symmetric during stall.

The wing planform determines the direction of the wing drop since it determines where the stall starts (Fig. 4.4). The stall is found to start at the inboard wing sections of the rectangular and slightly tapered wing planforms near to the trailing edges [115], repeating the exact behavior of our previous wind tunnel experiment [38]. The inboard wing sections stall first because these sections operate at higher local angles of attack; i.e., they enjoy higher aerodynamic loading than the outboard wing sections. Even increasing the local

Reynolds number of these inboard sections somewhat with respect to the outboard sections like in the slightly-tapered planform does not change the location where the stall starts. The ailerons are still effective since it is not stalled yet. This finding is in line with the conclusion of Dulin and Takahashi, where they described the stall behavior of airplane at this moment as "mushy" [115].

Unlike the rectangular and the slightly-tapered planforms, the significant spanwise variation of the local Reynolds numbers of the delta and hybrid wing planforms changes the stall onset location and makes the outboard sections stall first (Fig. 4.4). Since the stall occurs first at the outboard wing sections, where the ailerons are located, the direction of the wing drop of these wings is dictated by the change in the local angle of attack, which depends on the deflection of the ailerons. For example, suppose the ailerons are commanded to create a negative rolling moment to the left during the stall. In that case, the right-wing will stall first because the right aileron is deflected downward, increasing the local AOA of the outboard sections of the right-wing. So, the wing drop will happen in the opposite direction of the commanded roll.

It has been noticed from the tufts flow visualization and the load balance measurements that the wing drop kink happens twice for the high taper ratio wings, i.e., delta and hybrid planforms, when there is no ailerons deflection. First, the outboard section of one wing stalls creating the first drop, then the outboard section of the other wing follows after a slight increase in the AOA recovering from this drop. After a second AOA increase, the inboard section of the first stalled wing stalls, too, creating a second wing drop and more significant than the first one. After the third AOA, increase the inboard sections of the second stalled wing stalls and recover the balance by having two entirely stalling wings

As stated earlier, the stall starts at the inboard wing sections of the rectangular and the slightly tapered wing planforms, away from the ailerons' location. Therefore the stall onset location is not affected by the change in the local angle of attack caused by deflected ailerons.

Unlike the delta and hybrid wing planforms, the direction of wing drop of the rectangular and slightly-tapered planforms is not dictated by the ailerons' deflection. In the majority of the wind tunnel experiments done on the rectangular and tapered wings under this research, the wing of the two airplane models dropped to the left as shown in their graphs in Fig. 4.3, but in very few tests, the airplane rolled to the right.

The stall starts at the inboard sections of the elliptical wing but away from the fuselage and close to the ailerons (Fig. 4.4). The stall propagates over the elliptical wing quickly, unlike the other wings. This quick stall progression is concluded by the sharp kink in the rolling moment coefficient of this wing (Fig. 4.3). The same result was found by Dulin and Takahashi [115]. The wing drop of this cropped elliptical wing of taper ratio $\lambda = 0.39$ is not dictated by the ailerons' deflection, in contrast to the rectangular and slightly tapered wings. Further investigation is required to assess the effect of aileron deflection on the wing drop direction of the elliptical wing planforms with zero taper ratio such as that on the Spitfire

The rolling control authority of the rectangular and the tapered wing planforms during the wing drop is still non-zero. This non-zero value is because one wing is fully stalled while the other is not stalled yet, and its aileron is still effective. It seems it may be able to save the airplane from spin, but this will require a quick response like in this YouTube Video [116]. However, for the hybrid and delta wings, the maximum achievable rolling moment around the wing drop moment is almost zero, implying a serious LOC. This is in line with Schairer's conclusion regarding the magnitude of the wing drop moment: the unsymmetrical lift distribution produces a rolling moment of the same order of magnitude as that caused by a fully deflected ailerons [41].

The rolling moment coefficient of all wing planforms deteriorates after the recovery from the wing drop. $C_{\mathcal{L}}$ value becomes about 0.05 after the stall for $\delta_a = 30°$. This value represents about 62% of its pre-stall characteristics for the rectangular and the slightly tapered wing, but it represents about 80% of the pre-stall value for the tapered and rectangular wings.

4.3 Effect of wing planform on the pitching moment characteristics

In all wing planforms, the positive elevator deflection shifts the pitching moment coefficient curve down, while the negative deflection shifts it up (Fig. 4.5). During the horizontal tail stall and the following wing stall, the pitching moment coefficient increases with the increase in AOA in the range of AOA from 9° to 12°. This behavior will affect pitching stability dramatically. It will be required from the elevator to double the effort to provide a negative pitching moment sufficient to overcome the positive pitching moment that comes from stalling the tail and the wing in order to nose down the airplane and take the airplane back to the pre-stall regime.

The steep $C_{\mathcal{M}}$ of the hybrid wing planform has the same slope for all elevator deflections (Fig. 4.5). This concurrence proves that this steepness is not due to issues in the experimental data but an aerodynamic characteristic of this wing planform, which needs further analysis.

4.3.1 Effect of Control deflections the lift and the drag coefficients

Ailerons have a minimal effect on the lift. Except for the elliptical wing planform after stall, where the aileron deflections deteriorate the lift coefficient (Fig. 4.6). Aileron deflections in the linear regime increase the drag coefficient, but it has a limited effect after the stall on the same coefficient (Fig. 4.7).

The positive elevator deflection shifts the lift coefficient curve up, while the negative deflection shifts it down like any flap (Fig. 4.8). But the positive elevator deflection increases the drag coefficient in the post-stall regime $\alpha \geq 12°$ with limited effect on in the pre-stall

regime (Fig. 4.9).

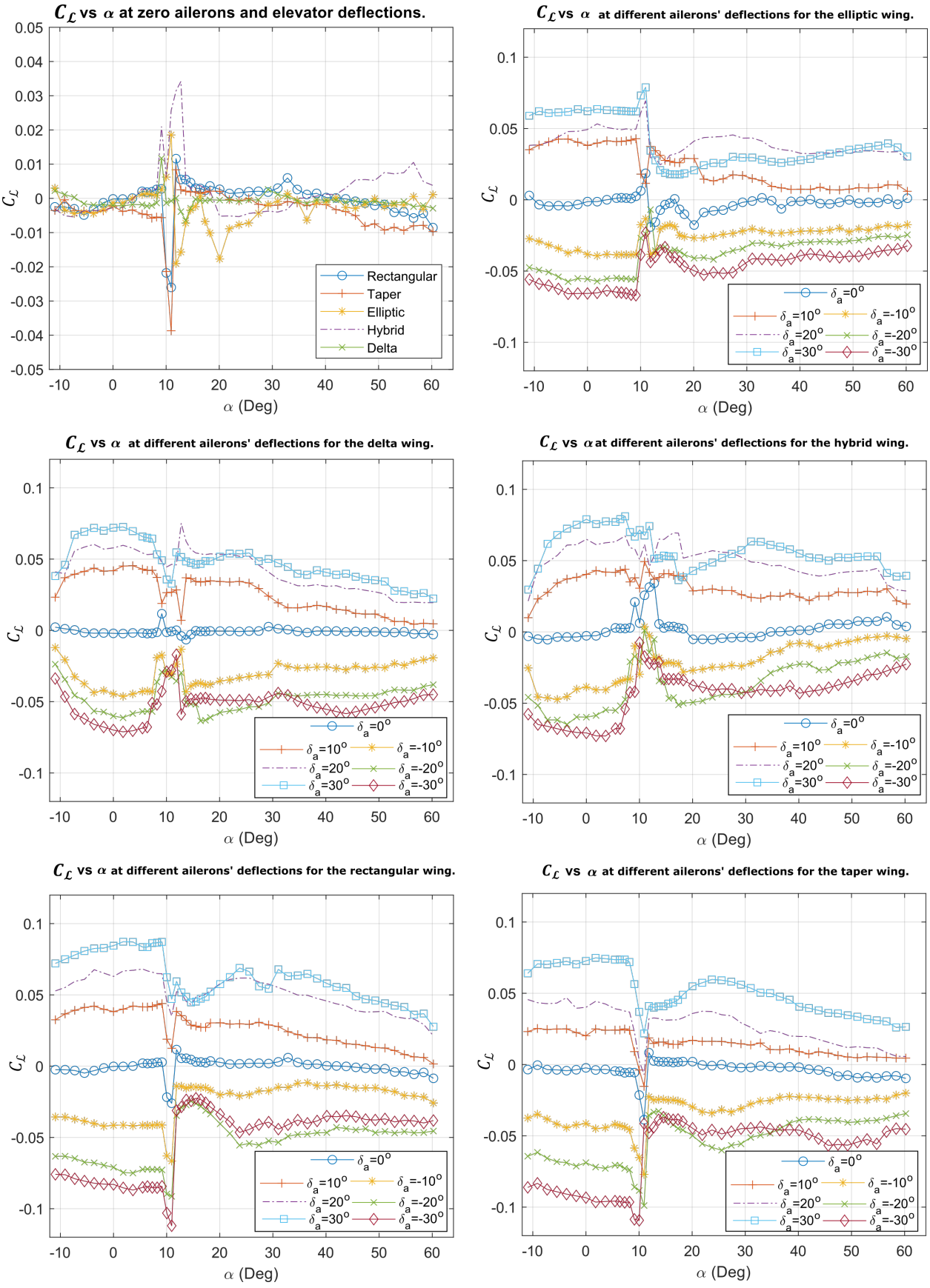

Figure 4.3: Effect of wing planform and ailerons on the rolling moment coefficient.

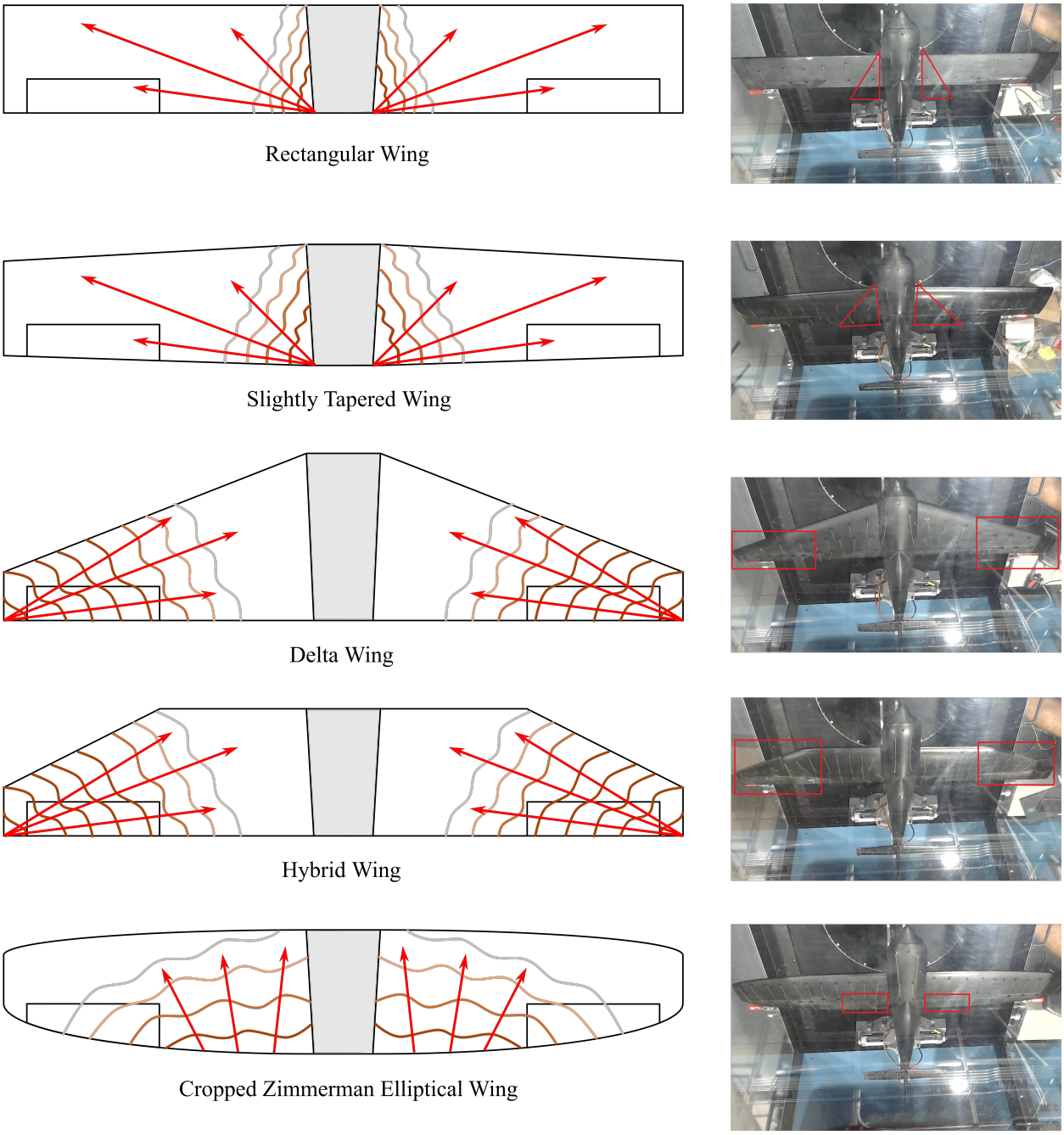

Figure 4.4: Stall progression patterns.

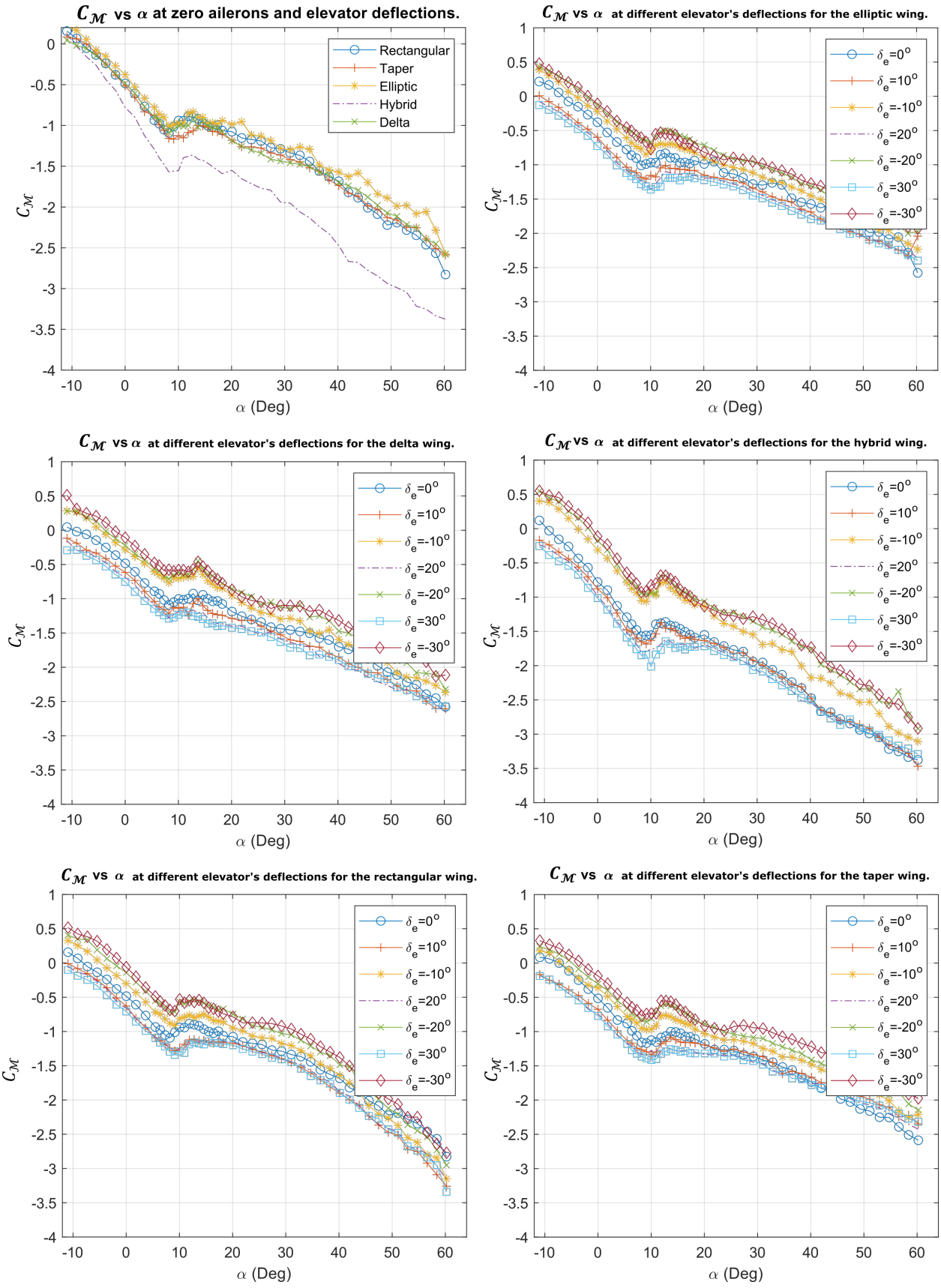

Figure 4.5: Effect of wing planform and elevator on the pitching moment coefficient.

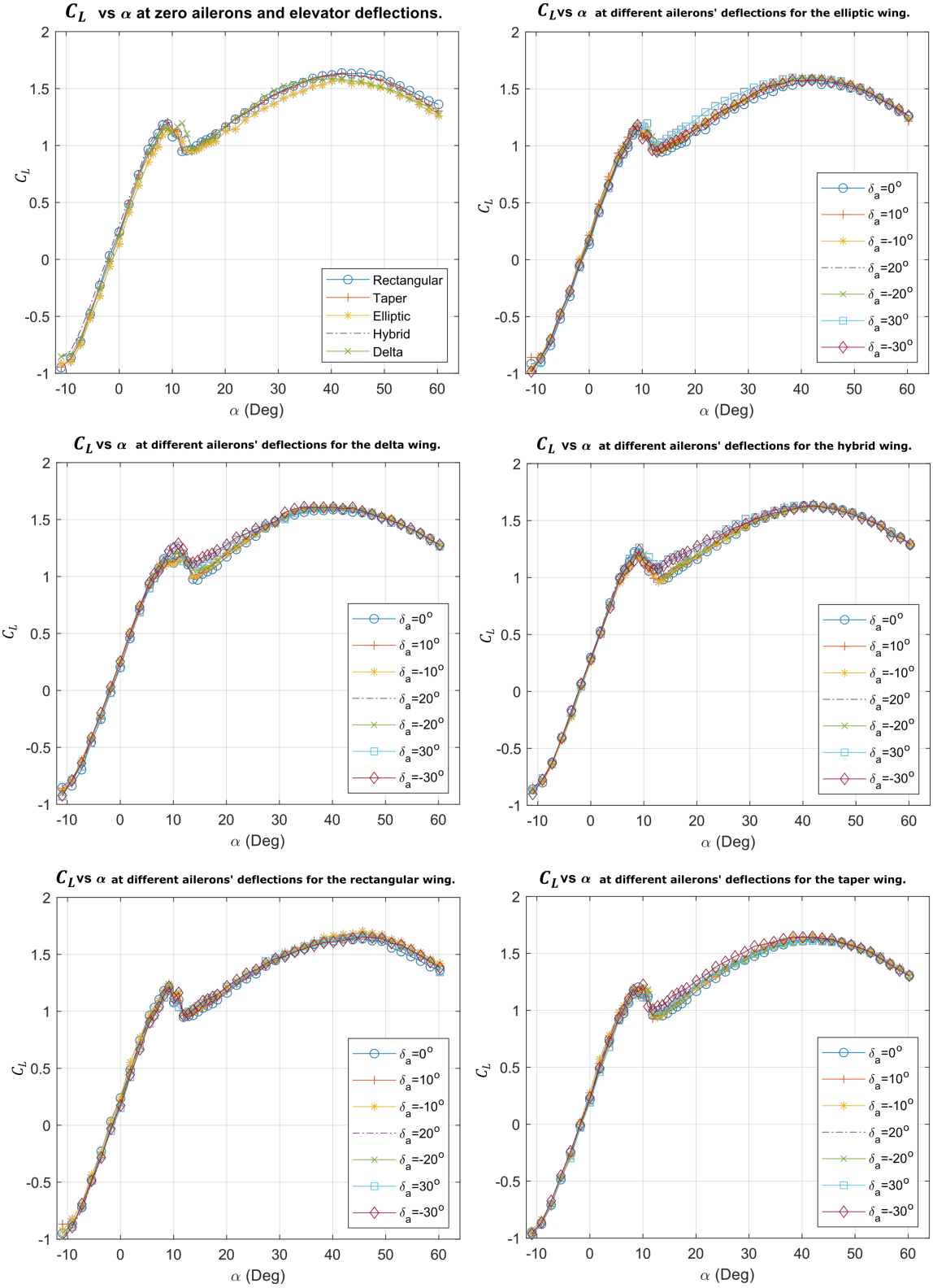

Figure 4.6: Effect of wing planform and ailerons on the lift coefficient.

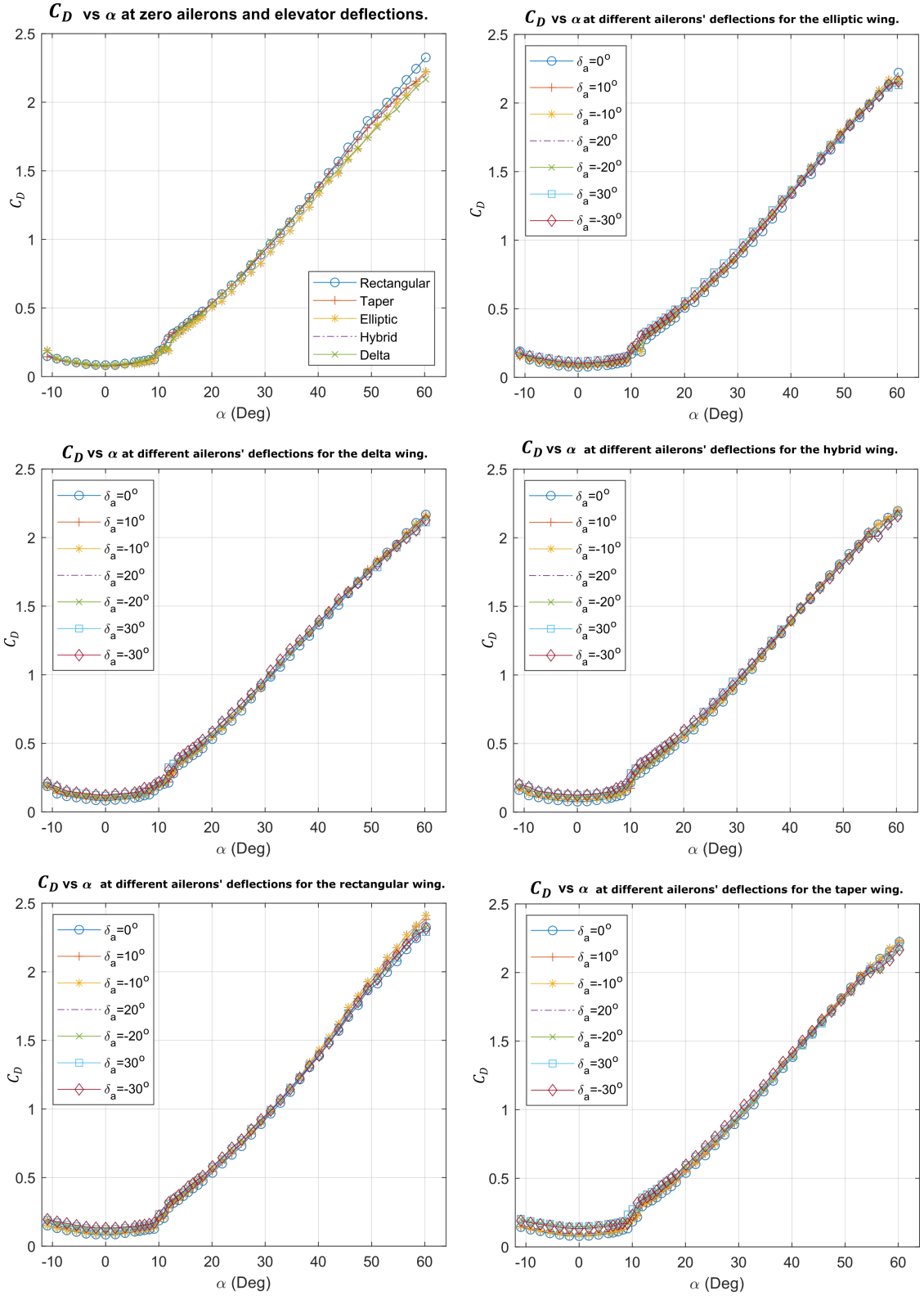

Figure 4.7: Effect of wing planform and ailerons on the drag coefficient.

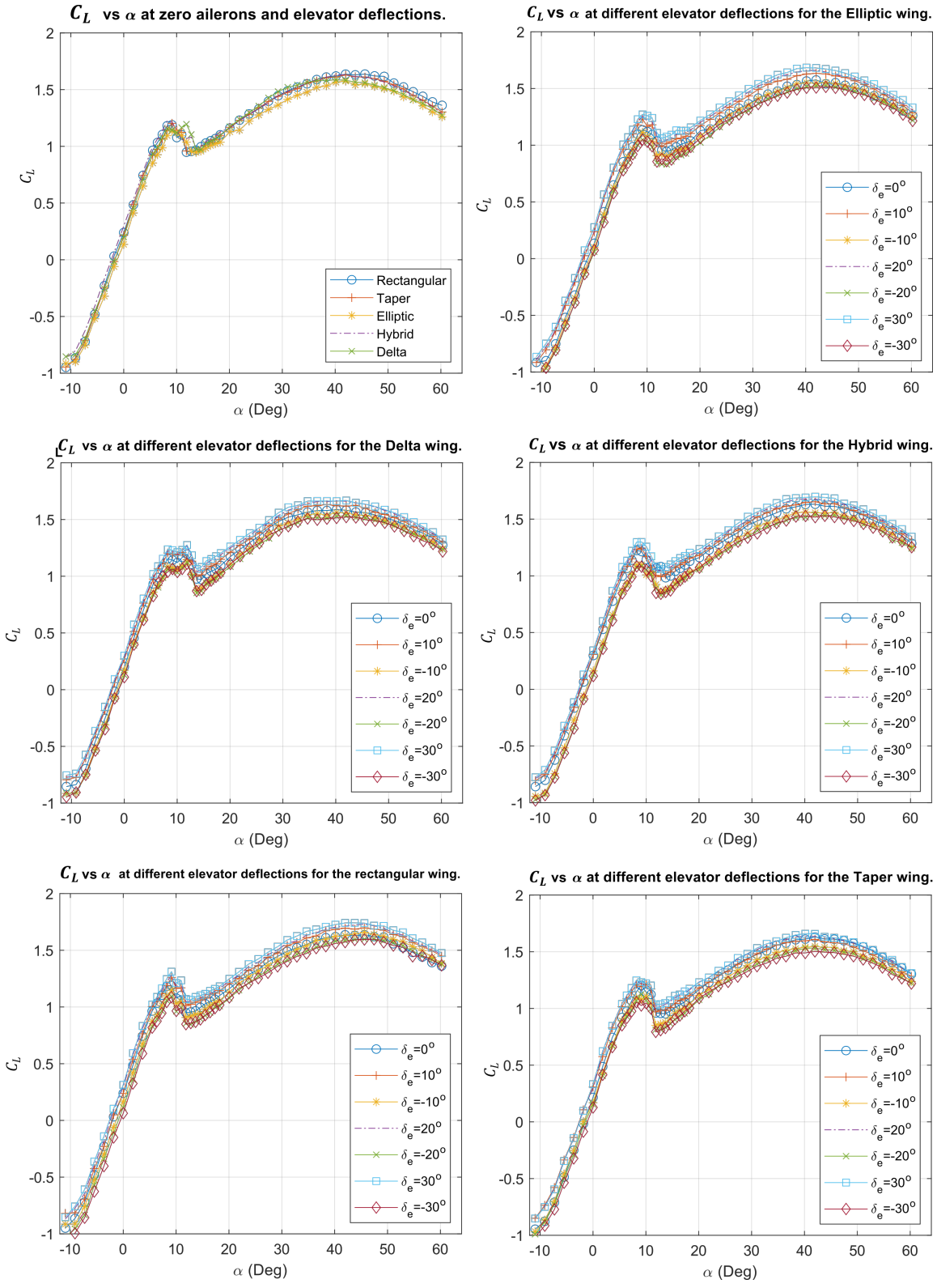

Figure 4.8: Effect of wing planform and elevator on the lift coefficient.

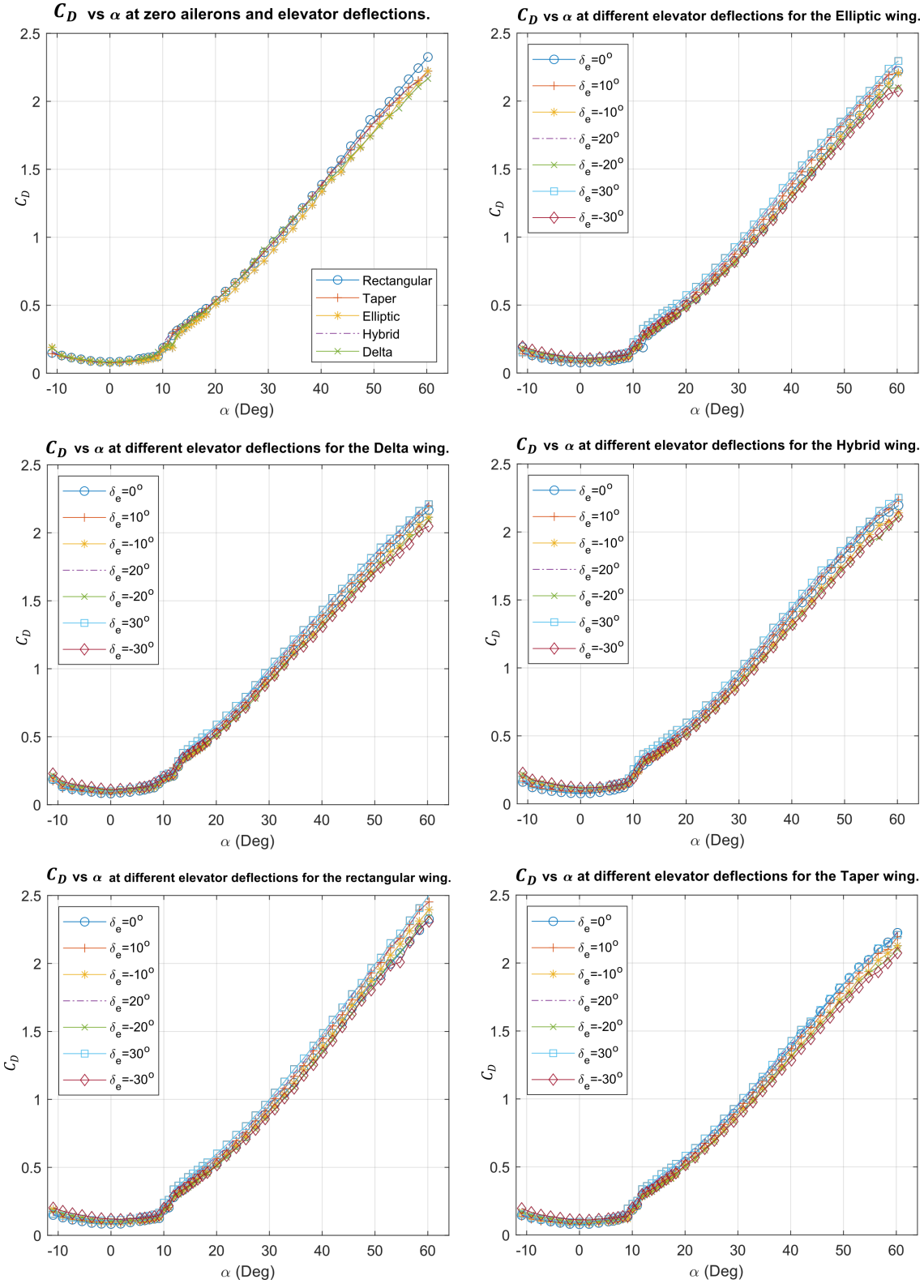

Figure 4.9: Effect of wing planform and elevator on the drag coefficient.

Chapter 5

Static and Dynamic Characteristics of the Aerodynamic Forces on Pitching Airfoils between 0 to 360 degrees Angle of Attack

Pitching airfoils of sections NACA 0012, NACA 0015, and NACA 0021 performing a complete rotation with different pitching rates/reduced frequencies are tested to study their aerodynamic characteristics at Reynolds numbers: 60,000, 100,000, and 135,000. Each wing is mounted vertically inside the wind tunnel test section. A four-axis load cell is mounted underneath the test section to measure the lateral forces and the two in-plane horizontal moments. A stepper motor, driven by a micro-stepping driver, is used to accurately control the angle of attack (AOA). An incremental digital encoder is used to measure the real-time variation of the AOA. All real-time signals are sampled using the same data acquisition system. Results show that the maximum lift coefficient and the corresponding angle of attack depends on pitch rate, where a significant increase in their values is observed at high angular

speeds.

5.1 Effects of the pitching rate/reduced frequency on the C_L curve

Figures 5.1, 5.2, 5.3, 5.4, 5.5, 5.6, 5.7, 5.8, and 5.9 show the time-variation of the lift coefficient at different angular speeds, Reynolds numbers and airfoil sections. The figures clearly show that the maximum lift coefficient $C_{L_{max}}$ increases with the increase in the pitching angular velocity ω. This increase in the $C_{L_{max}}$ is a delay in the stall. This delay in stall may be explained in simple terms as follows. In order for the fluid particles to avoid separation from the upper surface of the wing at high angles of attack, they need more adhesion to the wing surface to sustain a sufficient centripetal force necessary for the largely curved path. The effect of pitching angular velocity ω on this process is reducing the relative speed between the moving fluid particles and the leading edge (because the velocity of the leading edge due to pitching up is in the same direction as the flow). Since the relative velocity between the fluid particles and wing upper surface at the leading edge is reduced, less centripetal force will be required, and the separation will be delayed. On the other hand, since pitching is performed around 42% of the chord, the relative velocity is increased on most of the lower surface (58% of the chord), resulting in higher dynamic pressure. Both of these two effects lead to an increase in $C_{L_{max}}$. These figures 5.1, 5.2, 5.3, 5.4, 5.5, 5.6, 5.7, 5.8, and 5.9 show another result concerning the $C_{L_{min}}$, as $C_{L_{min}}$ is slightly decreased by the pitching rate/reduced frequency.

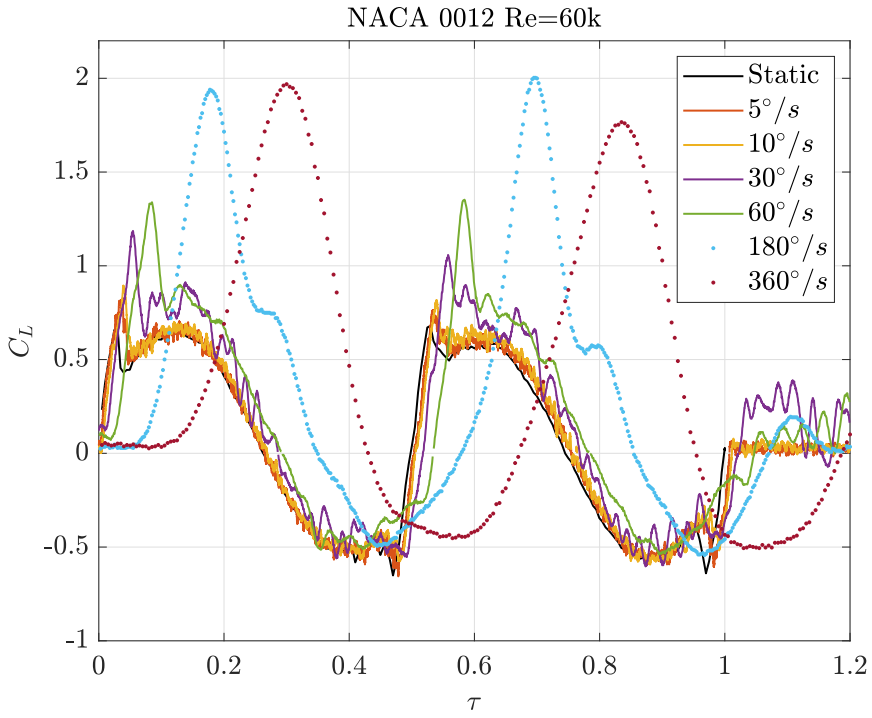

Figure 5.1: NACA 0012 C_L curve at different pitching rates/reduced frequencies at Re=60k

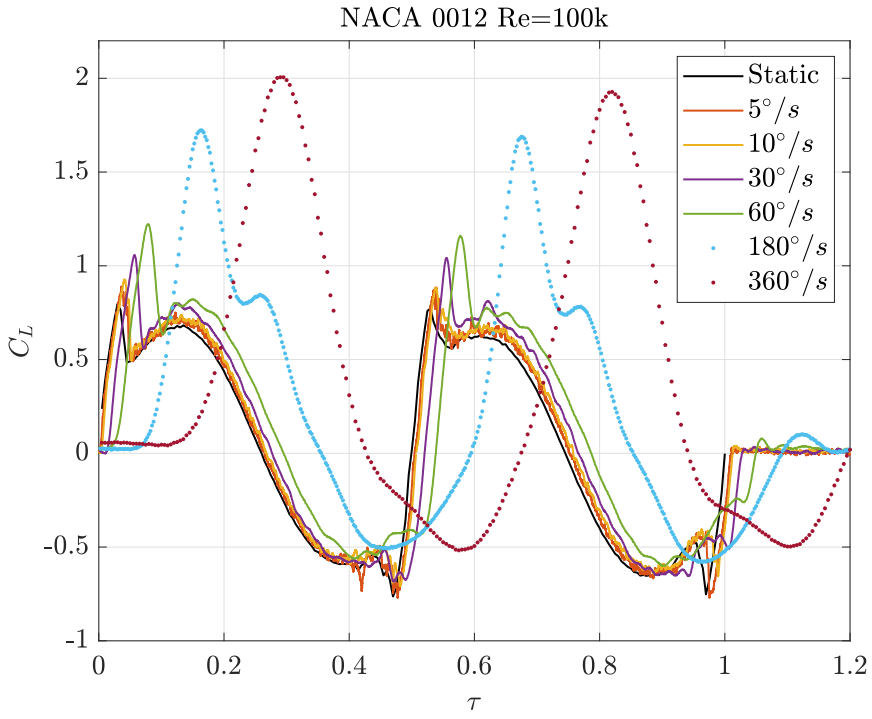

Figure 5.2: NACA 0012 C_L curve at different pitching rates/reduced frequencies at Re=100k

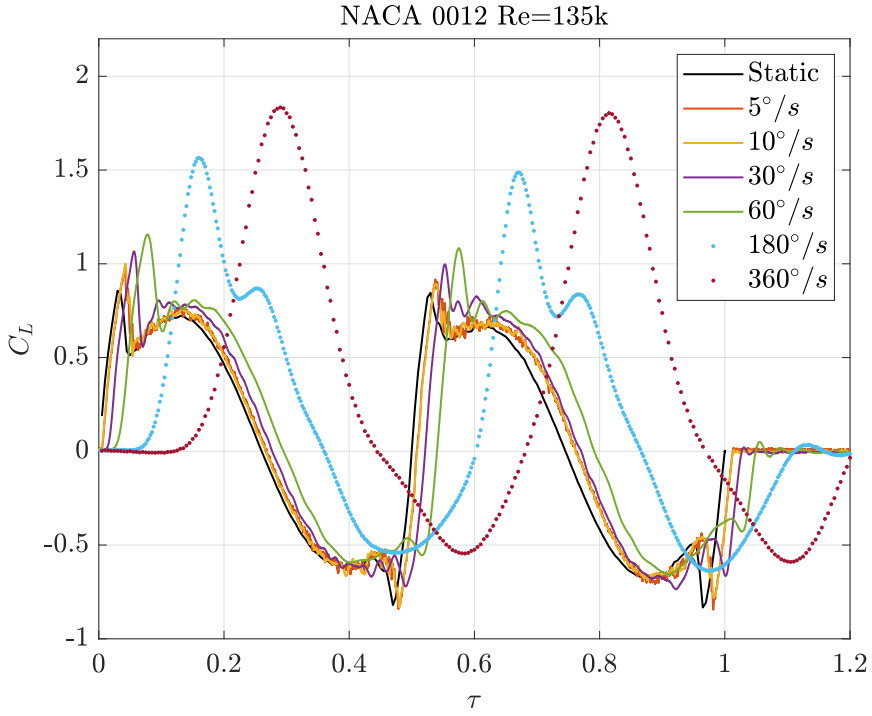

Figure 5.3: NACA 0012 C_L curve at different pitching rates/reduced frequencies at Re=135k

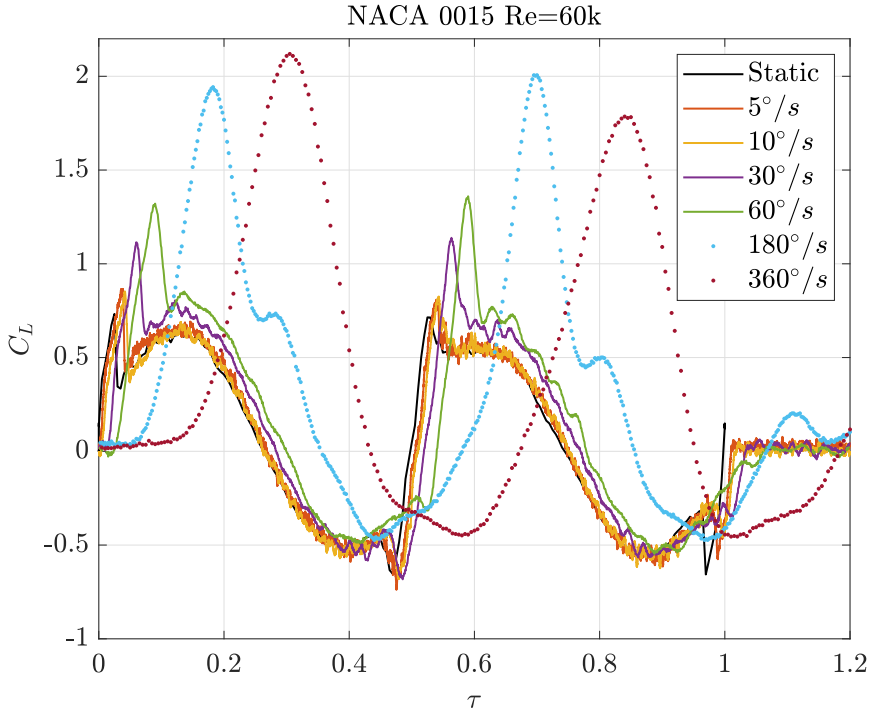

Figure 5.4: NACA 0015 C_L curve at different pitching rates/reduced frequencies at Re=60k

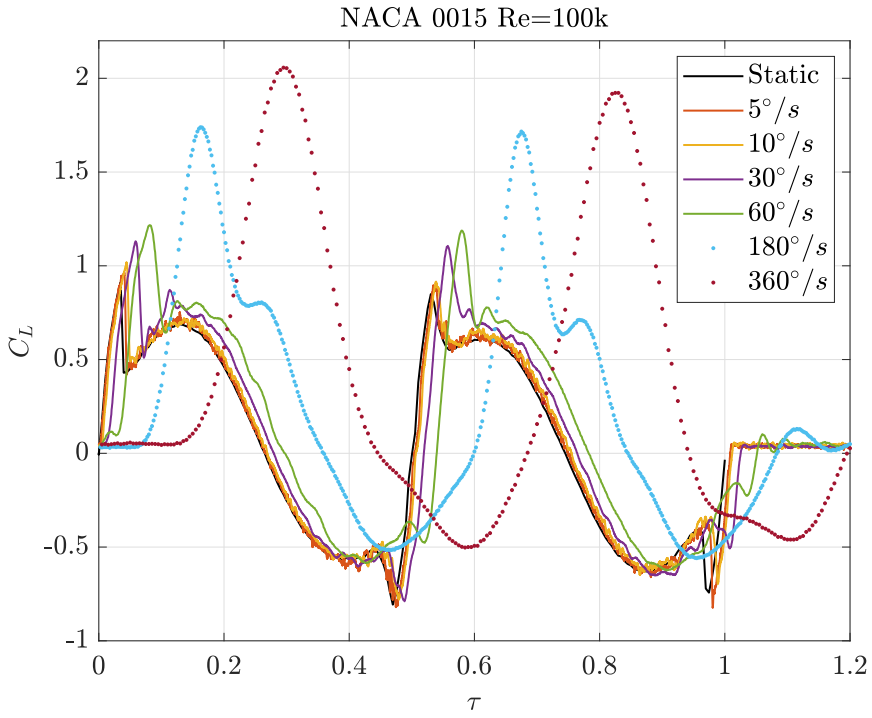

Figure 5.5: NACA 0015 C_L curve at different pitching rates/reduced frequencies at Re=100k

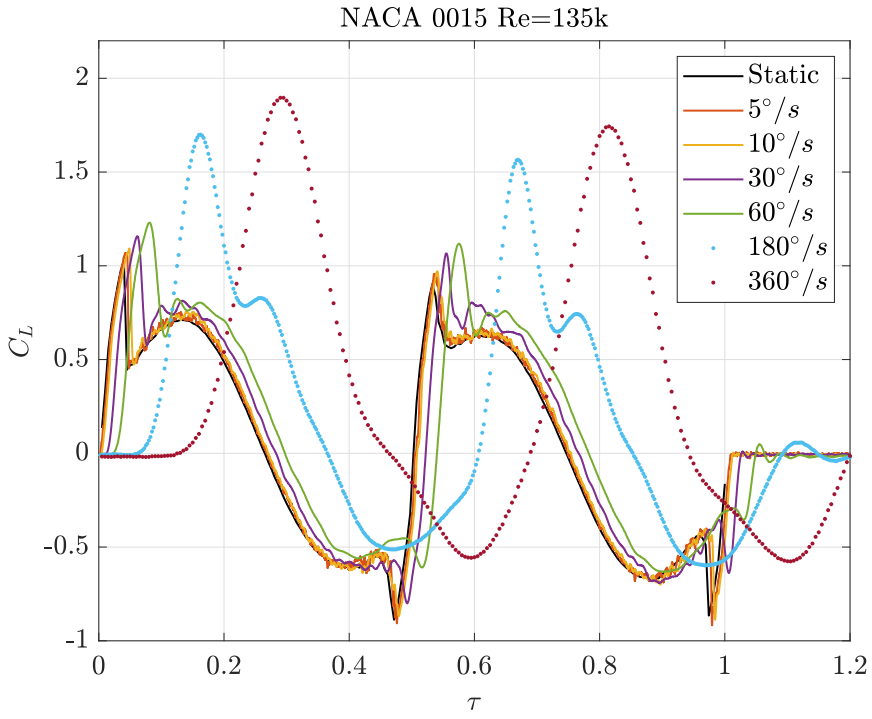

Figure 5.6: NACA 0015 C_L curve at different pitching rates/reduced frequencies at Re=135k

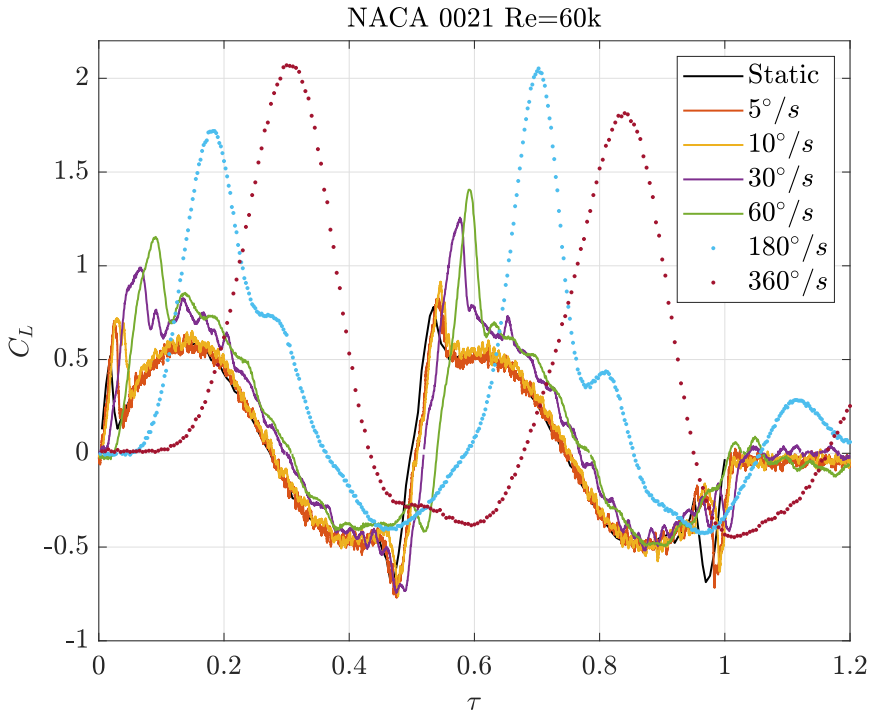

Figure 5.7: NACA 0021 C_L curve at different pitching rates/reduced frequencies at Re=60k

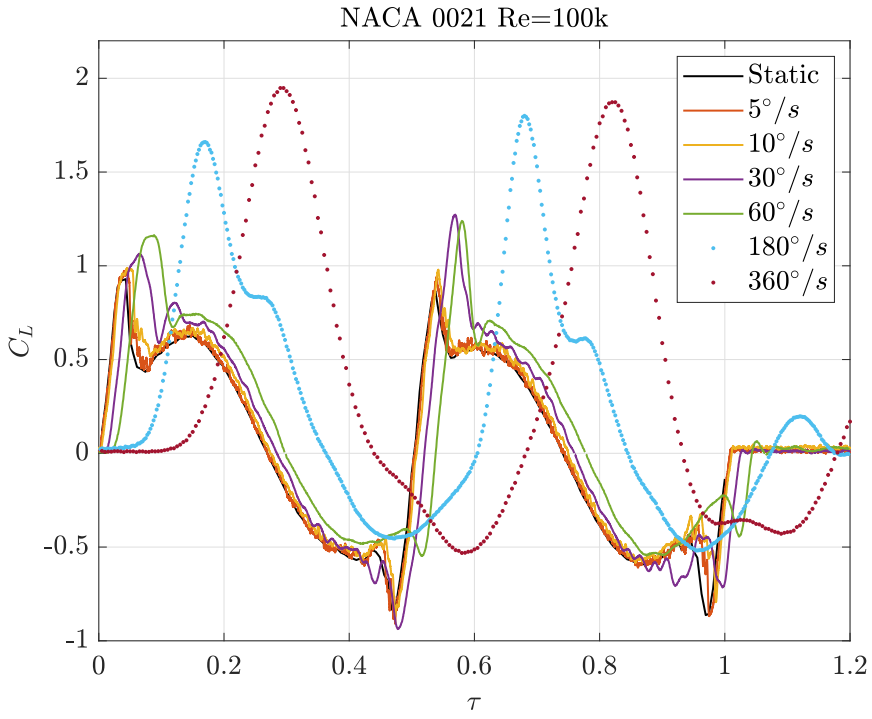

Figure 5.8: NACA 0021 C_L curve at different pitching rates/reduced frequencies at Re=100k

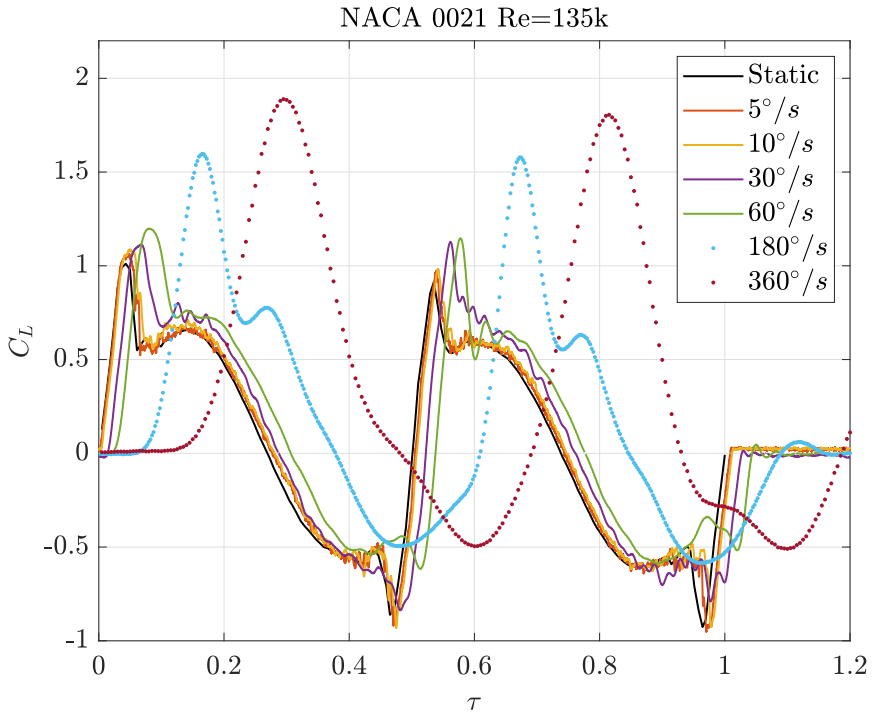

Figure 5.9: NACA 0021 C_L curve at different pitching rates/reduced frequencies at Re=135k

5.2 Effects of the Reynolds number on the C_L curve

Figures 5.10, 5.11, and 5.12 provide the same data of figures 5.1, 5.2, 5.3, 5.4, 5.5, 5.6, 5.7, 5.8, and 5.9 in a different format to accentuate the effect of Reynolds number. The figures show that the effect of Reynolds number in this range ($Re = 60k - 135k$) is not significant at low angular speeds; its effect increases with ω. The effect of Reynolds number is found to play an opposite role to the pitching velocity's. Since the viscosity does not change, the increase in the Reynolds number is just an increase in the fluid velocity. As discussed before, the larger the velocity, the larger the centripetal force required to maintain the largely curved path of the fluid particles (i.e., to keep the fluid particles attached to the wing's upper surface near the leading edge). This effect will promote separation in the immediate vicinity of the leading edge, which decreases $C_{L_{max}}$.

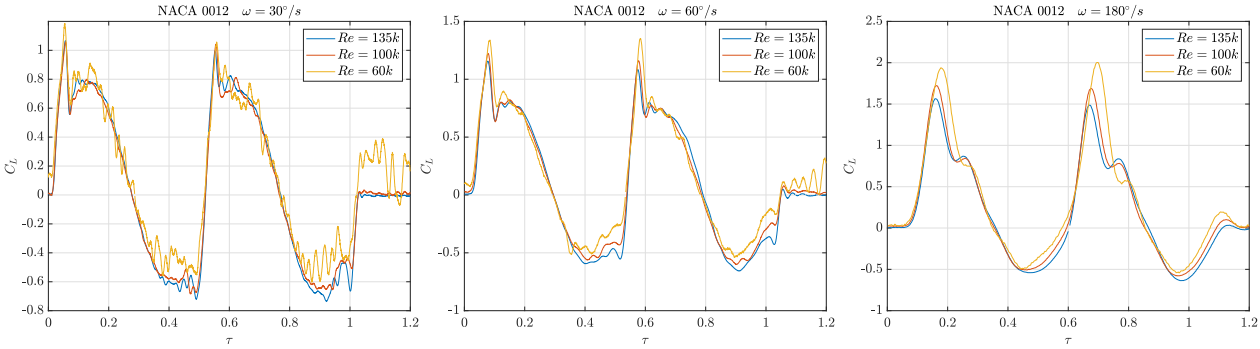

(a) (b) (c)

Figure 5.10: Rotating NACA0012 Wing at three different angular velocities:(a) $\omega = 30°/s$, (b) $\omega = 60°/s$, and (c) $\omega = 180°/s$.

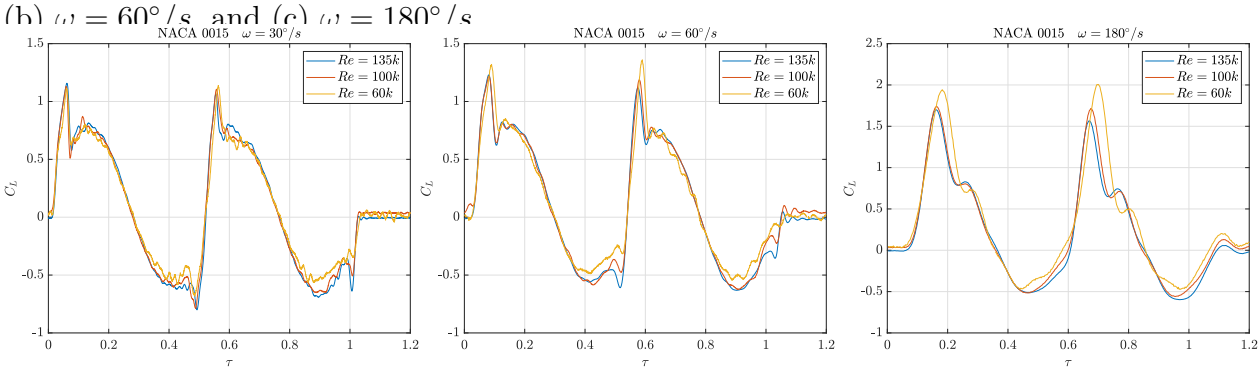

(a) (b) (c)

Figure 5.11: Rotating NACA0015 Wing at three different angular velocities:(a) $\omega = 30°/s$, (b) $\omega = 60°/s$, and (c) $\omega = 180°/s$.

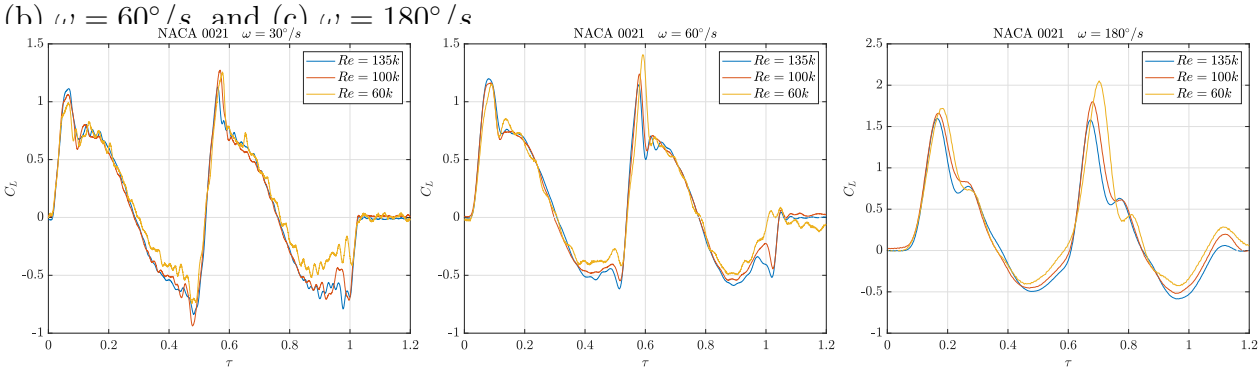

(a) (b) (c)

Figure 5.12: Rotating NACA0021 Wing at three different angular velocities:(a) $\omega = 30°/s$, (b) $\omega = 60°/s$, and (c) $\omega = 180°/s$.

5.3 Effects of wing cross section on the C_L curve

If the same analogy is used to study the effect of the wing cross-section on dynamic stall, the leading edge radius should be the main focus. The leading edge radius of each airfoil was measured as a percentage of the chord follows:

- NACA 0012:Leading edge radius equals 1.8% of the chord
- NACA 0015:Leading edge radius equals 2.4% of the chord
- NACA 0021:Leading edge radius equals 5.1% of the chord

The centripetal force required to maintain a particle moving with a certain velocity on a curvilinear path is directly proportional to curvature of the path (i.e., inversely proportional to the radius). So, the decreased leading edge radius (from NACA 0021 to NACA 0012) should expedite the stall similar to the effect of Reynolds number, but the leading edge separation is not only dictated by the surface curvature, but also how long the particle maximum lift coefficient of the pitching inverted airfoil (i.e., the moves on that curved path. In all wings, the stagnation point remains at the same angular displacement from the leading edge point since the angle of attack is the same. Despite this identical angular displacement, in the thicker airfoils, the fluid particle cut a longer distance s_p from the stagnation point to the end of the leading edge circular curvature (see Fig. 5.13); and the longer the distance along a curved path, the more susceptibility to separation. In conclusion, these two effects, the Re and the pitching rate/reduced frequency, seem to act against each other and may reduce the effect of the airfoil section on dynamic stall.

The last paragraph is in line with the results of $C_{L_{max}}$ over an inverted airfoil, as demonstrated in the second peak in the lift coefficient graphs (Figs. 5.1, 5.2, 5.3, 5.4, 5.5, 5.6, 5.7, 5.8, and 5.9). In most cases, the maximum lift coefficient of the pitching inverted airfoil

(i.e., the second peak) is larger than that of the normal airfoil. This can be explained in simple terms as follows. The relative velocity between the leading point (trailing edge in the inverted case) and the surrounding flow becomes slightly larger in the inverted airfoil case because of the increased rotation radius (58% versus 42%). For example, at Re=100k, the relative velocity at the leading edge equals 9.34m/s, while it is 9.19m/s at the trailing edge when the airfoil is inverted. So perhaps the major difference between the pitching wing in the conventional configuration and the inverted configuration is the curvature of the path near the leading point. While the sharpness of the trailing edge (the leading point in the inverted case) may be expected to promote separation, the forwardly inclined surface of the airfoil near the leading point (i.e., trailing edge) seem to guide the airflow along the curved path, mitigating the sharpness effect of the leading point, perhaps in the expense of additional drag. As a result, the maximum lift coefficient $C_{L_{max}}$ of the inverted airfoil (the second peak) is slightly higher than $C_{L_{max}}$ of the normal airfoil (the first peak), particularly for NACA 0021, as shown in figures 5.1, 5.2, 5.3, 5.4, 5.5, 5.6, 5.7, 5.8, and 5.9.

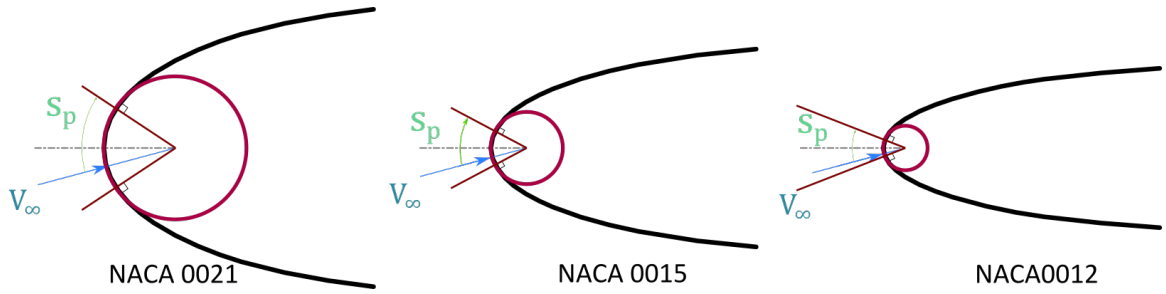

Figure 5.13: Magnified schematic for the distance s_p cut by a fluid particle over the leading edge circular surface for NACA0021, 0015, and 0012 at the same AOA.

The interpretations of these experimental results found in this section could be supported by more experimental tests using the same airfoils at the same different pitching rate/reduced frequency but changing the location of the center of rotation to different locations on the chord, including the leading edge position itself. This parameter will enable studying the leading edge relative velocity effect at the same pitching rate/reduced frequency. Also, it requires testing symmetric sections like a flat plate and ellipse of different aspect ratios.

5.4 Effects of Reynolds number and pitching rate/reduced frequency on $C_{L_{max}}$

One of the interesting results of this experiment is the combined effect of the Re, the pitching rate/reduced frequency and the airfoil section on $C_{L_{max}}$ (Figures: 5.14, 5.15, 5.16. $C_{L_{max}}$ increases with the pitching rate in an almost cubic relation $C_{L_{max}} \propto \sqrt{\omega}$. This means the $C_{L_{max}}$ will saturate at certain pitching rate/reduced frequency. Since the maximum pitching rate of this experiment is $360°/Sec$ (equivalent to reduced frequency = 0.0115 Hz),and the slope of the $C_{L_{max}}$ becomes close to zero at this frequency, the saturation is expected to happen on a frequency slightly higher than the maximum frequency of this experiment. The parameters of this cubic relation depend on the Re as the three Re curves are not identical. This dependence splits the relation between the $C_{L_{max}}$ and the Re into two regions for each airfoil as follows:

- NACA 0012: $C_{L_{max}} \propto \frac{1}{Re}$ for $\alpha \leq 25°$ and $C_{L_{max}} \propto Re$ for $\alpha \geq 25°$.
- NACA 0015: $C_{L_{max}} \propto \frac{1}{Re}$ for $\alpha \leq 40°$ and $C_{L_{max}} \propto Re$ for $\alpha \geq 40°$.
- NACA 0021: $C_{L_{max}} \propto \frac{1}{Re}$ for $\alpha \leq 100°$ and $C_{L_{max}} \propto Re$ for $\alpha \geq 100°$.

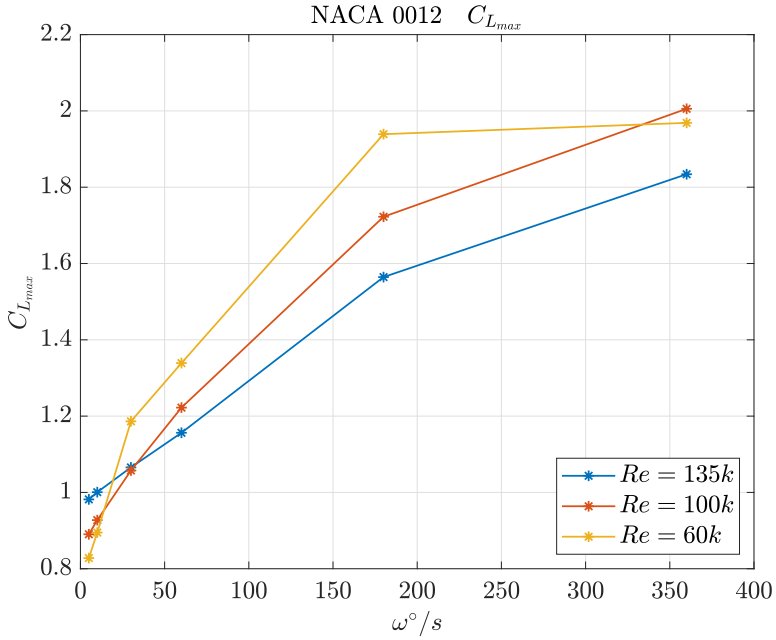

Figure 5.14: NACA 0012 $C_{L_{max}}$ Vs pitching rate/reduced frequency Reynolds numbers

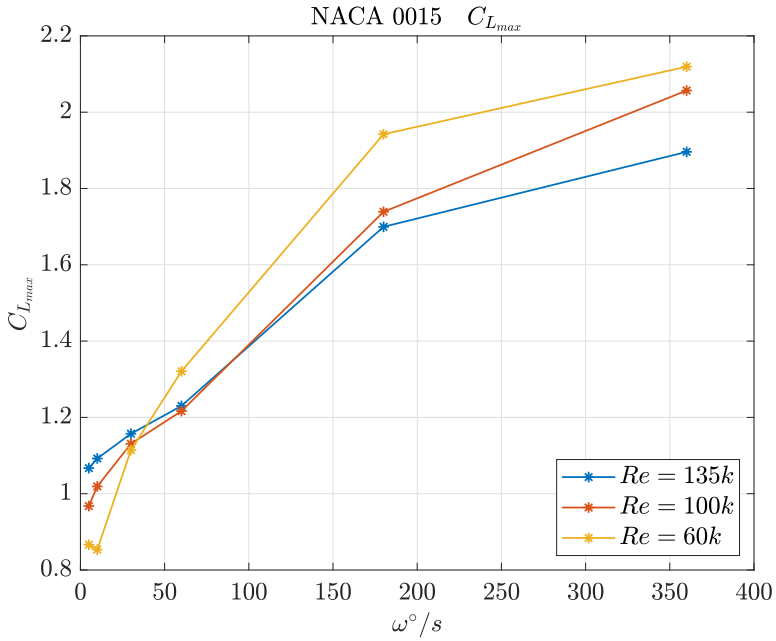

Figure 5.15: NACA 0015 $C_{L_{max}}$ Vs pitching rate/reduced frequency Reynolds numbers

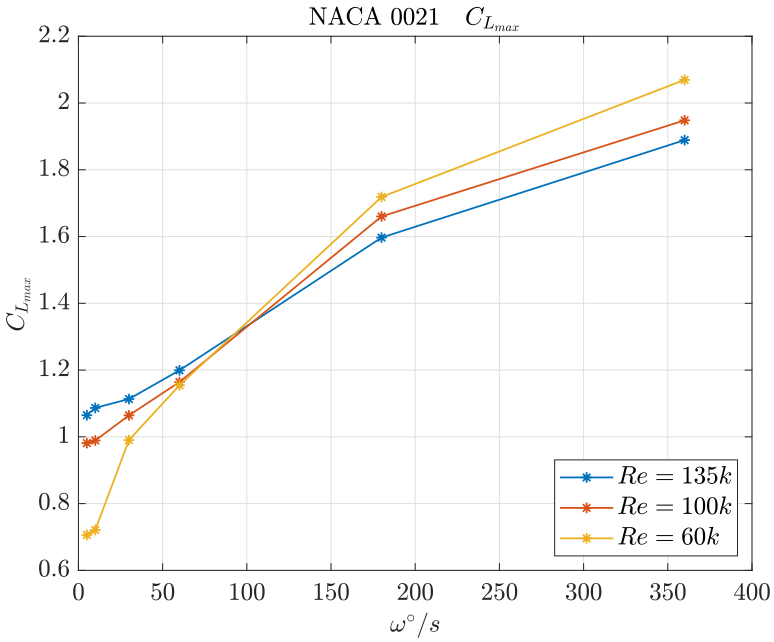

Figure 5.16: NACA 0021 $C_{L_{max}}$ Vs pitching rate/reduced frequency Reynolds numbers

Chapter 6

Conclusions and Recommendations

6.1 Conclusions

Wing drop is a vast rolling moment that is caused by inevitable asymmetric lift distribution at stall. An unstable, uneven stall between the two wing laves is the reason for this asymmetric lift distribution and asymmetric drag distribution as well. This asymmetric distribution of the resultant aerodynamic force causes lateral-directional instability at stall. Ailerons become partially ineffective at stall, which degrades the roll control authority and handling qualities at stall.

Wing drop typically happens at the critical stall angle without the aid of asymmetric catalytic maneuvers/control inputs such as aileron deflection and/or rudder's deflection, side slip, side wind, dirty wing, etc. Those catalytic inputs accelerate the wing drop before reaching the critical stall angle.

The wing planform determines where the stall starts on the wing's upper surface. The stall starts on the inboard wing sections near the trailing edge in the rectangular and slightly

tapered wing planforms. The stall starts far from the fuselage in the cropped elliptical wing but is still away from the tip sections where the ailerons are located. On the contrary, the outboard wing sections of the delta and the hybrid wing planforms stall first.

Wing planform affects the magnitude and the direction of the rolling moment associated with the wing drop phenomenon. The direction of the wing drop is unpredictable and independent of the direction of the aileron direction in the rectangular and slightly tapered wing planforms. In contrast, the aileron deflection dictates the direction of wing drop in the delta and hybrid wing planforms.

The rolling control authority deteriorates significantly during the wing drop and after the two wings stall. The rectangular and slightly tapered wings provide better rolling control authority during stall than the tapered or elliptical wing planforms.

Both pitch rate and Reynolds number affect the dynamic stall's maximum lift coefficient $C_{L_{max}}$. A larger pitching rate increases $C_{L_{max}}$, while a larger Reynolds number decreases it. These behaviors can be well explained if we postulate that the flow can sustain up to a specific maximum curvature limit (centripetal force). In this case, the effect of increasing the Reynolds number (i.e., increasing velocity) demands more centripetal force, promoting separation. On the other hand, the larger the pitching angular velocity, the larger the translational speed of the leading edge (which is in the same direction as the oncoming flow during pitching up); the smaller the relative velocity of the leading edge with respect to the surrounding flow, which demands less centripetal force, hence delaying separation and increasing $C_{L_{max}}$. The wing cross-section's thickness and the leading edge's radius seem to have fewer effects on $C_{L_{max}}$.

6.2 Recommendations

6.2.1 Recommendations on the Experimental Setups

The airplane stability experiment could be automated using a stepper motor to control the model positioning mechanism, similar to the rotating wings experiment. This automation will lessen the experiment time from 6 hours to less than fifteen minutes. Most importantly, this will help study the dynamic stall on the airplane stability and control authority in stall. As discussed in chapter 1, we expect rapid pitching during the stall instability region will eliminate the wing drop and this lateral-directional instability at stall.

Flow visualization using other methods like smoke and oil will give a better visualization of the stall progression patterns on the upper surface. Using larger airplane models in a larger wind tunnel with a controllable ruder will help in investigating the yaw moment divergence and the rudder effectiveness at stall.

We built six wings of different airfoils with a smaller chord to investigate the unsteady aerodynamics of low Reynolds numbers. Testing those wings will help understand the effect of the airfoil and the leading edge radius on the dynamic stall phenomenon. The new experimental setup we built in the last few months can directly measure the drag force. In addition, because of its increased stiffness, the system can run under higher dynamic pressures (i.e., higher Reynolds numbers).

6.2.2 Recommendation for Future Work

The blade of a vertical axis wind turbine (VAWT) is just a rotating wing, as in our second experiment. The rapid pitching motion in this experiment resembles the rotational motion of these VAWTs. This pitching motion increases the area under the positive portions and

decreases the negative portions of the $C_L - \alpha$ curve (Fig.6.1). The blade offset angle ϕ could be optimized using these complete curves to maximize the output torque at the center of rotation of the turbine.

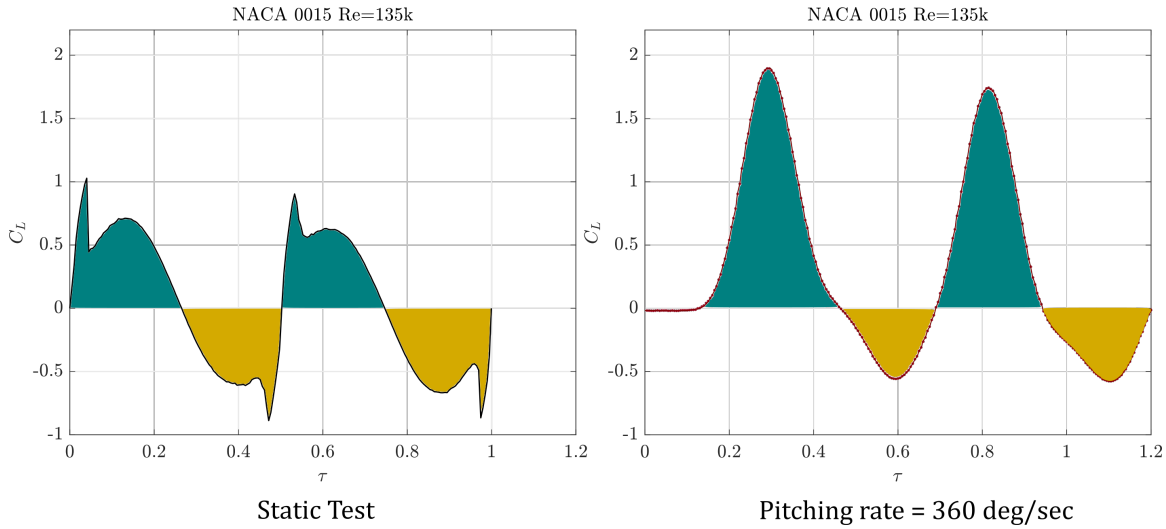

Figure 6.1: Effect of the wing rotational motion on the positive and negative portions of the $C_L - \alpha$ curve

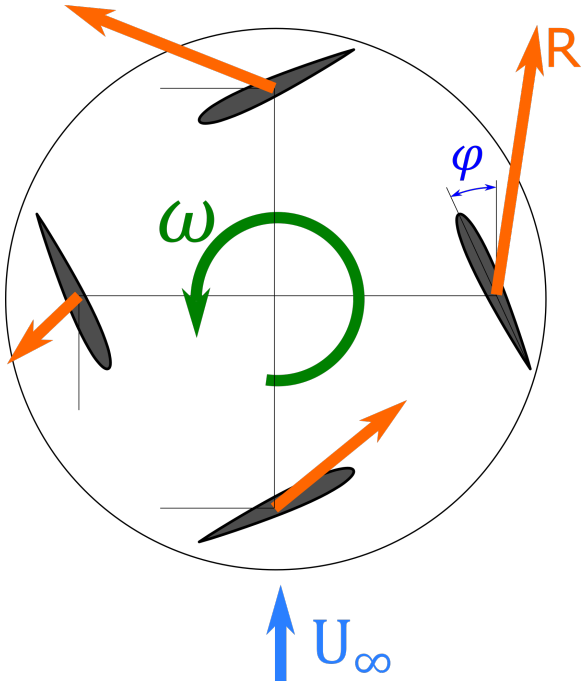

Figure 6.2: Blade Offset angle optimization ϕ for maximizing the output torque of VAWT

6.2.3 Proposal for general aviation airplanes wing drop and incipient spin detection system

It may be challenging to upgrade GA airplanes with wing drop detection systems like those in commercial airplanes. In this section, we propose a simple upgrade that will notify the pilot of an ongoing wing drop and its direction. This proposal is based on the finding of the effect of the wing planform on stall progression patterns. After the designer determines the stall progression pattern of his wing planform, they can install three or four miniature piezoelectric pressure transducers where the stall starts, arranged in a triangular form (Fig. 6.3. These sensors are cheap and can respond quickly to the airplane pitching rate. If the flow is attached, the pressure readings of the three sensors will be constant and change together at the same rate. If the stall starts on a particular wing, the three sensors of this wing will give oscillating readings without having any correlation because of the detached flow. These oscillations mean the stall starts at this wing, and the wing drop is in progress. Once the monitoring system, microcontroller, or microcomputer, detects these uncorrelated oscillations, it should give an alarm for a progressing wing drop.

6.2.4 Recommendation for the Regulating Authorities (FAA and CASA)

As discussed in detail in chapter 1, we propose changing the spin definition to stress that lateral-directional instability (which happens naturally at the critical stall angle) will provoke spin without the need for any other catalytic factor. If any asymmetric maneuvers and control inputs such as aileron deflection and rudder's deflection, side slip, side wind, or dirty wing exist, it will accelerate wing drop and spin even before reaching the critical stall angle. Based on that, we proposed this definition for the spin:

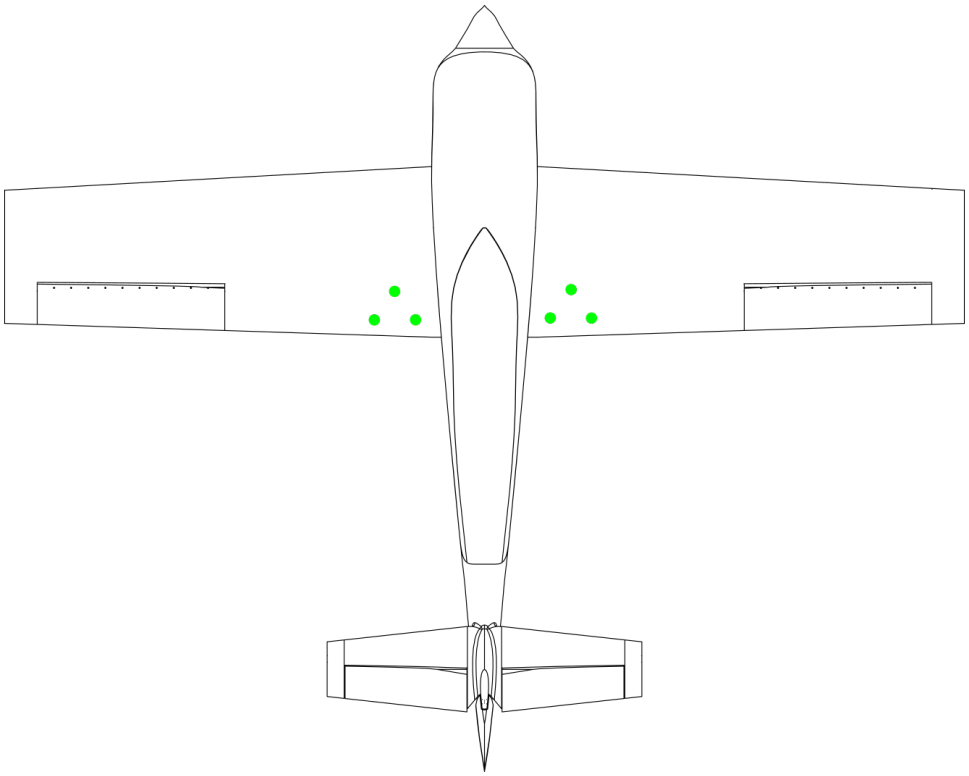

Figure 6.3: Proposed solution for cheap wing drop and incipient spin detection system using miniature pressure sensors

Spin is a sustained rotational falling motion of an airplane along a helical (corkscrew) path. Spin results from lateral-directional instability, occurring naturally at the critical stall angle. The lateral instability is known as Wing drop, which is a vast rolling moment that occurs due to asymmetrical lift distribution, while the directional instability occurs because of a yaw moment due to asymmetric drag distribution. The rolling moment (wing drop) and the yaw moment typically occur when the airplane flies at the critical stall angle without the need for any other factors. Spin could be accelerated before reaching the critical stall angle with the aid of asymmetric catalytic maneuvers/control inputs such as aileron deflection and/or rudder deflection, side slip, side wind, dirty wing, propeller vortex, etc.

Bibliography

[1] *Airplane Flying Handbook (FAA-H-8083-3C).* Federal Aviation Administration (FAA), US Department of Transportation Federal Aviation Administration, 2021.

[2] J. Collins and A. Sable, "Stall and spin accidents: Keep the wings flying," AOPA Air Safety Institute, Frederick, MD, Tech. Rep., 2017.

[3] N. Fala, "An analysis of fixed-wing stall-type accidents in the united states," *Aerospace*, vol. 9, no. 4, p. 178, 2022.

[4] J. R. Chambers, "Concept to reality: contributions of the langley research center to us civil aircraft of the 1990s," NASA, Tech. Rep., 2003.

[5] R. Whitford, *Design For Air Combat.* Jane's Publishing Company limited, 1987.

[6] G. E. Erickson, "High angle-of-attack aerodynamics," *Annual review of fluid mechanics*, vol. 27, no. 1, pp. 45–88, 1995.

[7] L. W. Carr, "Progress in analysis and prediction of dynamic stall," *Journal of aircraft*, vol. 25, no. 1, pp. 6–17, 1988.

[8] W. J. McCroskey, "The phenomenon of dynamic stall." National Aeronuatics and Space Administration Moffett Field Ca Ames Research ..., Tech. Rep., 1981.

[9] H. Babinsky, "How do wings work?" *Physics Education*, vol. 38, p. 497, 11 2003.

[10] T. Von Kármán, *Aerodynamics: selected topics in the light of their historical development.* Courier Corporation, 1954.

[11] J. Hoffren, "Quest for an improved explanation of lift," in *39th Aerospace Sciences Meeting and Exhibit*, 2001, p. 872.

[12] C. Gonzalez and H. E. Taha, "A variational theory of lift," *Journal of Fluid Mechanics*, vol. 941, 2022.

[13] H. E. Taha and C. Gonzalez, "The flow over a flat plate: Did kutta get it right?" in *AIAA SCITECH 2022 Forum*, 2022, p. 1665.

[14] R. H. Liebeck and A. I. Ormsbee, "Optimization of airfoils for maximum lift," *Journal of Aircraft*, vol. 7, no. 5, pp. 409–416, 1970.

[15] V. Lienhard, J. H. and I. Lienhard, J. H., "Velocity Coefficients For Free Jets From Sharp-Edged Orifices," *Journal of Fluids Engineering*, vol. 106, no. 1, pp. 13–17, 03 1984. [Online]. Available: https://doi.org/10.1115/1.3242391

[16] A. J. Kox, M. J. Klein, R. Schulmann, and C. Kilmister, "The collected papers of albert einstein, vol. 6. the berlin years: 1914-17," *Annals of Science*, vol. 55, no. 3, 1998.

[17] L. Prandtl, "Motion of fluids with very little viscosity," Tech. Rep., 1928.

[18] H. Schlichting, "Boundary layer theory," 1979.

[19] H. Schlichting and K. Gersten, *Boundary-layer theory*. Springer Science & Business Media, 2003.

[20] H. Schlichting and E. Truckenbrodt, *Aerodynamics of the Airplane*. McGraw-Hill, 1970.

[21] S. Hoerner, *Fluid-Dynamic Drag*. Hoerner Fluid Dynamics P.O. Box 21992 Bakersfield, CA 93390, USA, 1965.

[22] E. Torenbeek, *Synthesis of subsonic airplane design: an introduction to the preliminary design of subsonic general aviation and transport aircraft, with emphasis on layout, aerodynamic design, propulsion and performance*. Springer Science & Business Media, 2013.

[23] L. Prandtl, "Königliche gesellschaft der wissenschaften zu göttingen," *ed. Tragflügeltheorie*, 1918.

[24] J. C. Sivells, "Maximum-lift and stalling characteristics of wings," in *NACA: Univ. Conf. on Aerodyn.*, 1948.

[25] A. Pope, "On airfoil theory and experiment," *Journal of the Aeronautical Sciences*, vol. 15, no. 7, pp. 407–410, 1948.

[26] R. Shevell, "Aerodynamic bugs-can cfd spray them away?" in *3rd Applied Aerodynamics Conference*, 1985, p. 4067.

[27] M. Fouda and H. E. Taha, "Effect of wing planform on airplane stability and control authority in stall," in *AIAA Scitech 2022 Forum*, 2022, p. 1161.

[28] H. Hurt, *Aerodynamics for Naval Aviators: NAVWEPS 00-80T-80*. Direction of Commander, Naval Air Systems Command, 1965.

[29] *Flying Qualities Textbook: Volume II, Part 2*. USAF Test Pilot School, Edwards Air force Base, California, 1990.

[30] J. Roskam, *Airplane flight dynamics and automatic flight controls*. DARcorporation, 1995.

[31] H. E. Taha, A. Hassan, and M. Fouda, "Nonlinear flight physics of the lie bracket roll mechanism," *Nonlinear Dynamics*, vol. 106, no. 3, pp. 1627–1646, 2021.

[32] A. M. Hassan and H. E. Taha, "Design of a nonlinear roll mechanism for airplanes using lie brackets for high alpha operation," *IEEE Transactions on Aerospace and Electronic Systems*, vol. 57, no. 1, pp. 462–475, 2020.

[33] ——, "A novel airplane roll mechanism: Nonlinear motion planning approach," in *AIAA Scitech 2019 Forum*, 2019, p. 0912.

[34] ——, "Geometric control formulation and nonlinear controllability of airplane flight dynamics," *Nonlinear Dynamics*, vol. 88, no. 4, pp. 2651–2669, 2017.

[35] S. H. Strogatz, *Nonlinear dynamics and chaos: with applications to physics, biology, chemistry, and engineering*. CRC press, 2018.

[36] J. Chambers, "Overview of stall/spin technology," in *6th Atmospheric Flight Mechanics Conference*, 1980, p. 1580.

[37] R. C. Nelson and A. Pelletier, "The unsteady aerodynamics of slender wings and aircraft undergoing large amplitude maneuvers," *Progress in Aerospace Sciences*, vol. 39, no. 2-3, pp. 185–248, 2003.

[38] M. Fouda and H. E. Taha, "Experimental investigations of airplane maneuverability and stability in stall," in *AIAA Scitech 2021 Forum*, 2021, p. 1819.

[39] W. Sears, "Some recent developments in airfoil theory," *Journal of the Aeronautical Sciences*, vol. 23, no. 5, pp. 490–499, 1956.

[40] W. R. Sears, "A new treatment of the lifting-line wing theory, with applications to rigid and elastic wings," *Quarterly of Applied Mathematics*, vol. 6, no. 3, pp. 239–255, 1948.

[41] R. S. Schairer, "Unsymmetrical lift distributions on a stalled monoplane wing," Ph.D. dissertation, California Institute of Technology, 1939.

[42] A. J. Ross, "Investigation of nonlinear motion experienced on a slender-wing research aircraft," *Journal of Aircraft*, vol. 9, no. 9, pp. 625–631, 1972.

[43] J. Katz, "Wing/vortex interactions and wing rock," *Progress in aerospace sciences*, vol. 35, no. 7, pp. 727–750, 1999.

[44] C.-H. Hsu and C. E. Lan, "Theory of wing rock," *Journal of Aircraft*, vol. 22, no. 10, pp. 920–924, 1985.

[45] L. Nguyen, L. Yip, and J. Chambers, "Self-induced wing rock of slender delta wings," in *7th Atmospheric Flight Mechanics Conference*, 1981, p. 1883.

[46] J. R. Chambers and R. M. Hall, "Historical review of uncommanded lateral-directional motions at transonic conditions," *Journal of aircraft*, vol. 41, no. 3, pp. 436–447, 2004.

[47] R. M. Hall and S. H. Woodson, "Introduction to the abrupt wing stall program," *Journal of Aircraft*, vol. 41, no. 3, pp. 425–435, 2004.

[48] R. M. Hall, S. H. Woodson, and J. R. Chambers, "Accomplishments of the abrupt-wing-stall program," *Journal of Aircraft*, vol. 42, no. 3, pp. 653–660, 2005.

[49] J. Lamar, F. Capone, and R. Hall, "Aws figure of merit (fom) developed parameters from static, transonic model tests," in *41st Aerospace Sciences Meeting and Exhibit*, 2003, p. 745.

[50] B. Owens, F. Capone, R. Hall, J. Brandon, and K. Cunningham, "Free-to-roll analysis of abrupt wing stall on military aircraft at transonic speeds," in *41st Aerospace Sciences Meeting and Exhibit*, 2003, p. 750.

[51] F. J. Capone, R. M. Hall, D. B. Owens, J. E. Lamar, and S. N. McMillin, "Review and recommended experimental procedures for evaluation of abrupt wing stall characteristics," *Journal of aircraft*, vol. 41, no. 3, pp. 448–455, 2004.

[52] D. B. Owens, J. K. McConnell, J. M. Brandon, and R. M. Hall, "Transonic free-to-roll analysis of the f-35 (joint strike fighter) aircraft," *Journal of aircraft*, vol. 43, no. 3, pp. 608–615, 2006.

[53] P. L. Coe Jr, J. R. Chambers, and W. Letko, "Asymmetric lateral-directional characteristics of pointed bodies of revolution at high angles of attack," Tech. Rep., 1972.

[54] D. E. Hahne, J. M. Luckring, P. F. Covell, W. P. Phillips, G. M. Gatlin, J. D. Shaughnessy, and L. T. Nguyen, "Stability characteristics of a conical aerospace plane concept," *SAE Transactions*, pp. 1664–1682, 1989.

[55] C. Fremaux, D. Vairo, and R. Whipple, "Effect of geometry and mass distribution on tumbling characteristics of flying wings," *Journal of aircraft*, vol. 32, no. 2, pp. 404–410, 1995.

[56] CASA, *Advisory Circular Ac 61-16v1.0: Spin Avoidance and Stall Recovery Training*. CASA, Civil Aviation Safety Authority of the the Australian Government, April 2020.

[57] C. Cavagnaro, "Technique: Taming the stall slips, skids, and centering the ball," 2019. [Online]. Available: https://www.aopa.org/news-and-media/all-news/2019/april/pilot/technique-taming-the-stall

[58] *Airplane Flying Handbook (FAA-H-8083-3A)*. Federal Aviation Administration (FAA), US Department of Transportation Federal Aviation Administration, 2011.

[59] *Airplane Flying Handbook (FAA-H-8083-3B)*. Federal Aviation Administration (FAA), US Department of Transportation Federal Aviation Administration, 2016.

[60] *Stall and Spin Awareness Training, Advisory Circular No: 61-67C (FAA-H-8083-3A)*. Federal Aviation Administration (FAA), US Department of Transportation Federal Aviation Administration, 2016.

[61] Wikipedia, "Stall." [Online]. Available: https://en.wikipedia.org/wiki/Stall_(fluid_dynamics)

[62] K. Bangs, "No stall, no spin: why angle of attack is essential," 2020. [Online]. Available: https://airfactsjournal.com/2020/02/no-stall-no-spin-why-angle-of-attack-is-essential/

[63] S. B. Grafton, J. R. Chambers, and P. L. Coe Jr, "Wind-tunnel free-flight investigation of a model of a spin-resistant fighter configuration," Tech. Rep., 1974.

[64] M. P. Fink, D. C. Freeman Jr, and H. D. Greer, "Full-scale wind-tunnel investigation of the static longitudinal and lateral characteristics of a light single-engine airplane," Tech. Rep., 1970.

[65] J. P. Shivers, M. P. Fink, and G. M. Ware, *Full-Scale Wind-Tunnel Investigation of the Static Longitudinal and Lateral Characteristics of a Light Single-Engine Low-Wing Airplane*. National Aeronautics and Space Administration, 1970, vol. 5857.

[66] H. D. Greer, J. P. Shivers, M. P. Fink, and C. Carter, "Wind tunnel investigation of static longitudinal and lateral characteristics of a full scale mockup of a light single engine high wing airplane," Tech. Rep., 1973.

[67] M. P. Fink and D. C. Freeman Jr, "Full-scale wind-tunnel investigation of static longtudinal and lateral characteristics of a light twin-engine airplane," Tech. Rep., 1969.

[68] R. Smith, B. Dike, B. Ravichandran, A. El-Fallah, and K. Mehra, "Discovering novel fighter combat maneuvers: simulating test pilot creativity," in *Creative evolutionary systems*. Elsevier, 2002, pp. 467–VIII.

[69] J. D. Lang and M. S. Francis, "Unsteady aerodynamics and dynamic aircraft maneuverability," Air Force Avionics Lab Wright-Patterson AFB OH, Tech. Rep., 1985.

[70] W. B. Herbst, "Supermaneuverability," Messerschmitt-Boelkow-Blohm GMBH Munich (Germany FR), Tech. Rep., 1984.

[71] P. W. Harper and R. E. Flanigan, "The effect of rate of change of angle of attack on the maximum lift of a small model," Tech. Rep., 1950.

[72] F. D. Harris and R. R. Pruyn, "Blade stall—half fact, half fiction," *Journal of the American Helicopter Society*, vol. 13, no. 2, pp. 27–48, 1968.

[73] M. Fouda, N. M. Khalifa, M. M. Rashad, M. Shao, M. Elsharif, and H. E. Taha, "Static and dynamic characteristics of the aerodynamic forces on pitching airfoils between 0 to 360 degrees angle of attack," in *AIAA Scitech 2022 Forum*, 2022, p. 1663.

[74] W. J. McCroskey, L. W. Carr, and K. W. McAlister, "Dynamic stall experiments on oscillating airfoils," *AIAA Journal*, vol. 14, no. 1, pp. 57–63, 1976.

[75] U. B. Mehta, "Dynamic stall of an oscillating airfoil," *AGARD Unsteady Aerodyn.*, 1978.

[76] W. J. McCroskey and R. K. Fisher, "Detailed aerodynamic measurements on a model rotor in the blade stall regime," *Journal of the American Helicopter Society*, vol. 17, no. 1, pp. 20–30, 1972.

[77] N. D. Ham and M. S. Garelick, "Dynamic stall considerations in helicopter rotors," *Journal of the American Helicopter Society*, vol. 13, no. 2, pp. 49–55, 1968.

[78] G. J. Leishman, *Principles of helicopter aerodynamics*. Cambridge university press, 2006.

[79] W. Johnson, "The response and airloading of helicopter rotor blades due to dynamic stall," Massachusetts Institute of Technology, Cambridge Aeroelastic and Structures Research Laboratory, Tech. Rep., 1970.

[80] R. Lynette, *California wind farms: Operational data collection and analysis*. Solar Energy Research Institute, 1989.

[81] P. Veers, "The effect of aerodynamics analysis on fatigue life estimation," in *Wind Turbine Aerodynamics Seminar*, 1985, pp. 26–29.

[82] C. P. Butterfield, "Three-dimensional airfoil performance measurements on a rotating wing," Solar Energy Research Inst., Golden, CO (USA), Tech. Rep., 1989.

[83] H. A. Madsen, *Aerodynamics of a horizontal-axis wind turbine in natural conditions*, 1991.

[84] M. Robinson, M. Luttges, M. Miller, and D. Shipley, "Wind turbine blade aerodynamic: the analysis of field test data," *ASME SOL ENERGY DIV PUBL SED, ASME, NEW YORK, NY,(USA), 1994,*, vol. 15, pp. 9–16, 1994.

[85] O. D. Vries, "On the theory of the horizontal-axis wind turbine," *Annual review of fluid mechanics*, vol. 15, no. 1, pp. 77–96, 1983.

[86] W. Banks and G. Gadd, "Delaying effect of rotation on laminar separation," *AIAA journal*, vol. 1, no. 4, pp. 941–941, 1963.

[87] R. Leknys, M. Arjomandi, R. Kelso, and C. Birzer, "Dynamic-and post-stall characteristics of pitching airfoils at extreme conditions," *Proceedings of the Institution of Mechanical Engineers, Part G: Journal of Aerospace Engineering*, vol. 232, no. 6, pp. 1171–1185, 2018.

[88] S. I. Benton and M. R. Visbal, "Understanding abrupt leading edge separation as a mechanism for the onset of dynamic stall," in *2018 AIAA aerospace sciences meeting*, 2018, p. 0356.

[89] ——, "Effects of leading-edge geometry on the onset of dynamic stall," *AIAA Journal*, vol. 56, no. 10, pp. 4195–4198, 2018.

[90] G. Bangga, S. Hutani, and H. Heramarwan, "The effects of airfoil thickness on dynamic stall characteristics of high-solidity vertical axis wind turbines," *Advanced Theory and Simulations*, vol. 4, no. 6, p. 2000204, 2021.

[91] S. Guntur, N. N. Sørensen, S. Schreck, and L. Bergami, "Modeling dynamic stall on wind turbine blades under rotationally augmented flow fields," *Wind Energy*, vol. 19, no. 3, pp. 383–397, 2016.

[92] M. H. Hansen, M. Gaunaa, and H. A. Madsen, *A Beddoes-Leishman type dynamic stall model in state-space and indicial formulations*, 2004.

[93] N. Adema, M. Kloosterman, and G. Schepers, "Development of a second-order dynamic stall model," *Wind Energy Science*, vol. 5, no. 2, pp. 577–590, 2020.

[94] J. Holierhoek, J. De Vaal, A. Van Zuijlen, and H. Bijl, "Comparing different dynamic stall models," *Wind Energy*, vol. 16, no. 1, pp. 139–158, 2013.

[95] L. Pla Olea, N. M. Khalifa, and H. E. Taha, "Geometric control study of the beddoes-leishman model in a pitching-plunging airfoil," in *AIAA SCITECH 2022 Forum*, 2022, p. 2415.

[96] J. G. Leishman and T. Beddoes, "A semi-empirical model for dynamic stall," *Journal of the American Helicopter society*, vol. 34, no. 3, pp. 3–17, 1989.

[97] N. M. Khalifa, A. S. Rezaei, and H. E. Taha, "Comparing the performance of different turbulence models in predicting dynamic stall," in *AIAA Scitech 2021 Forum*, 2021, p. 1651.

[98] Wikipedia, "Extra ea-300lt specs." [Online]. Available: https://en.wikipedia.org/wiki/Extra_EA-300#Specifications_(EA-330LT)

[99] A. T. W. Aircraft, "Extra ea-300 and ea-330." [Online]. Available: https://janes.migavia.com/deu/extra/ea-300.html)

[100] *ZULTRAT Technical Data Sheet*, Zortrax. [Online]. Available: https://cf.zortrax.com/wp-content/uploads/2018/06/Z-ULTRAT_Technical_Data_Sheet_eng-1.pdf

[101] *ZULTRAT Safety Data Sheet*, Zortrax. [Online]. Available: https://cf.zortrax.com/wp-content/uploads/2018/06/Z-ULTRAT_Safety_Data_Sheet_eng-1.pdf

[102] J. M. McCarthy and G. S. Soh, *Geometric design of linkages*. Springer Science & Business Media, 2010, vol. 11.

[103] J. B. Barlow, W. H. Rae, and A. Pope, *Low-speed wind tunnel testing*. John wiley & sons, 1999.

[104] M. Fouda, M. A. Shorbagy, and H. E. Taha, "Multi-axis load cell provisional patent," March 2021, uS Provisional UC Case No. 2021-780-1.

[105] M. Zakaria, M. Fouda, and H. E. Taha, "Experimental investigation of aerodynamic characteristics of a 4-winged flapping," in *AIAA Scitech 2022 Forum*, 2022.

[106] D. Deb, K. Huang, M. Fouda, and H. E. Taha, "Effect of self-induced body vibrations on thrust generation in bio-inspired flying robots," in *AIAA Scitech 2022 Forum*, 2022.

[107] M. A. Shorbagy, B. El-hadidi, G. El-Bayoumi, O. Said, and M. Fouda, "Experimental study on bio-inspired wings with tubercles," in *AIAA SciTech 2019 Forum*, 2019, p. 0848.

[108] *Load cell power supply module adjustable from 4 to 15 VDC PSM-R data sheet*, Transducer Techniques. [Online]. Available: https://www.transducertechniques.com/pdf/psmr.pdf

[109] *USB Programmable Single Channel Instrumentation Amplifier and Low-Pass Filter data sheet*, Alligator Technologies. [Online]. Available: https://alligatortech.com/downloads/USBPGF-S1_Data_Sheet.pdf

[110] *NI USB-621x User Manual*, National Instruments. [Online]. Available: https://www.ni.com/pdf/manuals/371931f.pdf

[111] *Nema 23 Bipolar 0.9deg 1.26Nm Stepper Motor Data Sheet*, OMC-Stepperonline. [Online]. Available: https://www.omc-stepperonline.com/download/23HM22-2804S.pdf

[112] *AMT10 Modular Incremental Encoder Data Sheet*, CUI Devices. [Online]. Available: https://www.cuidevices.com/product/resource/amt10.pdf

[113] *ÄeroLab Subsonic Wind Tunnel 30ẍ30¨*, AEROLAB. [Online]. Available: https://www.aerolab.com/aerolab-products/open-circuit-wind-tunnels/

[114] R. E. Sheldahl and P. C. Klimas, "Aerodynamic characteristics of seven symmetrical airfoil sections through 180-degree angle of attack for use in aerodynamic analysis of vertical axis wind turbines," Sandia National Labs., Albuquerque, NM (USA), Tech. Rep., 1981.

[115] D. J. Dulin and T. T. Takahashi, "Design implications of elliptical planform wings," in *56th AIAA/ASCE/AHS/ASC Structures, Structural Dynamics, and Materials Conference*, 2015, p. 0397.

[116] semelton1, "Rv-7a stall test with wing tufts," 2014. [Online]. Available: https://www.youtube.com/watch?v=ECTCVgiBHjA

Appendix A

Airplane models

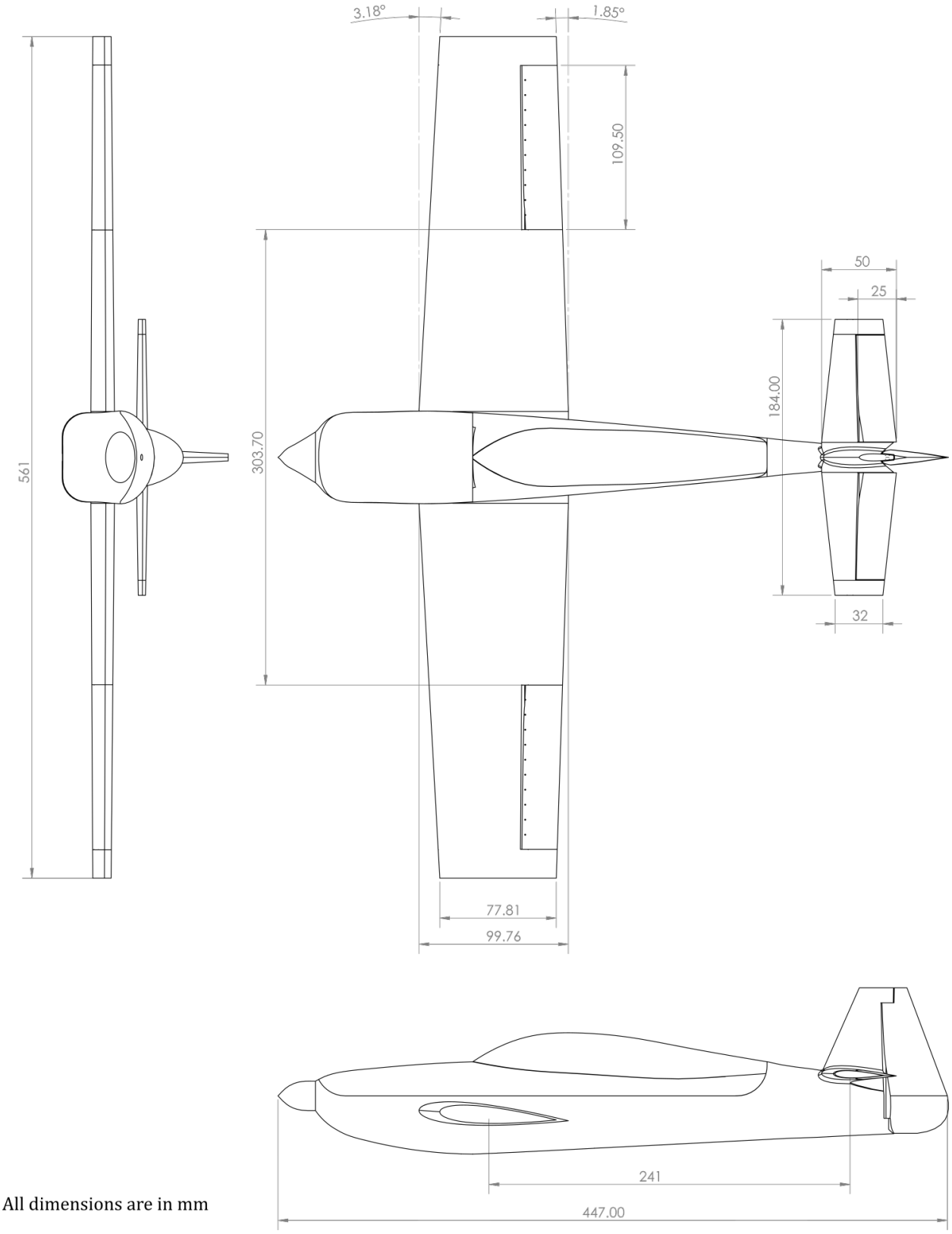

Figure A.1: Three-view drawing of the taper wing planform airplane model

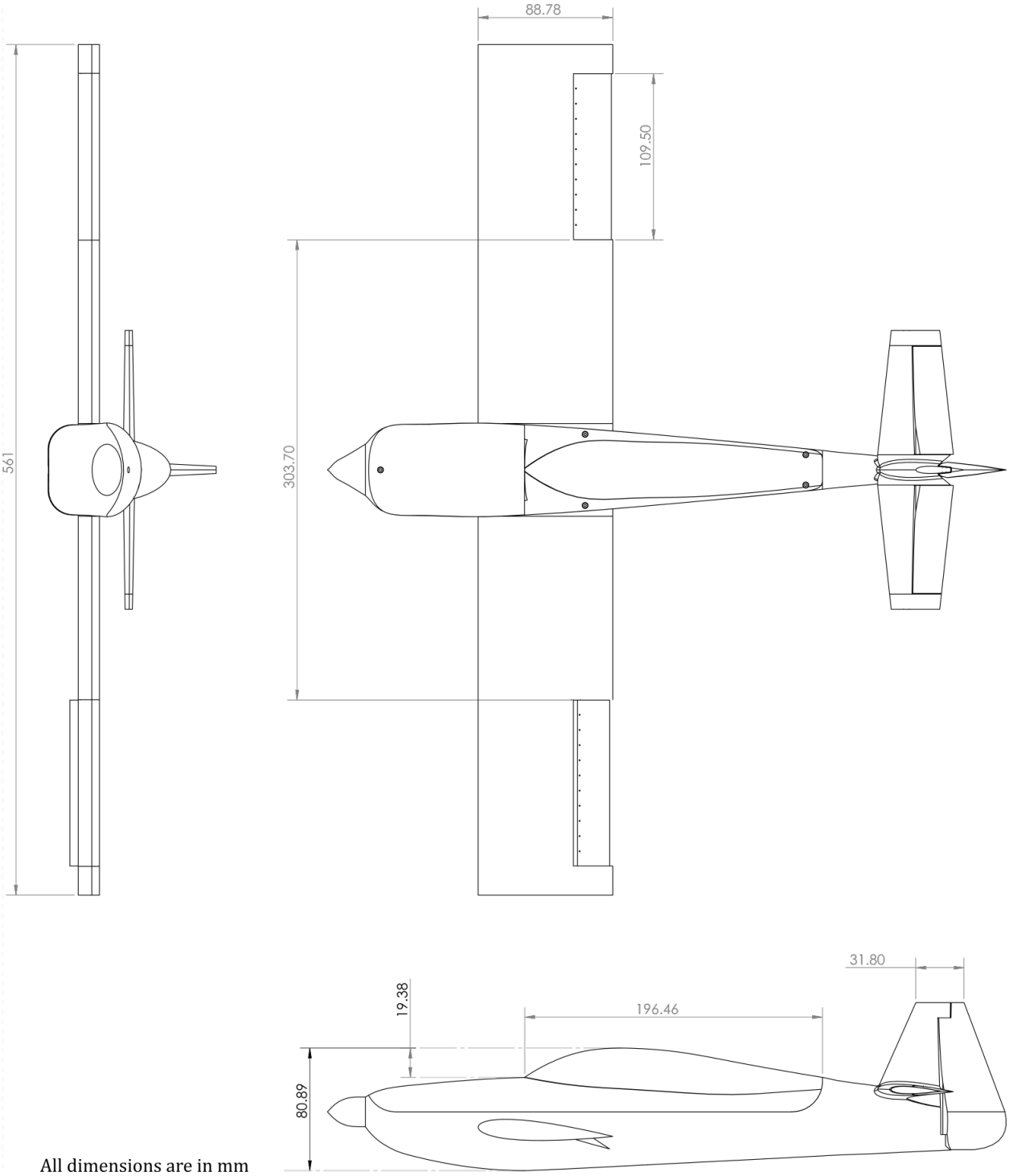

Figure A.2: Three-view drawing of the straight/rectangular wing planform airplane model

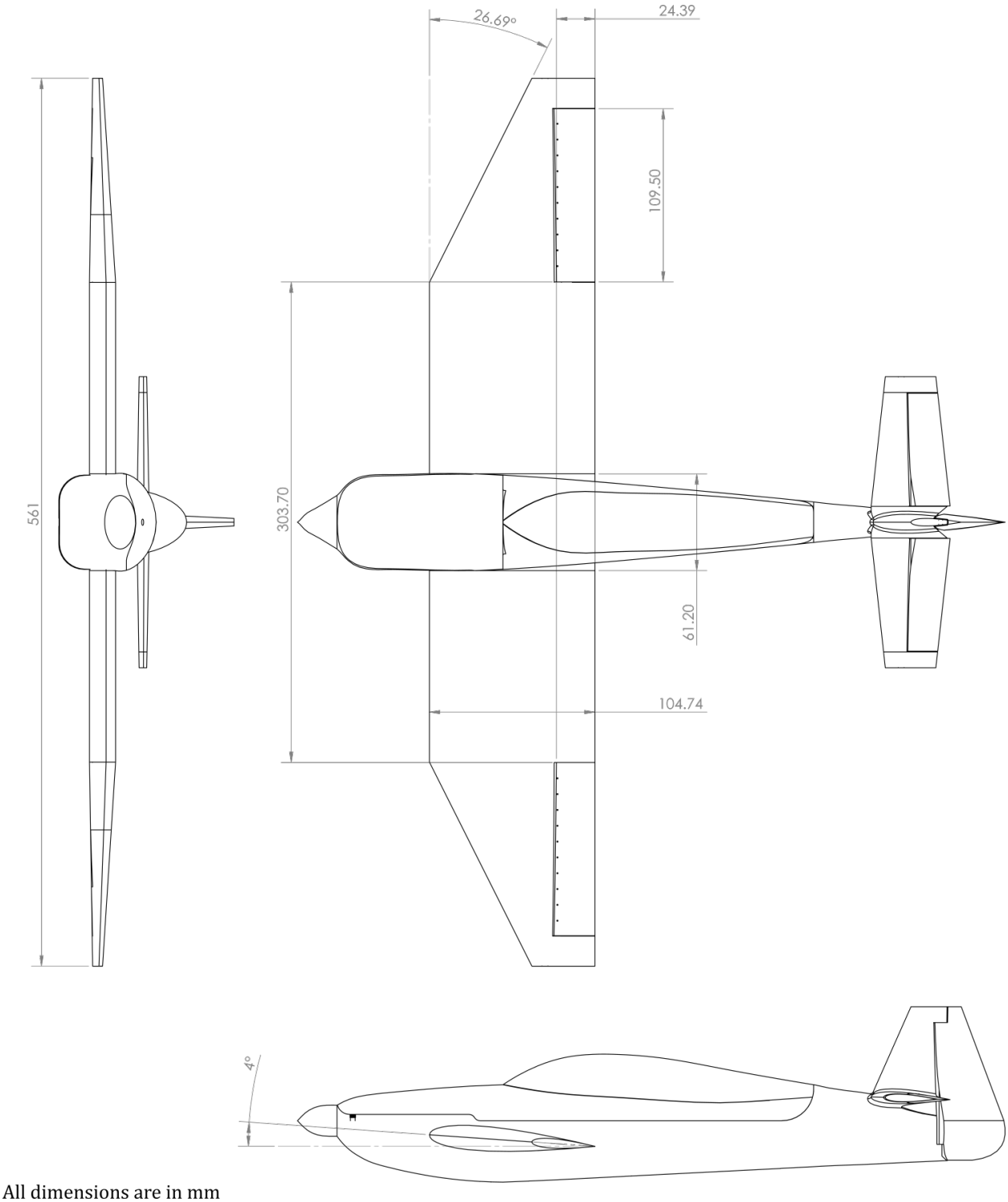

Figure A.3: Three-view drawing of hybrid wing planform airplane model

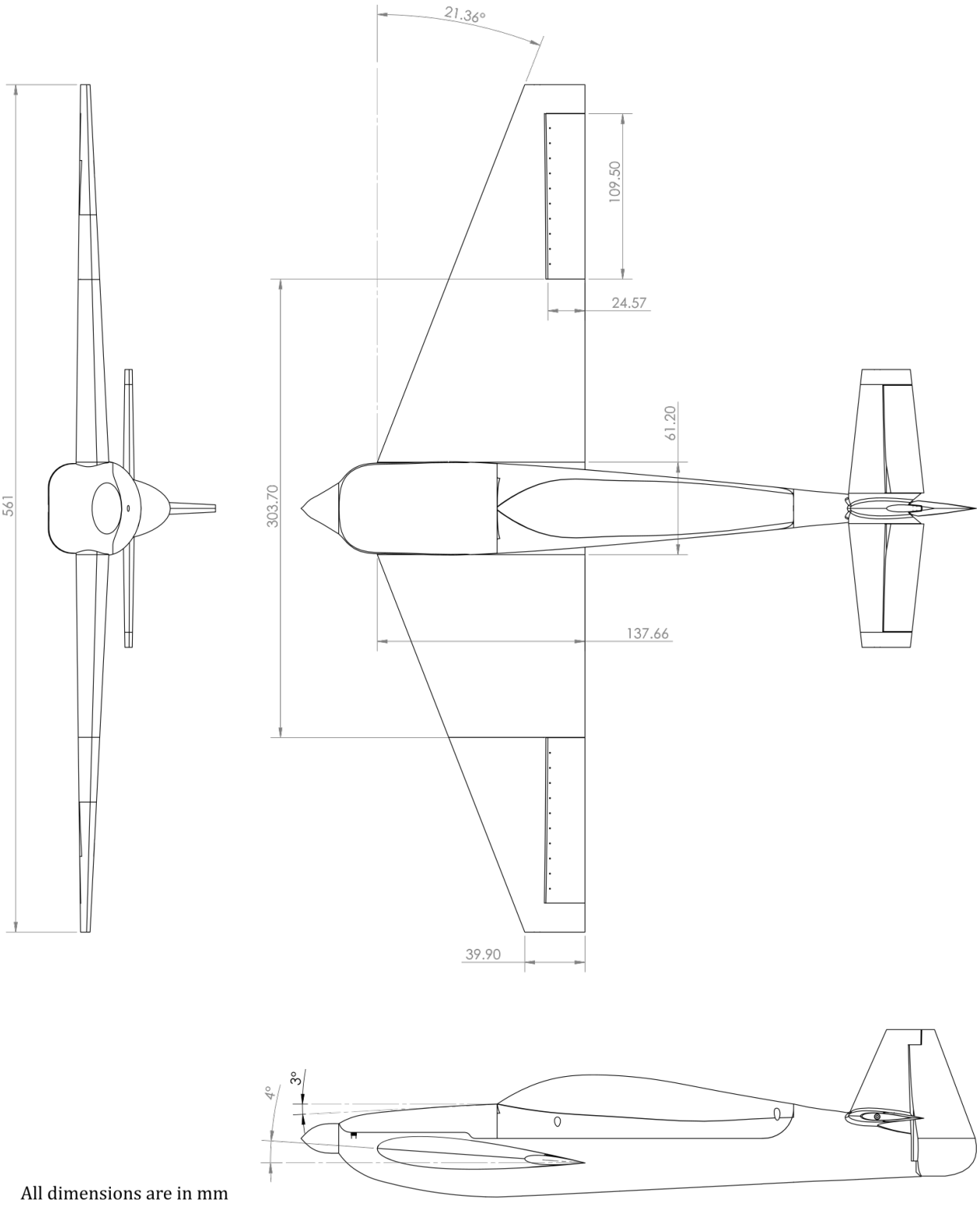

Figure A.4: Three-view drawing of delta wing planform airplane model

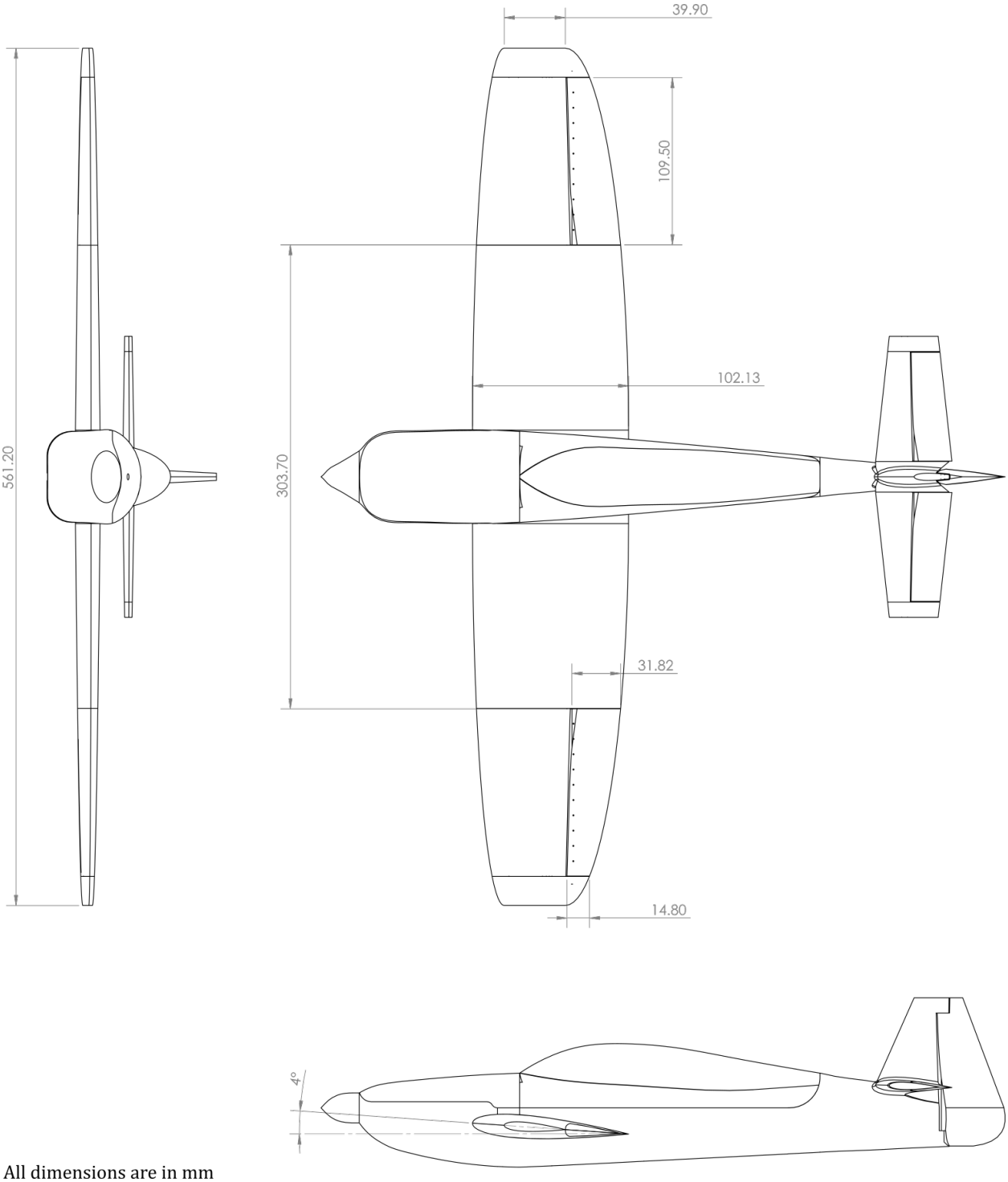

Figure A.5: Three-view drawing of elliptic wing planform airplane model

Appendix B

Load Balance LabVIEW data flow program

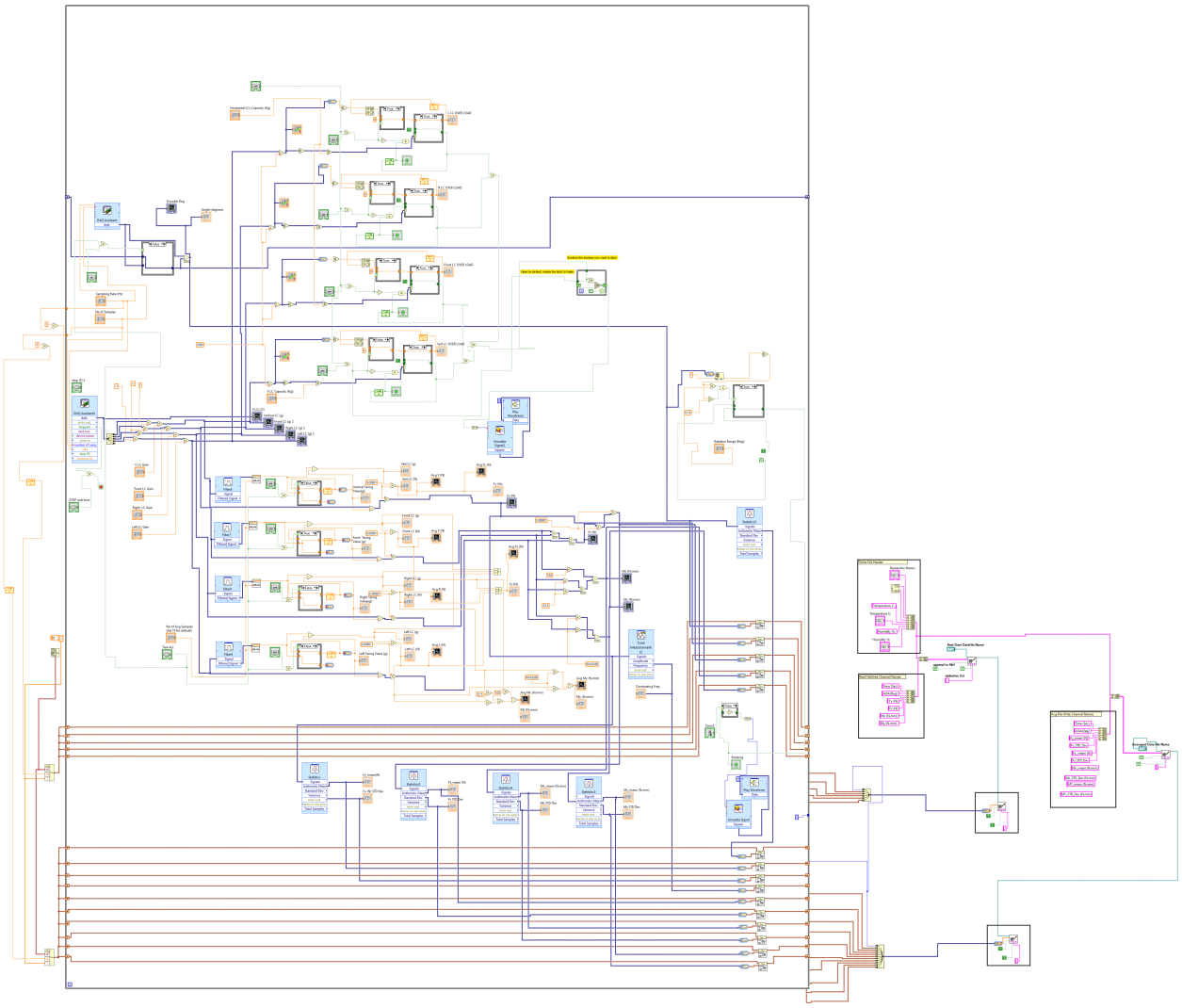

Figure B.1: Load balance interface program - LabVIEW block diagram

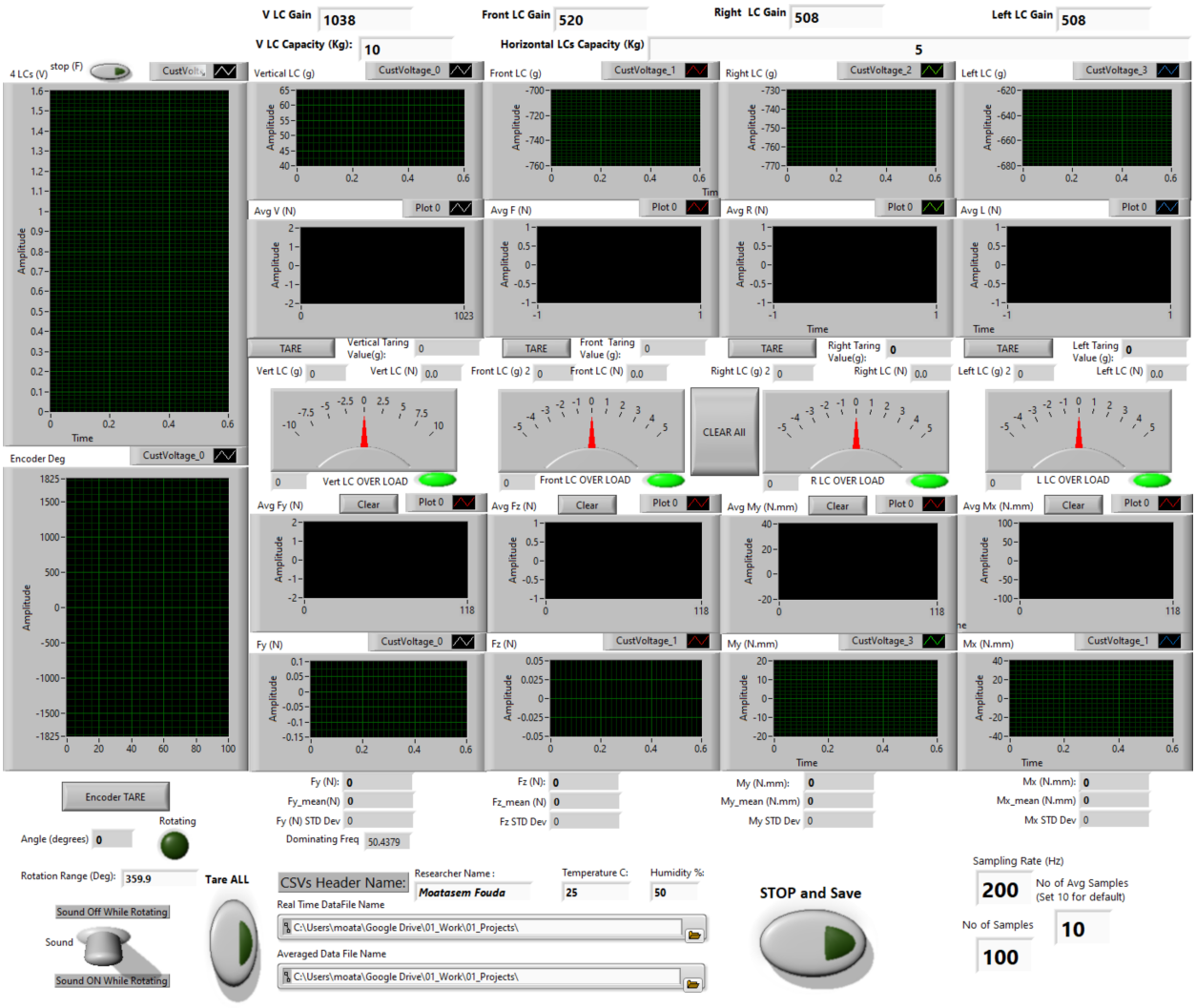

Figure B.2: Load balance interface program – LabVIEW front panel

Appendix C

Airplane model control surfaces program - Arduino code

```
#include <Servo.h>

String angle; //angle of deflection desired
char surface; //decide which surface to be deflected
Servo aileron, elevator, rudder;
double transfer; //transfer function of 4 bar mechanism TBD
double elevatoroffset;
double aileronoffset;
boolean sign=false;

void setup() {
  Serial.begin(9600);  //clock

  aileron.attach(11);  //the pin for the aileron control
  elevator.attach(10);  //the pin for the elevator control
  rudder.attach(8);  //the pin for the rudder control

  aileron.write(0);
  elevator.write(0);
  rudder.write(0);
}
void loop(){


  if (Serial.available()) //checks if there is an input
  {
    char c = Serial.read();  //gets one byte from serial buffer
    if (c == '-'){
      sign=true;
    }
    else if (isDigit(c) || c== '.')
    {
      angle+=c;
    }

    else if(c==',')
    {
      double deflection = angle.toDouble();
```

```
    double deflection = angle.toDouble();
    if(sign){
      deflection*=-1;
      sign=false;
    }
    transfer=10.5/6*sin(radians(deflection));
    double n= (asin(transfer)*57296) / 1000;
    n+=90;
      if(surface=='a'){
      aileron.write(n+aileronoffset);
      Serial.print("Ailerons deflected to ");
      Serial.print(deflection);
      Serial.print(" degrees.");
      Serial.println();
      delay(250);
     /*aileron.detach();*/
    }
    if(surface=='e') {
      elevator.write(n+elevatoroffset);
      Serial.print("ELevator deflected to ");
      Serial.print(deflection);
      Serial.print(" degrees.");
      Serial.println();
      delay(100);
     /*elevator.detach();*/
    }
    if(surface=='r') rudder.write(n);

    angle="";
  }
  else
  {
   surface=c;
  }
}
```

Appendix D

Pitching wings - Dynamic stall experiment- Arduino code

```
#include "variables.h"
void setup() {
  Serial.begin(9600);
  pinMode (driverPUL, OUTPUT);
  pinMode (driverDIR, OUTPUT);
  digitalWrite(ENA, HIGH); //energize and hold the stepper motor

}
void loop() {
  Serial.print("Current Position: ");
  Serial.print(currentPos);
  Serial.print(" Degrees");
  Serial.println();

  Serial.println("Enter the desired angle for the motor
  while (Serial.available() < 2) {}  in degrees{-360,360}");
  targetPos = Serial.parseFloat();
  Serial.print("Target Position: ");
  Serial.print(targetPos);
  Serial.print(" Degrees");
  Serial.println();
  Serial.println();
  Serial.println();


  Serial.println("Enter the desired number of rotations");
  while (Serial.available() < 2) {}
  noOfRev = Serial.parseFloat();
  Serial.print("Number of Rotations: ");
  Serial.print(noOfRev);
  Serial.println();
  Serial.println();
  Serial.println();
```

```
Serial.println("Enter the desired speed in deg/s (1~400 deg/s)");
while (Serial.available() < 2) {}
angVel = Serial.parseFloat();
Serial.print("Angular Speed: ");
Serial.print(angVel);
Serial.print(" Deg/Sec");
Serial.println();
Serial.println();
Serial.println();

if (revsDelay < 180 / angVel) {
  revsDelay = 180 / angVel;
}


pulsDelaySeconds = (1 / (angVel * plusesPerRev)) ;

pulsDelay = 180000000.0 * pulsDelaySeconds ;

if (targetPos > currentPos) {
  setdir = HIGH;
  angDisp = targetPos - currentPos;
}
else if (targetPos < currentPos) {
  setdir = LOW;
  angDisp = currentPos - targetPos;
}
else {
  Serial.println("Motor is already at this position");
  steps = 0;
}
```

```
  else if (targetPos < currentPos) {
    setdir = LOW;
    angDisp = currentPos - targetPos;
  }
  else {
    Serial.println("Motor is already at this position");
    steps = 0;
  }

  steps = int (round(angDisp * plusesPerRev / 360));
  digitalWrite(driverDIR, setdir);

  for (int j = 0; j < noOfRev; j++) {
    for (int i = 0; i < steps; i++) {
      digitalWrite(driverPUL, HIGH);
      delayMicroseconds(pulsDelay);
      digitalWrite(driverPUL, LOW);
      delayMicroseconds(pulsDelay);
    }
    curnoOfRev = j + 1;
    Serial.print(" No of Completed Revolutions:   ");
    Serial.print(curnoOfRev);
    Serial.println();
    delay(revsDelay * 1000);

  }

  currentPos = curnoOfRev * targetPos;

  delay(500);


}
```

Appendix E

Static test of the rotating wings - Arduino code

```
#include "variables.h"

void setup() {
  Serial.begin(9600);
  pinMode (driverPUL, OUTPUT);
  pinMode (driverDIR, OUTPUT);
  digitalWrite(ENA, HIGH); //energize and hold the
                                          stepper motor
}
void loop() {
  Serial.print("Current Position: ");
  Serial.print(currentPos);
  Serial.print(" Degrees");
  Serial.println();

  Serial.println("Enter the desired angle for the motor
  while (Serial.available() < 2) {}  in degrees{-360,360}");
  targetPos = Serial.parseFloat();
  Serial.print("Target Position: ");
  Serial.print(targetPos);
  Serial.print(" Degrees");
  Serial.println();


  Serial.println("Enter the desired speed in deg/s
  while (Serial.available() < 2) {}      (1~400 deg/s)");
  angVel = Serial.parseFloat();
  Serial.print("Angular Speed: ");
  Serial.print(targetPos);
  Serial.print(" Deg/Sec");
  Serial.println();
```

```
Serial.println("Enter the static test angular step (should be multiple of 0.9 deg");
while (Serial.available() < 2) {}
staticMove = Serial.parseFloat();
Serial.print("Static Test Step: ");
Serial.print(staticMove);
Serial.print(" Deg");
Serial.println();


Serial.println("Enter the static test hold between the steps in seconds");
while (Serial.available() < 2) {}
stopsHold = Serial.parseFloat();
Serial.print("Static Test Hold between Step: ");
Serial.print(stopsHold);
Serial.print(" Seconds");
Serial.println();

pulsDelaySeconds = (1 / (angVel * plusesPerRev)) ; //(360/angVel)
                                                   =period of one revolution,
pulsDelay = 180000000.0 * pulsDelaySeconds ;          pulsDelay in microseconds


if (targetPos > currentPos) {
  setdir = HIGH;
  angDisp = targetPos - currentPos;
}
else if (targetPos < currentPos) {
  setdir = LOW;
  angDisp = currentPos - targetPos;
}
else {
  Serial.println("Motor is already at this position");
  steps = 0;
}
```

```
}
else {
  Serial.println("Motor is already at this position");
  steps = 0;
}


steps = int (round(staticMove * plusesPerRev / 360));
digitalWrite(driverDIR, setdir);


noStops = angDisp / staticMove;

for (int j = 0; j < noStops; j++) {

  for (int i = 0; i < steps; i++) {
    digitalWrite(driverPUL, HIGH);
    delayMicroseconds(pulsDelay);
    digitalWrite(driverPUL, LOW);
    delayMicroseconds(pulsDelay);
  }

  currentPos = currentPos + staticMove;
  Serial.print(" Current Position is: ");
  Serial.print(currentPos);
  Serial.print(" Deg");
  Serial.println();
  delay (stopsHold * 1000);
}
currentPos = targetPos;

delay(500);
```